DISSERTATION

A CLONABLE SELENIUM NANOPARTICLE IN ACTION: HIGH RESOLUTION LOCALIZATION OF FTSZ USING ELECTRON TOMOGRAPHY

Submitted by

Kanda Borgognoni

Department of Chemistry

In partial fulfillment of the requirements

For the Degree of Doctor of Philosophy

Colorado State University

Fort Collins, Colorado

Spring 2021

Doctoral Committee:

Advisor: Christopher J. Ackerson

James Neilson
Alan J. Kennan
Susan Tsunoda

ABSTRACT

A CLONABLE SELENIUM NANOPARTICLE IN ACTION: HIGH RESOLUTION LOCALIZATION OF FTSZ USING ELECTRON TOMOGRAPHY

A meaningful understanding of biochemistry requires that we understand the function of proteins, which is heavily dependent on their structure and location within an organism. As the Resolution Revolution of cryo-electron microscopy gains unprecedented ground largely due to the recent development of commercially available direct electron detectors, energy filters, and high-end computation, thousands of protein structures have been solved at atomic or near-atomic resolution, with the highest resolution structure to date being solved at 1.2 Å. A major challenge that has limited the broad use of cryo-electron tomography (cryo-ET) is locating a protein of interest in an organism, as no commercially available high-contrast markers which can be generated *in vivo* exist. Herein, we present a breakthrough study which aims to solve this problem by synthesizing high contrast metal nanoparticles labeling desired proteins *in situ*. We isolated a Glutathione Reductase-like Metalloid Reductase (GRLMR), which can reduce selenite and selenate into selenium nanoparticles (SeNPs), from *Pseudomonas moraviensis* stanleyae found in the roots of a Se hyperaccumulator *Stanleya pinnata*, or Desert Princes' Plume. A recombinant variant, denoted as a clonable Selenium NanoParticle (cSeNP), was fused to filamentous temperature sensitive protein Z (FtsZ), and the chimera was expressed *in vivo* using a T7 expression system in model organism *E. coli* for a proof-of-concept study. Because the SeNPs biogenically produced are amorphous, they exist in a quasistable state and are composed of polymeric Se_n in the form of chains and rings that are constantly breaking and reforming through one and two electron propagation. To stabilize the particles during cellular preservation *ex aqua*,

a disproportionation-like reaction can be done either *in vivo* or as a post-fixation step to form crystalline metal selenide (MSe) NPs that can withstand the processing liquids used. Thereafter, electron tomography was used to acquire a tilt series that was reconstructed into a tomogram and segmented using IMOD, generating a model representing MSeNPs labeling FtsZ filaments. As such, we have demonstrated the potential of using cSeNP as a high resolution marker for cryo-ET. While our study relied on traditional preservation and embedment techniques, we anticipate that for cells preserved via vitrification, cloned SeNPs can be used without subsequent transformation to MSeNPs, as the amorphous particles are stable in aqueous media. Prospectively, we expect that clonable nanoparticle technology will revolutionize cryo-ET, allowing us to localize proteins *in vivo* at high resolution while maintaining organism viability through metal immobilization. Furthermore, this technique can be expanded to other imaging modalities, such as light microscopy and X-ray tomography, through the discovery and engineering of other clonable nanoparticles.

ACKNOWLEDGEMENTS

In acknowledgement of the work itself, it could not have been done without the efforts of several people who have contributed to the advancement of clonable nanoparticle technology. To Bossman Ack for starting the lab and the bud of the idea. It has truly flourished into something quite revolutionary (in our opinion, obviously, and hopefully in others' too). Thank you for working with me over the years and for providing the support that you could. It was certainly more than what most advisors would have done.

To those who began the journey, Ricky (who I had the chance to work with and learn from), Thomas, Mackenzie, and Lucian, by discovering GRLMR from a field in Colorado and doing all of the initial studies. In that regard, I guess we should also thank those miners from the 1800s who did not mind dumping their waste into nature…? Lemon meringue pie from lemons. To Zach (Butz) who I worked closely with for several years on this project. It would not have gotten to this stage without you. To Zach (Nilsson), who also has contributed to the advancement of this project through instrumentation expertise. To those in the Prieto group, Jen and Becca, for multiple discussions about synthesizing and looking at nanoparticles.

To my lab mates Phillip my desk buddy, James and Ian for keeping me up to date on the extreme right ideals, Christian and Hosier and Ryan for being responsible adults I could talk with about problems and science, and Alex and Collin for keeping me company in the Bio lab. To the Ack lab alumni. Heine for being awesome, Tim for showing me around and talking with me about the lab, Thomas for continuing to talk with me about TEM and other stuff, and Scott and Marcus for hanging out with us.

To my family for supporting me. My no FOMO Mom for making me smart and Alex for being the best big brother in the world. To those who personally supported me, especially Lily, Neubs, and Maggie for always being true friends. To my wifey Luiza, I am very grateful to have met you. I am also thankful to have met the other Brazilians, Rute, Daniel, Chawani, Juliana, and Priscilla, for the great times we had together in the USA and in Brazil. To my pottery friends, Liz and David and Sean and Matt and Sue, for having a blast with ceramics.

TABLE OF CONTENTS

CHAPTER 1: Introduction to Clonable Nanoparticle Technology

Proteins are largely responsible for all of the processes that maintain the health and proper function of each individual cell. Incredibly, these proteins must work together in a delicate balance to perform variegated tasks such as biomolecule transport, signaling, catalysis, and gene regulation as a few examples. A full understanding of how specific cell types contribute to the vitality of an organism requires that we understand complex biological systems, which are composed of and regulated by **proteins**. Thus, methods that probe protein function is paramount to the fundamental understanding of how organisms function at the molecular level.

The main determinants of protein function are structure and location within a system. Great advances have been made in structure determination due to the considerable developments in X-Ray Crystallography and NMR Spectroscopy, allowing for tens of thousands of proteins to be solved at angstrom-level resolution and deposited into the Protein Data Bank (PDB).[1] While these achievements are instrumental to progress in the field, these methods are limited to proteins that are amenable to specific experimental parameters. For example, proteins must be fairly small to be analyzed by traditional H^1NMR (~35 kDa), or they must be crystallizable to be analyzed using X-Ray Spectroscopy.[1,2] Importantly, these methods rely on extracting and purifying a protein of interest. This removes it from the native environment, causing a loss of one of the key determinants of protein function: **location**. Hence, for a full understanding of biological systems, it is vital to also localize where proteins of interest are within a cell using microscopy.

Biological microscopic studies, once revolutionized by the discovery of clonable fluorophores like Green Fluorescent Protein (GFP), engender foundational evidence for cellular processes via *in situ* protein labeling and tracking by fluorescence. While fluorescence microscopy has greatly improved our understanding of subcellular processes, it is limited by low spatial

resolution due to the diffraction limit of light.[3,4] Typically, standard fluorescence microscopy is limited to around 200 nm spatial resolution in two dimensional imaging and 400 nm in tomography, which is larger than many subcellular structures as shown in Figure 1.1 reproduced with permission from Huang *et al*.[4–7] Currently, super resolution methods that break the diffraction barrier of light are vigorously being developed. While super resolution fluorescence microscopy has the potential of achieving a spatial resolution up to 10 nm, the best resolution achievable with a *biogenic* tag remains around 40 nm in two dimensions.[4,7–10] Furthermore, light microscopy is limited to locating only the proteins that are labeled, which disregards important structural information of the surroundings.

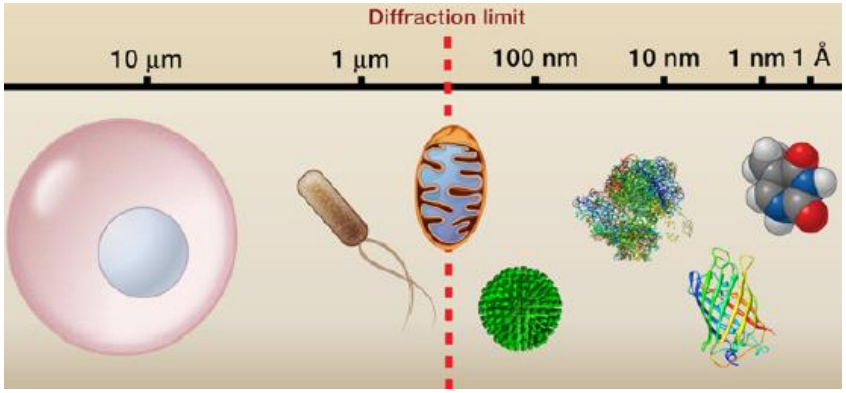

Figure 1.1: Sizes of common biological specimens and structures and the resolution limit of light microscopy reproduced with permission from Huang *et al.* (2010). From left to right: mammalian cell, bacterial cell, mitochondrion, influenza virus, ribosome, green fluorescent protein, thymine.

For a global picture that details cellular ultrastructure, we must turn to electron microscopy (EM), which is experiencing its own Resolution Revolution due to recent developments commercially available direct electron detectors and user friendly, computationally expensive programs.[11–14] Cryo-electron tomography (cryo-ET) of whole organisms coupled with subtomogram averaging permits us to resolve proteins to ca. 2.6 nm on average, with the highest resolved structure to date being solved to near-atomic precision at 3.5 Å.[15] Of particular importance to this revolution is single-particle cryo-EM, which has resulted in over 6,000

structures being solved at near-atomic or atomic level resolution and deposited into the Electron Microscopy Data Bank (https://www.ebi.ac.uk/pdbe/emdb/index.html). The highest resolved structure of human apoferritin has been solved to 1.15 Å resolution.[12,16] Not only does this rival X-ray crystallography, but it also provides a means to solve structures of proteins that cannot be crystallized, as is the requirement for X-ray analysis.[17] Furthermore, to study small proteins that can be crystallized, by using microcrystal electron diffraction (microED) coupled with tomography, it is possible to solve crystal structures in three dimensions to subatomic resolution, with the highest resolution achieved to date being 0.6 Å.[18] In short, electron microscopy allows us to view high resolution, global pictures of organisms as well as routine near-atomic resolution images of cellular ultrastructure.

Fundamentally, images are created in an electron microscope through the sample/beam interaction. This interaction causes countless events to occur, such as electron scattering, secondary electron scattering, and X-ray emissions to name a few, which allows us to collect many different forms of data. For example, by measuring the electrons ejected from the sample, we can gain topographical information from the sample as is routine for Scanning Electron Microscopy (SEM). The X-rays emitted from the sample can be used for elemental analysis with techniques like Energy Dispersive X-ray Spectroscopy (EDS). Finally, measurably scattered electrons allow us to view atomic-level structures, such as lattice planes in crystalline samples, and create high-resolution images in Transmission Electron Microscopy (TEM).[19–24] To create such high-resolution images in biological TEM, it is vital to create contrast. Since low atomic number elements (i.e. the main components of biomatter: C, N, O) interact very little with the incident beam, exogenous elements with a drastically different atomic composition must be added, such as a heavy metal, to "stain" biological material.[20,25–27] While common heavy metal staining provides

the necessary contrast, these stains only target common structures and functional groups (phospholipids, DNA, amines, etc.), making it impossible to visualize specific proteins.[26,28]

To improve contrast specificity, immunogold labeling was developed for by conjugating antibodies to gold nanoparticles.[29–33] Even though antibodies can hypothetically localize specific proteins, in practice these proteins tend to lose their antigenicity during sample processing that leads to background labeling.[34] In another aspect, the nanoparticle conjugates are too large to diffuse through the cell membrane (ca. 15 – 20 nm), requiring that the technique be used as a post-fixation step after the cell or tissue has been sliced open to expose the target.[25,30–33,35,36] This limits our use of high contrast markers to room temperature EM analysis. With the extraordinary advances currently underway in cryo-EM, largely thanks to the development of direct electron detectors and high-end computing, it is a great disadvantage to be unable to use this technique efficiently in a living system.[14]

Alternatively, the label can be introduced into the organism at the DNA level by cloning the genetic sequence of the tag directly conjugated to the protein of interest, providing perfect specificity. Practically, clonable markers must be portable, small enough to not alter protein function, and must not require post-synthetic modification to be functional.[37–40] The *grand challenge* to developing a clonable EM tag is that the label itself cannot be the contrast agent. The clonable tag must be able to *produce* the contrast agent. To date, the most promising biogenic tags, like APEX2, use radicals to generate a localized osmiophilic polymer that can be stained with osmium tetroxide.[3,28,33,41,42] While there are some considerations to mind regarding the specificity of the metal stain, the main limitation with this method is that it cannot be done *in vivo*. The sample must be fixed in order to generate the contrast agent, which again neglects the opportunity for native cryo-EM imaging. Also, conventional fixation leads to artifacts and great perturbation of

cellular ultrastructure, which can cause misinterpretation of structural data. To date, our inability to use the few clonable EM tags that have been developed is greatly limiting.[25]

We believe a better approach would be to use enzymes capable of forming a metal nanoparticle so that a high contrast marker would be localized directly next to a target of interest (see Figure 1.2). Countless methods of biological nanoparticle synthesis have been developed that utilize either bioscaffolds for patterned mineralization or organismal extracts for metal reduction and nanoparticle production.[43–56] However, no reports exist of single enzymes capable of reducing or oxidizing metals into nanoparticle form.[57]

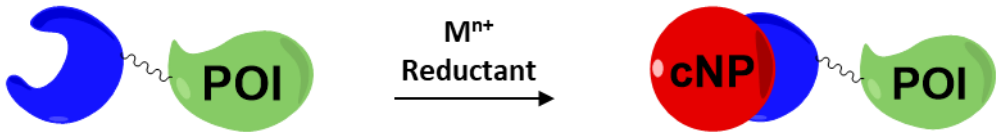

Figure 1.2: Cartoon representation of a clonable nanoparticle tag synthesized by an enzyme linked to a protein of interest (POI).

Heavy metals pose a threat to living organisms, as they have been shown to exhibit great toxicity via mechanisms that either produce radical oxygen species or interfere with essential nutrient uptake.[57–63] To alleviate these detriments, biological pathways have naturally evolved to handle heavy metal stress through small molecule chelation, protein adsorption, metal efflux, and immobilization.[57–73] Of particular interest to us are pathways that have evolved to immobilize metals in the form of nanoparticles. Nanoparticles are easily distinguished from biological material in an electron microscope and can be cleared through the renal system of organisms at sizes less than 6 nm, greatly reducing their long-term toxicity.[74,75] Therefore, by developing a clonable nanoparticle, i.e. by genetically encoding an enzyme capable of synthesizing a nanoparticle, it is possible to achieve EM contrast *in situ* while maintaining organism viability and target function.

We initiated a field study in the Colorado Mineral Belt collecting bacterial samples found in heavy metal contaminated waters.[76] We hypothesized that these bacteria are likely surviving due to one of the detoxification pathways mentioned above. To this end, we can isolate and screen

various species against toxic levels of different metals found at the site and search for nanoparticle formation via an observed color change in the bacterial culture.

One strain, *Pseudomonas moraviensis* stanleyae, was isolated from the root of a Se hyperaccumulator *Stanleya pinnata*, or Desert Princes' Plume. The strain was extremely tolerant to toxic levels of SeO_3^{2-} and SeO_4^{2-} (10 mM) and turned a brick red color, indicating the formation of zerovalent, amorphous Se as shown in Figure 1.3.[57,76] The left image is a suspension culture of the strain when exposed to 10 mM SeO_3^{2-} and the right picture is of the control where no SeO_3^{2-} was added. In a separate study, it was also shown that *P. moraviensis* is the fastest Se-reducing strain in the world.[77]

Figure 1.3: Bacteria grown with (left) and without (right) SeO_3^{2-} supplementation in LB. Cultures under notmal growth conditions appear yellow like the flask on the right. Because GRLMR reduces SeO_3^{2-} to SeNPs, the culture changes collor from yellow to red as seen in the right flask. Image reproduced from Ni, T. *et al*. (2015) with permission from RSC Publishing.

From this strain we isolated a single enzyme, a Glutathione Reductase-like Metalloid Reductase (GRLMR), that was responsible for reducing selenoxyanions into amorphous Se nanoparticles (SeNP) in a NADPH-dependent manner.[57] As a homodimer capable of forming nanoparticles, we hypothesized that GRLMR would be a great springboard in a proof-of-concept

study showing the possibility of using clonable nanoparticle labeling technology for high resolution localization in biological electron microscopy.

CHAPTER 2: Characterizing the Size Control and Conjugation of a Clonable Selenium Nanoparticle[a]

Introduction

For this tag to be effective, three criteria must be met by the enzyme: reduction of the metal precursor, nanoparticle retention, and size control.[57] While GRLMR innately meets the first criteria, it was not capable of conjugating to those particles once formed or effectively controlling the size of SeNPs. Retention of the nanoparticle is crucial so as to avoid nonspecific contrast in electron microscopy. Additionally, it has been suggested that a particle size of ~5 nm should be small enough to not disrupt native target function, necessitating enzymatic size control.[57]

For nanoparticle conjugation, we needed to modify the enzyme to contain a region that favored SeNP binding. We used a phage display assay, which has been done successfully by other groups to specifically bind metal salts, nanoparticles, and surfaces, to create a library of 12-residue peptides that specifically favored SeNP binding.[57,78] These peptides were screened against 5 nm enzymatically produced particles, and from this library we found that the 12mer with the sequence LTPHKHHKHLHA worked as the best selenium binding peptide (SeBP).[78] Because GRLMR functions as a homodimer, we first concatenated two copies of the wild type (WT) gene together using a flexible-rigid-flexible linker with the sequence (GGGGS)-(EAAAK)-(GGGGS) along with two copies of SeBP.[57,78] The final construct is denoted as a clonable Selenium NanoParticle (cSeNP).

To characterize peptide-SeNP conjugation, we can use vibrational spectroscopy to probe specific side chains that we suspect are interacting with the nanoparticle by tracking known

[a] Zachary Butz and Kanda Borgognoni contributed equally to the manuscript from which this chapter is based. Shown in detail here is the work contributed by Kanda Borgognoni.

markers for metal binding and backbone conformation. To avoid saturation from water modes, Raman spectroscopy was chosen for the vibrational study. For a molecule to be Raman active, the change in the polarizability of the bond must be nonzero. Raman scattering occurs when the photons of a monochromatic light source collide with the electrons of the molecule and become inelastically scattered. The intensity of the mode is dependent on the change in polarizability of the molecule, and the shift is due to the vibrational energy of the mode with respect to the wavelength of incident light. For example, highly polar molecules such as water will have a very weak signal in Raman spectroscopy due to the lack of polarizability of the OH bond. Because of the weak water signal, Raman spectroscopy is ideal for studying biomolecules.

Results and Discussion

Enzyme-NP conjugation of WT versus the variant (cSeNP) was initially tested using a Bradford assay to measure the amount of enzyme that remained associated with SeNPs. The results in Appendix A Figure A.1 demonstrate that only 13% of WT was bound to SeNPs whereas 82% of cSeNP bound to particles. This suggests that fusion of SeBP to GRLMR greatly improved the conjugation of the enzyme to nanoparticles.

To confirm that SeBP was forming a covalent bond with the SeNP surface, Raman spectroscopic analysis was conducted. Because histidine (labeled for clarity in Figure 2.1) has been shown to play an important role in coordinating metal ions such as Cu^{2+} and Zn^{2+}, we believe that

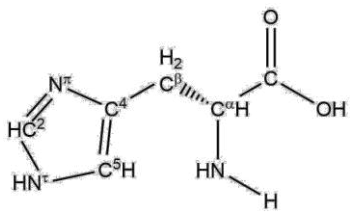

Figure 2.1: Histidine labeled for clarity when discussing vibrational modes below. Structure generated using ChemDraw®.

the SeBP binds favorably to SeNPs due to the abundance of His present.[79–83] The nitrogen atoms of the imidazole ring at the first and third position are labeled N^{τ} and N^{π}, respectively.[15] The imidazole group is known to coordinate with metal ions, and tautomer markers in the 900 – 1630 cm^{-1} region have been previously used to identify His-metal binding.[80–82,84] Depending on the protonation state of the ring, the 1565 – 1635 cm^{-1} region correlates with the $C^4{=}C^5$ stretching mode. This mode tends to upshift by 10 – 20 cm^{-1} upon binding to a metal ion.[80,84] Key tautomer markers are listed in Table 2.1.

Table 2.1: Expected shifts and assignments of histidine tautomer markers in the vibrationally sparse region.

Tautomer Marker	**Expected Shift (cm^{-1})**	**Assignment**
N^{τ}-H, N^{π}	1568 - 1573	$C^4{=}C^5$ st
	1282 - 1287	$N^{\pi}C^4$ st, C^4C^{β} st, C^5N^{τ} st
N^{τ}-H, N^{π}-**M**	1573 - 1590	$C^4{=}C^5$ st
	1272 - 1277	$N^{\pi}C^4$ st, C^4C^{β} st, C^5N^{τ} st
N^{π}-H, N^{τ}	1583 - 1588	$C^4{=}C^5$ st + N^{π}H bending
	1260 - 1265	C^5H def, C^2H def, $N^{\pi}C^2$ st
N^{π}-H, N^{τ}-**M**	1594 - 1606	$C^4{=}C^5$ st N^{π}H bending
	1434 - 1440	ring st
N^{τ}-H, N^{π}-H	1627 - 1634	$C^4{=}C^5$ st
	1264 - 1269	ring st
N^{τ}-M, N^{π}-**M**	1555 - 1567	$C^4{=}C^5$ st
	1282 - 1292	$C^2N^{\pi}C^4$ st ; $N^{\pi}C^4$ st, C^4C^{β} st, C^5N^{τ} st

Because vibrational spectra can easily be convoluted due to the substantial number of bonds in a protein, the peptide-nanoparticle complex was measured with no enzyme present.

SeNPs were synthesized fresh for each measurement using a borohydride reduction method followed by a peptide conjugation step and subsequent purification. SeNPs were characterized using Raman spectroscopy and Dynamic Light Scattering (See Appendix A Figures A.2 and A.3). DLS showed that SeNPs formed with this protocol arrested around 40 nm in diameter, and Raman data show two characteristic vibrational modes at 234 cm^{-1} and 252 cm^{-1}, indicative of amorphous SeNP formation.[85] Raman spectra of the SeBP control sample and the SeBP-SeNP sample were collected as described in Appendix A and are show in Figure 2.2. We tracked the vibrational modes

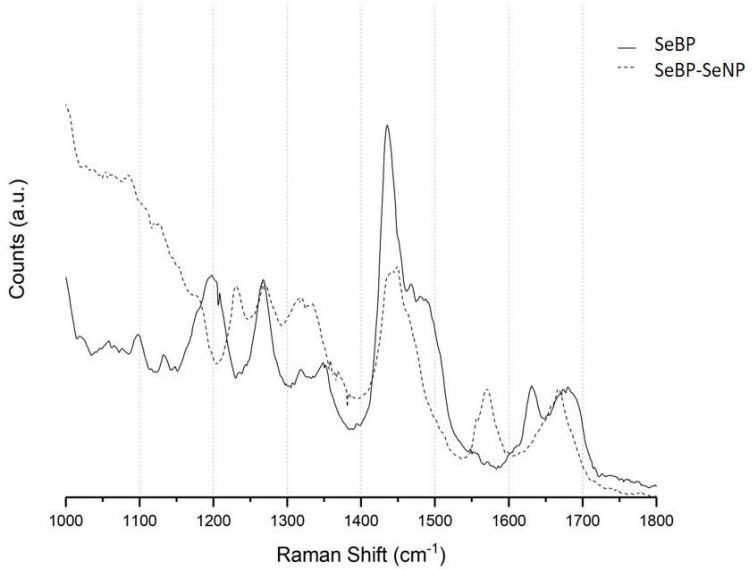

Figure 2.2: Raman spectra of a SeBP film drop-cast from a sample dissolved in pH 7.4 1x PBS (solid trace) and a SeBP-SeNP film drop-cast from a sample dissolved in pH 7.4 1x PBS (dashed trace).

of histidine that correlate with His-metal binding and of the SeBP backbone that have previously shown to correlate with secondary structure conformation.

The spectra were expanded to regions of interest as shown in Figure 2.3. Above each peak is a representative His structure that is color coded according to the marks on the traces. The 1631 – 1636 cm^{-1} peak of the SeBP control sample correlates with the histidine C^4C^5 stretching mode (shown above in red) that indicates a N^{τ}-H/N^{π}-H protonation state ($HisH_2^+$). This assignment is supported by the presence of the peak at 1268 cm^{-1}, which also corresponds to a $HisH_2^+$

imidazolium ion. Upon nanoparticle conjugation, observed in the SeBP-SeNP trace, the C^4C^5 stretching mode downshifts to a broad peak centered at 1571 cm^{-1}. The region of the trace from 1565 – 1573 cm^{-1} corresponds to a neutral imidazole form (HisH) that is unbound with the N^{τ} tautomer protonated and the N^{π} unprotonated (structure shown in green). The portion of the peak above 1573 cm^{-1} likely corresponds with a metal bound His in the form N^{τ}-H/N^{π}-M (structure shown in orange). This assignment is supported by the shift in the band at 1268 cm^{-1} shown in Figure 2.3. Regarding the tautomer form N^{τ}-H/N^{π}-M, upon metal binding the band splits into two sets of peaks with one at 1267 cm^{-1} and one set at 1271/1273 cm^{-1}. The 1267 cm^{-1} band is attributed to HisH in the form N^{τ}-H and unbound N^{π} (structure shown in blue), whereas the 1271/1273 cm^{-1} band correlates with a N^{τ}-H/N^{π}-M form (structure shown in orange), which agrees with the findings from Takeuchi *et al.* (2003). The peak at 1556 cm^{-1} in Figure 2.3 is likely due to a metal

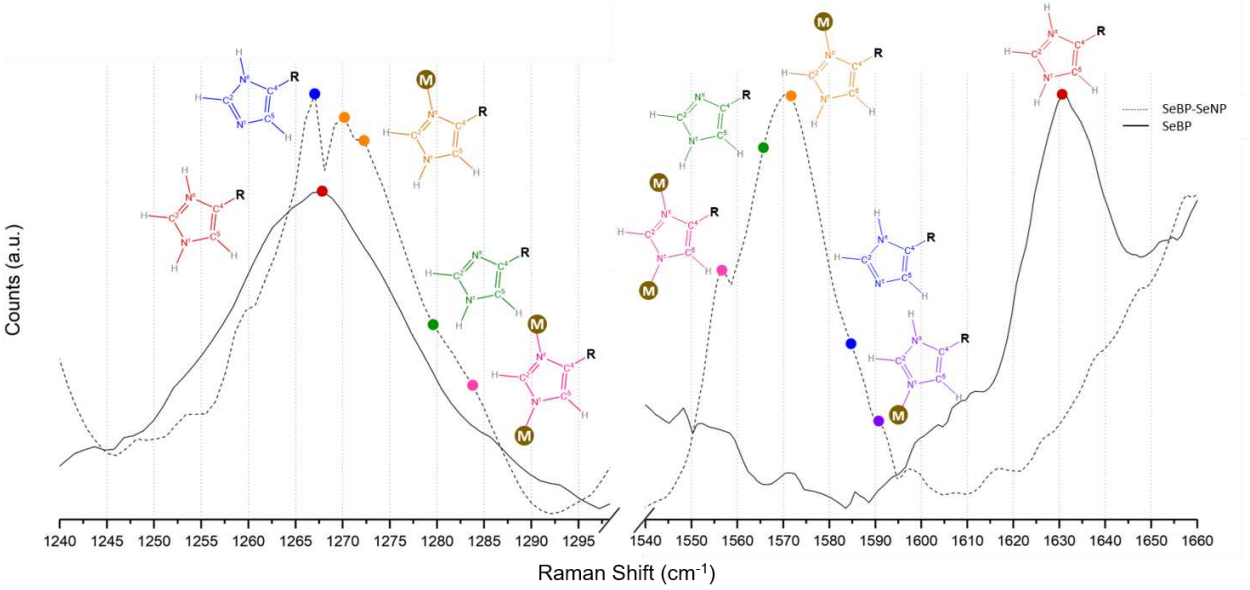

Figure 2.3: Raman spectra of SeBP (solid trace) and SeBP-SeNP (dashed trace). The spectra are focused on regions of His tautomer markers. Specific His modes are shown above the spectrum and color coded with the marks (red = N^{τ}-H/N^{π}-H; purple = N^{τ}-M/N^{π}-H; blue = N^{τ}/N^{π}-H; orange = N^{τ}-H/N^{π}-M; green = N^{τ}-H/N^{π}; pink = N^{τ}-M/N^{π}-M).

bridging form of His (N^{τ}-M/N^{π}-M) with the corresponding peak arising at 1284 cm^{-1} (structure shown in pink).

Additionally, we tracked the amide I and amide III backbone modes of SeBP to observe conformational changes that occurred upon conjugation to SeNP. The amide I backbone mode is located in the 1600 – 1700 cm^{-1} region and is comprised mainly of C=O symmetric stretching with contributions from an out-of-phase CN stretching, $C^{\alpha}CN$ deformation, and NH in-plane bending.[86–92] This mode is considerably influenced by transition dipole coupling, which describes the conformational dependence of the dipole interaction energy on spatial separation and orientation.[86,92] The amide III mode, also sensitive to structural rearrangement is located in the 1200 – 1320 cm^{-1} region and mainly involves an in-phase combination of CN stretching coupled with NH in-plane bending with some influence from $C^{\alpha}C$ stretching and C=O in-plane bending.[86,91,92] Figure 2.4 has been expanded to these two regions. In the control trace (no SeNPs), the inherent broadness and location of the amide I mode from 1650 – 1710 cm^{-1} is suggestive of an unordered backbone structure. When SeBP is bound to SeNPs, the peak narrows and downshifts to 1667 cm^{-1}, which correlates with a mainly β-sheet type backbone structure. The conformational assignment of the backbone mode before and after SeNP conjugation can be confirmed by observing the amide III mode in the 1200 – 1320 cm^{-1} region as also shown in Figure 2.4. In the control trace, when SeBP is not bound to SeNPs, the mode is convoluted by the His modes centered at 1268 cm^{-1} (Figure 2.3 solid trace). An amide III mode centered about 1260 cm^{-1} suggests an

unordered structure, and one that is centered at 1265 cm^{-1} is suggestive of either an α-helix or a polyproline II (PPII) type structure as shown by the black mark on the solid trace in Figure 2.4. The presence of PPII structure is likely, since the peptide contains a Pro residue that causes this shift. Upon binding to SeNP, the amide III mode downshifts to 1230 cm^{-1} shown by the grey mark on the dashed trace in Figure 2.4, which confirms a β-sheet structure.

After confirming that cSeNP was capable of covalently binding to SeNPs via the SeBPs, we tested whether it also imparted size control to the functionality of the tag. We first measured the particles formed using the WT versus cSeNP with dynamic light scattering (DLS). From these experiments, it was observed that cSeNP was able to greatly control the size of the SeNPs formed (~80 nm) when compared to the WT that formed particles is the micron regime (see Appendix A Figure A.4).[78]

To correlate the size differences observed in DLS, S(T)EM was done on particles synthesized with a wide concentration range of $HNaSeO_3$ (40 µM – 10 mM) using cSeNP and WT (Figure 2.5). Upon analysis, we observe that cSeNP forms particles with size distributions (PSD)

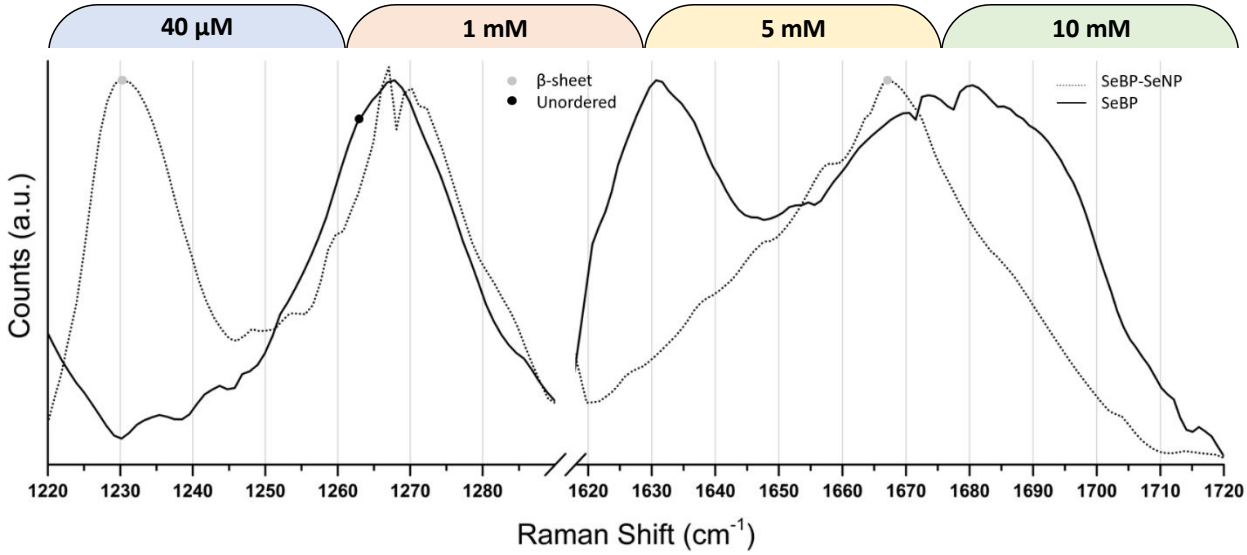

Figure 2.4: Raman spectra of SeBP (solid trace) and SeBP-SeNP (dashed trace) expanded to the amide I and amide III regions. The black and grey marks are centered upon modes correlated with an unordered structure or a β-sheet structure, respectively.

of 37.38 ± 5.75 nm (n = 533), 32.60 ± 6.29 nm (n = 546), 37.34 ± 7.12 nm (n = 1288), and 45.89 ± 6.98 nm (n = 694) when reacted with 40 μM, 1 mM, 5 mM, and 10 mM $HNaSeO_3$, respectively. Similarly, the WT PSD is 48.48 ± 17.63 nm (n =1078), 61.59 ± 24.99 nm (n = 846), and 59.92 ± 21.19 nm (n= 1172) when reacted with 1 mM, 5 mM, and 10 mM $HNaSeO_3$, respectively. From the WT sample reacted with 40 μM $HNaSeO_3$, no particle formation was observed and only salts remained as is seen in Figure 2.5E. From the PSD and S(T)EM images shown in Figure 2.5, we confirm that cSeNP is able to maintain much smaller SeNPs sized ca. 35 nm whereas the particles synthesized with the WT grow much larger (>80 nm) and cluster into micron sized aggregates.

The particle size distribution (PSD) can be explained both by the ability of cSeNP to act as a capping agent and by LaMer burst nucleation and growth. Firstly, a kinetics study was done to monitor the turnover number of the variant versus WT. Impressively, concatenation of the enzyme resulted in an increased turnover number, k_{cat} = 40 (min^{-1}) for the cSeNP compared to k_{cat} = 23 (min^{-1}) for the WT.[78] Because cSeNP can produce reduced Se much faster, there are many more selenide species available as burst nucleation sites. The increase in nucleation sites causes a much quicker depletion of the remaining selenide species during growth, ultimately leading to smaller particles.[93,94] This can also explain why the WT is unable to produce SeNPs at 40 μM $HNaSeO_3$ shown in Figure 2.5 panel E compared to the cSeNP in panel A, which is able to produce particles at that concentration. The WT is unable to produce enough reduced Se quickly enough to reach the critical concentration required for burst nucleation, and the Se species are oxidized back to a more soluble form rather than nucleating.[94]

In sum, we demonstrated that SeBP improves the ability of GRLMR as a cSeNP tag by imparting both NP conjugation and size control. The SeBP is able to covalently bind to those particles via the imidazole ring of histidine by forming both monovalent and divalent His-SeNP

complexes coupled with conformational changes in backbone structure. It also allows the enzyme to better conjugate to the particles, improving retention from 13% to 82%. Furthermore, because cSeNP acts as a ligand and the kinetics of SeO_3^{2-} reduction the concatemer are apparently faster, it also is able to better control the size of the particles formed. Over a wide range of selenite concentrations, cSeNP arrests the size of the particles to ca. 35 nm.

Outlook

As demonstrated above, cSeNP meets the requirements we have set forth as a viable clonable nanoparticle label. It is able to form SeNPs, conjugate to those SeNPs, and control the size of SeNPs. Moving forward, we hypothesized that upon satisfactorily designing and characterizing the cSeNP, it could be used in a proof-of-concept study to test whether this construct would successfully localize a well-studied protein of interest.

CHAPTER 3: Optimization of a Clonable Nanoparticle Label

The model system we chose for a proof-of-concept study is filamentous temperature sensitive protein Z (FtsZ), a bacterial tubulin homologue that, along with at least 13 other division proteins, aids in cleaving a parent cell into two daughter cells during binary fission through Z ring formation.[95,96] The structure of FtsZ is highly conserved across species, albeit their sequences vary greatly.[95,97] While the C-terminal end is responsible for recruiting small molecules and other division proteins, such as FtsA and ZipA, to tether the filament to the membrane, the N-terminal end is responsible for polymerization with other FtsZ monomers.[95,97,98] The ratio of FtsZ and other division proteins must remain in a delicate equilibrium for cells to divide. If these ratios are altered, membrane cleavage cannot progress.

FtsZ is a GTPase that polymerizes with other FtsZ monomers into 30 – 80 subunit protofilaments that randomly align the cell membrane. When a cell undergoes binary fission, these protofilaments migrate to the midpoint of the elongated cell into a structure known as the Z ring. During Z ring formation, the protofilaments loosely align into disordered helical bundles along the midsection of the cell as shown in Figure 3.1, reproduced with permission from *The Annual Review of Biochemistry*, Lutkenhaus (2007).[95,99] The Z ring acts as a scaffold for other division proteins to bind and provide the constrictive force that cleaves the parent cell into two daughter cells.[100,101] After division, the units disassemble and return as randomly oriented helical protofilaments running along the membrane.

Structurally, the assembly of protofilaments into a Z ring *in vivo* is largely debated. In *E. coli*, some cases show a ring structure composed of several assembled protofilaments, while others argue the protofilaments are loosely arranged along the membrane yet disassembled.[95,98,102,103] Furthermore, there are cases showing the Z ring is composed of a single strand of protofilaments

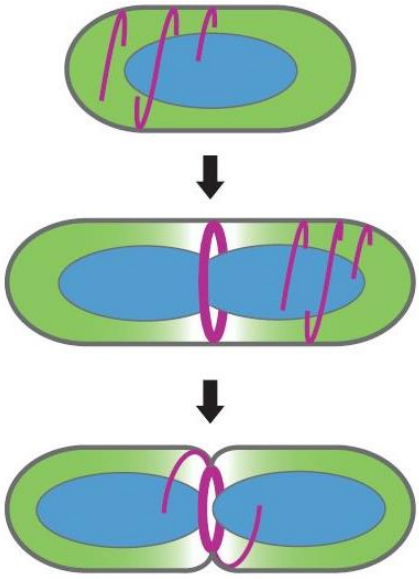

Figure 3.1: Cartoon representation of how FtsZ migrates toward the midpoint of the cell curing binary fission. Reproduced from Lutkenhaus 2007 with the permission of Annual Reviews.

arranged into the Z ring, while others show multiple filaments stacked several units wide arranged at the midpoint.[97] Nonetheless, it is apparent that, on average, FtsZ monomers within the protofilaments are arranged ~7 nm apart and protofilaments are about 16 nm from the inner membrane of the cell and typically extend to 100 nm.[95,103,104]

In fusing cSeNP to FtsZ, we expect to observe filaments decorated with SeNPs as depicted in Figure 3.2. From the studies mentioned, we anticipate that these particles will be closely packed and will traverse the membrane of the cell at the midpoint. We expect that this extensive crowding will cause SeNPs to remain quite small (ca. < 7 nm). Importantly, since we will be using an IPTG inducible T5 expression system, we expect to overproduce the cSeNP-FtsZ chimera within the cell. As mentioned above, affecting the delicate balance of division

Figure 3.2: Cartoon representation of cSeNP forming particles that decorate a FtsZ protofilamnent.

proteins can disrupt Z ring formation and cause cells to become extremely elongated (on the range of 20 – 30 μm compared with the normal phenotype ca. 3 – 5 μm).[29,105] Therefore, in addition to Z rings, we expect to see much larger cells with segments of helical protofilaments forming wave-like patterns along the membrane.[95]

Results and Discussion

The cSeNP-FtsZ chimera was fused using $(EAAAK)_2$ as the linker. The construct was inserted into a pD441-CH expression vector and transfected via heat shock into BL21 (DE3) competent *E. coli* and grown in petri dishes on antibiotic-containing solid LB medium. After growth, several stabs of cells were taken and grown up again to confluency in liquid LB containing antibiotics. Cultures were then taken and stored as glycerol stocks until needed. Details of culture growth and storage can be found in Appendix B.

Two cSeNP-FtsZ constructs were made by labeling either the C-terminal end or the N-terminal end of FtsZ. As noted previously, both termini play important roles in the function of FtsZ. Also, it has been observed that constructs made with GFP were not always functional. Thus, it was necessary to label both ends since we could not be sure that by tagging one end we would not disrupt the function of FtsZ.

For *in vivo* induction experiments, beginning with the construct where cSeNP is fused to the C-terminal end of FtsZ (FtsZ-cSeNP), we set our parameters based on previous studies of FtsZ as well as on SeNP formation. As was seen in Chapter 2, because cSeNP is able to synthesize SeNPs within 30 minutes (see Appendix A Figure A.4), we ensured that IPTG expression was initiated for at least 30 minutes. As a visual confirmation, once the cells are pelleted, a color change from yellow to red is observed in the culture. On the other hand, because we do not want to perturb the function of FtsZ with an excessively large SeNP, our ideal particle growth would be 5 nm. To

this end, cultures may not appear as vibrant red as was observed in the original studies where particles averaged ca. 80 nm.[57]

Several factors were tested towards optimizing chimera expression and nanoparticle formation (i.e. the "Goldilocks" parameters). Initially, we screened induction times and temperatures that would produce the most division points within cells analyzed with SEM. Times from 5 minutes up to 16 hours were tested. When these screens were performed at 37 °C, it was difficult to isolate cells during binary fission across all times tested. We attributed this to rapid cell growth and dropped the temperature to 28 – 30 °C to slow that growth rate. When this change was made, we easily isolated dividing cells during log phase growth.

Next, an induction screen was done to determine the optimal IPTG concentration that would allow us to isolate both protofilaments and Z-rings. As had been noted, overexpression of FtsZ can disrupt proper cell duplication due to the imbalance of division proteins. This results in an abundance of protofilaments running throughout the cells in wave-like patterns. To control FtsZ expression, 1 mM, 100 μM, and 10 μM IPTG inductions were performed for 1 hour in the presence of 1 – 2 mM SeO_3^{2-} (1 mM was used for the 10 μM IPTG sample to avoid metal stress) during log phase growth. Both 1 mM and 100 μM IPTG expression produced cells with noticeable contrast in SEM that was distinct from control samples, whereas the 10 μM IPTG sample likely did not produce enough of the chimera to observe obvious contrast in regions where we expected (Appendix B Figure B.2). Comparing the 100 μM sample with the 1 mM sample, we observe a difference in FtsZ expression level by the morphology of the cells. The 100 μM sample results in a moderate expression level of the chimera, where cells are elongated up to 10 μm but not excessively extended to 20 – 30 μm as is shown previously with FtsZ overexpression.[29,105,106] These hyper-extended cells are indeed present in the 1 mM IPTG high expression level sample,

where we also see long filamentous structures with high contrast running throughout the cell (see Appendix B Figure B.3).

Next, we tested optimal selenite concentrations that would produce the most contrast in an electron micrograph while maintaining cell viability. Shown in Figure 3.3 are S(T)EM[b] data of samples overexpressing the chimera in the presence of 250 µM, 1 mM, and 2 mM SeO_3^{2-}. As a control, we grew one sample with no SeO_3^{2-} present shown in Figure 3.3A. Bacteria in the presence of greater than 2 mM SeO_3^{2-} began to appear stressed, and thus the concentration of selenite used for subsequent protocols did not exceed 2 mM (See Appendix B Figure B.4).

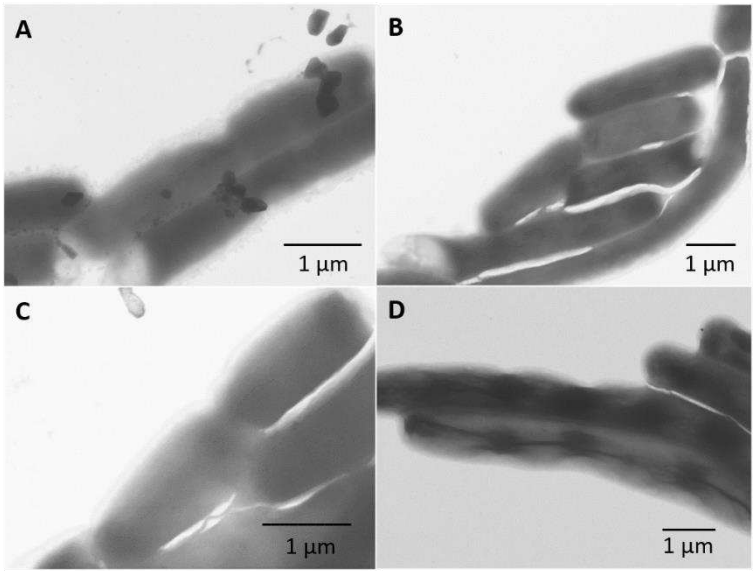

Figure 3.3: Selenite concentration screen. (A) Control incubated with no SeO_3^{2-} (B) sample incubated with 250 µM SeO_3^{2-} (C) sample incubated with 1 mM SeO_3^{2-} and (D) sample incubated with 2 mM SeO_3^{2-}.

From Figure 3.3, we see that by incrementally increasing the concentration SeO_3^{2-}, there is a gradual increase in the contrast observed at the pinch point of the cell. Most notable is the sample

[b] A note on S(T)EM and (S)TEM acronyms. In the text, when S(T)EM appears, it represents data collected on a JEOL JSM-650 FE-SEM in scanning transmission mode. The resolution of EDS data collected from this microscope is low with respect to the size of the sample (0.5 µm resolution at best). (S)TEM signifies that the data was collected on a JEOL JEM2100F TEM in scanning transmission mode. Resolution of EDS data collected on this microscope is greatly improved (theoretically, the resolution would be the size of the spot probe, though electron scattering and sample motion reduce this).

incubated with 2 mM SeO_3^{2-}, in which cells appear healthy with distinctive contrast not seen in the control sample. Combining these results, we deciphered the "Goldilocks" parameters, in which incubating the samples with 100 µM IPTG and 2 mM SeO_3^{2-} for 30 – 180 minutes at 30 °C produced optimal growth and contrast within samples. The optimization parameters that were tested are summarized in Table 3.1.

Table 3.1: Parameters for the optimization of FtsZ expression and nanoparticle formation.

[IPTG] (µM)	Induction Time (min)	Temperature (°C)	[SeO_3^{2-}] (µM)
10	5	37	1
100	30	28 – 30	10
250	45	22 – 25	100
500	90		1000
1000	135		1500
	180		2000
	240		2500
	300		3000
	360		4000
			5000

To confirm that the observed contrast was due to Se, we used Energy Dispersive X-Ray Spectroscopy (EDS). Even though the resolution of SEM-EDS is about 500 nm, which is much larger than the average pinch point (about 200 nm), we only looked for an indication that Se was present in the sample. Using micromolar amounts of Se seemed to be insufficient to generate a signal using EDS. By mapping the samples that had been incubated with 2 mM Se in S(T)EM-EDS, we were able to observe a Se gradient (data not shown). We moved this sample to (S)TEM-EDS, and the elemental overlay map is shown in Figure 3.4. The EDS spectrum shows a small amount of Se present by observing the K line close to 11.2 keV (see Appendix B Figure B.5). The individual elemental maps are shown in Appendix B Figure B.5. It is clear that a localized concentration of Se is present at the division point of the cell as we expect. Along with the obvious

points of contrast observed in EM images, using EDS we were able to conclude that the tag was retaining Se and was associated with FtsZ at the expected locations.

Noticeably, while samples incubated with higher concentrations of SeO_3^{2-} would exhibit

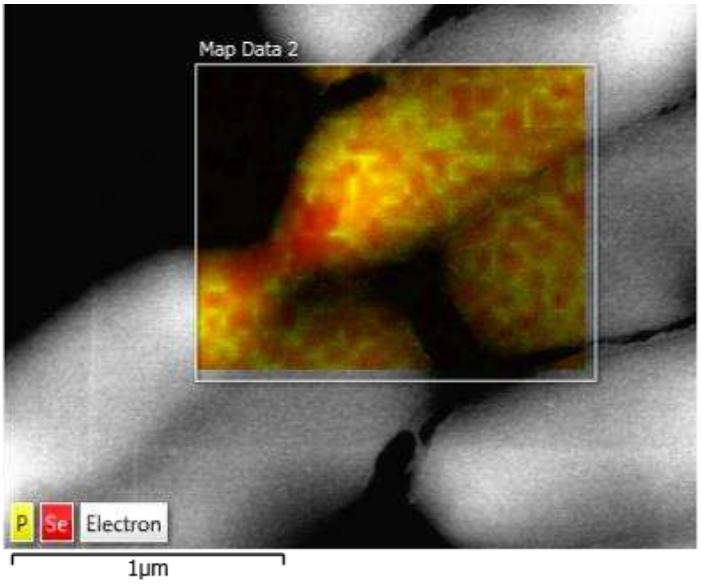

Figure 3.4: (S)TEM-EDS analysis of an *in vivo* sample prepared with 100 µM IPTG and 2 mM SeO_3^{2-}. Maps: yellow indicates phosphorus and red indicates selenium.

high contrast areas at locations we expect, the particles were indistinct. Thus, a "Red Sonja" protocol favoring the growth of large SeNPs was conducted to ensure particle formation *in vivo*. In the presence of 1 mM SeO_3^{2-} and 100 µM IPTG, cells were induced for 3, 4, 5, and 6 hours seen in Figure 3.5. From this experiment, obvious particle formation was not observed until hour 5, and importantly, the formation of particles was inconsistent as seen in Figure 3.5D, where particles are quite punctate in the center cell but indistinct in the surrounding cells. It is possible that the inconsistency in particle formation was due to the extended induction time, as previous experiments have shown that FtsZ begins to degrade after 3 hours. However, from Figure 3.5A we do not notice large, punctate particles as we expect given the time allowed for particle formation.

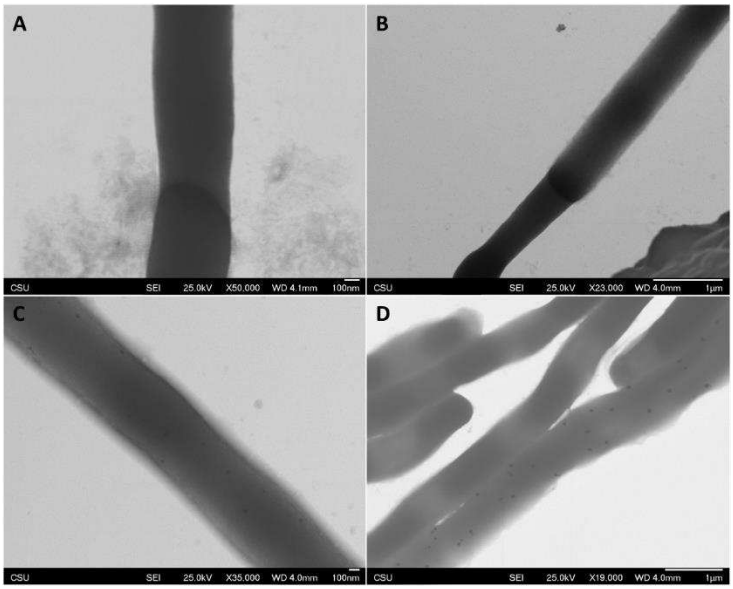

Figure 3.5: Extended induction in 1 mM SeO_3^{2-} and 100 µM IPTG for (A) 3h (B) 4h (C) 5h (D) 6h.

We mentioned that GRLMR is the fastest Se-reducing enzyme in the world, and in our studies confirmed that the recombinant variant can form 40 nm particles in 30 minutes, which indicates that we should be forming SeNPs under these conditions. Of note, it has been observed in literature that FtsZ-GFP fusions labeled from the C-terminus are not fully functional *in vivo*, which could be due to the inability of FtsZ to properly tether to the membrane.[95] Thus, if FtsZ is not properly functioning, the degraded protein could also cause hinder the function of cSeNP and formation of SeNPs.

To improve the activity of the chimera, we moved the cSeNP from the C-terminus to the N-terminus of FtsZ (cSeNP-FtsZ). Experiments were repeated by inducing cultures with 1 mM IPTG and 2 mM SeO_3^{2-} for 1 and 2 hours and are shown in Figure 3.6. The control sample does not contain any SeO_3^{2-} and is shown in Figure 3.6A and 3.6D, in which we see no distinct particle formation. One sample was incubated with SeO_3^{2-} for 1 hour as seen in Figure 3.6B and 3.6E, in which we begin to see small particles forming throughout the cell and also at the pinch points. In

the sample marinated with SeO_3^{2-} for 2 hours, particles become much more distinct as illustrated in Figure 3.6C and 3.6F.

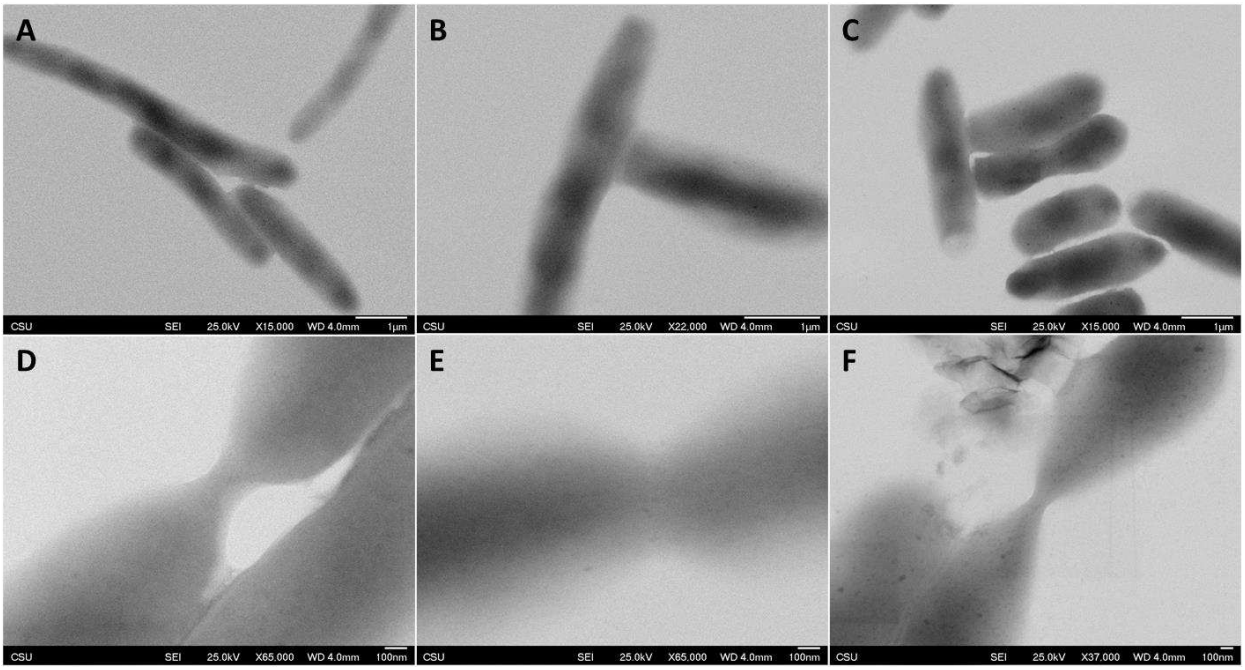

Figure 3.6: N-Terminal construct induction. (A&D) control (B&E) sample incubated with selenite for 1 hour (C&F) sample incubated with selenite for 2 hours.

Elemental analysis was done using (S)TEM on a sample induced in the presence of 1 mM SeO_3^{2-} and 100 µM IPTG for 1 hour, where both large internal particles and pinch points were analyzed. We confirmed that both maps contained Se as is shown in Appendix B Figure B.7.

Inspired that the chimera was now functional, an additional experiment was conducted to test whether expressing the chimera for an extended period of time before adding SeO_3^{2-} would have a significant impact on particle formation. To test this, cells were grown in 10 µM IPTG and 1 µM SeO_3^{2-} overnight for low expression of the chimera. Following, a ramp up was done where either 250 µM or 100 µM IPTG and 2 mM SeO_3^{2-} (none for the control) were added to cultures for approximately 2 hours. The two different concentrations of IPTG represent two distinct levels of expression as was tested previously.[106] High expression level is shown in Figure 3.7A (control) and 3.7B, where cells are elongated and extremely filamentous determined by apparent cell

thickness. In Figure 3.7C, cells are also elongated but are not as filamentous, as is deducted by the lower level of contrast throughout the cell and at specific points where cleavage furrows seem to be forming.

Shown in Figure 3.7D-F are higher magnification images of the high express control (D), the high express sample (E), and the low express sample (F). In the control, it is possible that ultrasmall SeNPs are being formed, since it was necessary to supplement the medium with 1 µM SeO_3^{2-} to avoid cell death due to the prolonged expression period. Nonetheless, there is far less contrast in the control compared with the high express sample incubated with 2 mM SeO_3^{2-}. As is apparent in Figure 3.7E, obvious SeNP formation is observed along the edge of the membrane and also along the filaments as expected. Finally, in the low expression sample, the particles are much more distinct along the membrane and at the division points within the cell (Figure 3.7F).

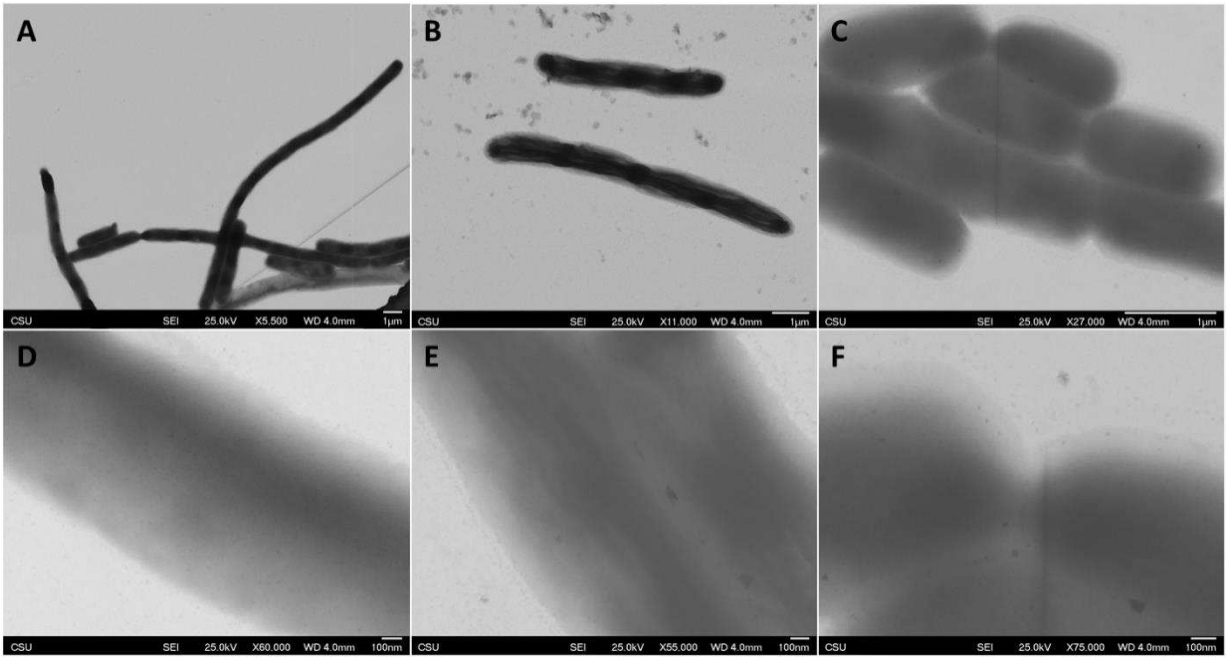

Figure 3.7: Extended expression experiment. Low magnification images of the control (A), the sample induced with 100 µM IPTG (B), and the sample induced with 250 µM IPTG (C) are shown in the top row. Higher magnification images of the control (D), the sample induced with 100 µM IPTG (E), and the sample induced with 250 µM IPTG (F) are shown in the bottom row.

While the extended expression greatly affects the number and length of filaments within the cell, it is unclear whether or not there is a significant impact on particle formation. In both Figure 3.6 and 3.7 we observe punctate particles in areas that we expect. Thus, we determined that either method could be used for the next phase of the project, which ultimately entailed generating tomograms of particle-aligned filaments. Accomplishing this required that we slice open the bacteria to better resolve the particles within. Because the cells are 500 – 800 nm thick, even at our maximum available accelerating voltage of 200 kV, the electron beam cannot transmit completely through the sample. Therefore, we must prepare the cells in resin that can be cured into plastic blocks. This process involves a serial dehydration, normally done in acetone, followed by infiltration in resin and curing under low heat (37 – 60 °C) over a 1 – 10 day period depending on conditions. Experimental details can be found in Appendix B.

We prepared samples induced with 100 μM IPTG and 2 mM SeO_3^{2-} for 2 hours. After the induction period, we performed a high-pressure freeze followed by freeze-substitution into a glutaraldehyde/acetone cocktail for simultaneous fixation and dehydration. After dehydration, the sample was infiltrated using an epoxy-based resin followed by a low temperature cure. The results from this experiment are shown in Figure 3.8. The overview of the sample is given in panel A, where we see a typical view of the sample in light grey along with a few odd cells appearing as dark grey entities. During sample processing, it is possible for some cytoplasmic bodies to pop out of their cellular membranes, resulting in smaller anomalies appearing on top of the sections that have not been exposed to acetone or glutaraldehyde. Viewing Figure 3.8B and 3.8C, it is clear that in the normal cell bodies, there do not appear to be punctate SeNPs like we saw previously in Figures 3.6 and 3.7. However, upon inspection of the cytoplasmic bodies shown in Figure 3.8D and 3.8E, we do observe ~5nm particles running throughout the entity. SEM-EDS was done on

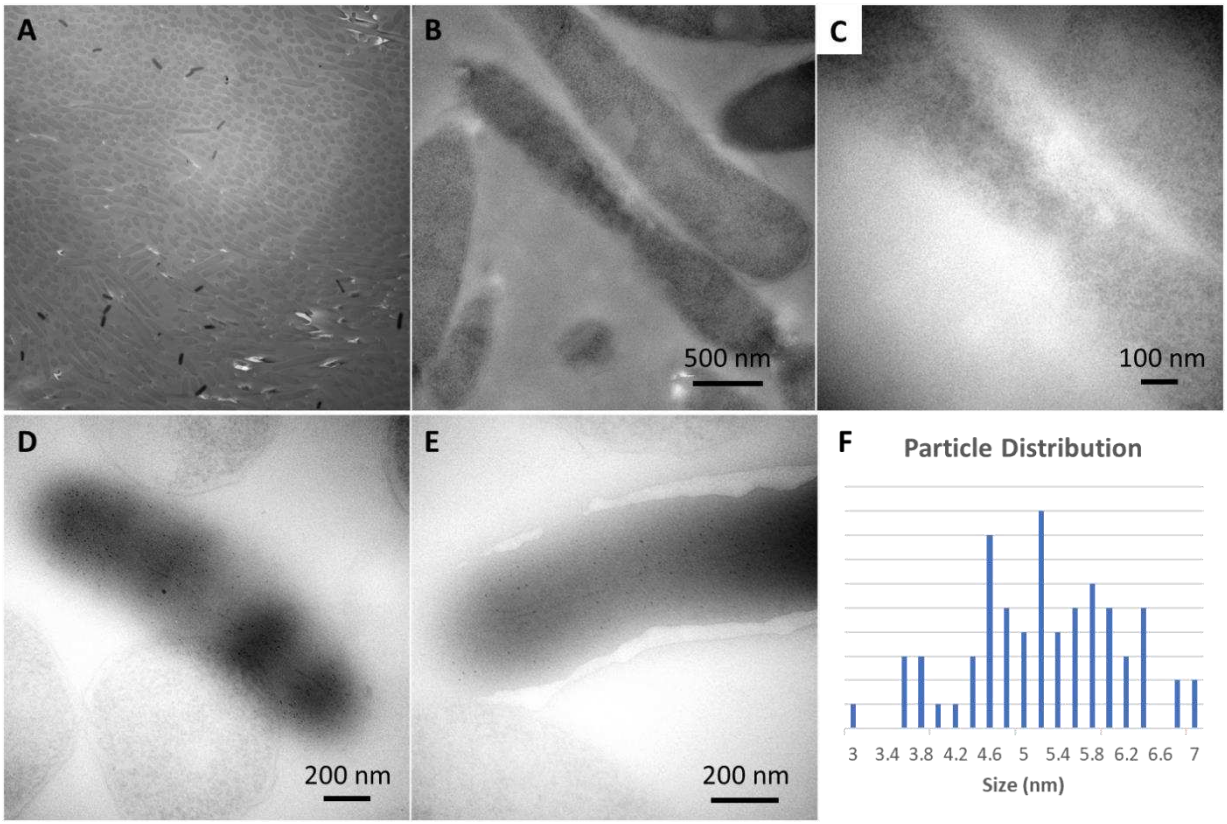

Figure 3.8: (A) Low magnification overview of the sample. (B) higher magnification view of a midpoint where we expect FtsZ to localize. (C) The pinch point of a cell is in full view where FtsZ is expected to localize. (D&E) Images of cytoplasmic bodies. (F) A particle distribution graph of a small sample of particles (n = 70) observed in the cytoplasmic bodies.

the cytoplasmic bodies, as one is boxed in white shown in Figure 3.9. Looking at the elemental maps, these anomalies are Se rich and P poor, which further supports that these bodies are cells that contain SeNPs and that have popped out of their membranes.

Comparing the samples prepared using high pressure freeze-substitution (HPFS) and embedment versus chemically fixed samples, it is clear that somewhere downstream during sample processing, the SeNPs are degrading. We suspected that acetone could be causing this degradation, since this solvent was not present during the initial whole cell experiments. To test the stability of SeNPs in acetone, a dissolution study was performed, mimicking a typical freeze substitution temperature ramp. SeNPs were synthesized via a borohydride reduction method as described in Appendix A and transferred into 100% acetone that had been prechilled to -80 °C using dry ice

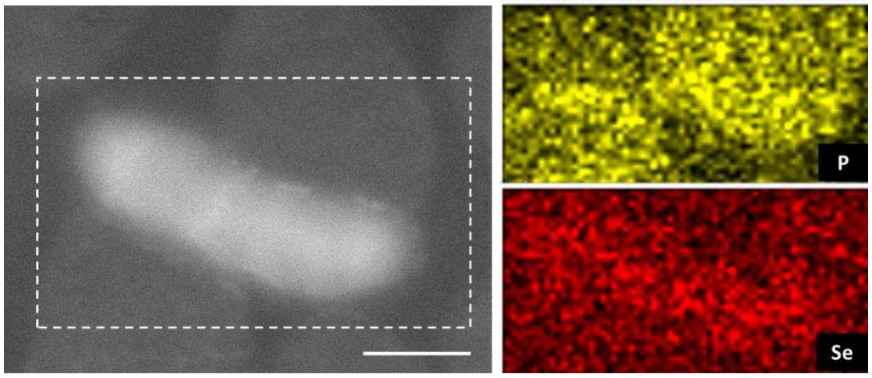

Figure 3.9: SEM-EDS analysis of cytoplasmic bodies boxed in white. Elemental mapping shows that the bodies are Se rich and P poor, indicating that these bodies have popped out of their membranes and contain SeNPs.

and immediately placed in a -80 °C freezer for 5 days. At this temperature, particles remained stable and unchanged. Once the particles were brought back up to room temperature, they dissolved in acetone within 1 – 2 hours as denoted by a color change from red to colorless.

To understand why the particles are dissolving, we need to understand their structure. Amorphous SeNPs are composed of polymeric Se_n chains and Se_8 rings that pack together via van der Waals forces, and the charge state of Se atoms within these polymeric chains is either 0, -1, or -2.[94,107,108] Se^0, the predominant species, is insoluble in water, which is likely attributed to the dominating forces in water being dipole-dipole interactions.[76,107] If the water is removed from the system and replaced with a nonpolar solvent like acetone, the dominant forces become dispersive. As acetone intercalates into SeNPs, polymeric Se subunits experience these dispersive interactions and slowly dissolve into the acetone. At low temperatures, it is possible that polymeric Se packs more tightly together, negating the diffusion of acetone into the particles. However, it is clear that once a certain temperature is reached, the space between Se subunits is great enough for acetone to again intercalate into the particles.

To observe this dissolution, an experiment was done to test the degradation of the SeNP surface when exposed to acetone for 5 minutes and 20 minutes. Shown in Figure 3.10, when comparing SeNPs that have not been exposed to acetone (Figure 3.10A) versus those that have been exposed for 5 minutes (Figure 3.10B), the acetone-exposed particles appear to contain much less mass as is obviated by the lesser contrast. When further comparing the SeNPs exposed to acetone for 5 minutes versus 20 minutes (Figure 3.10C), we see that particles begin to aggregate and grow, as it seems at this point most of the smaller particles have either dissolved or fused into larger particles following an Otswald ripening mechanism. We suspect that eventually these larger particles will also dissolve in accordance with the visual observations noted previously.

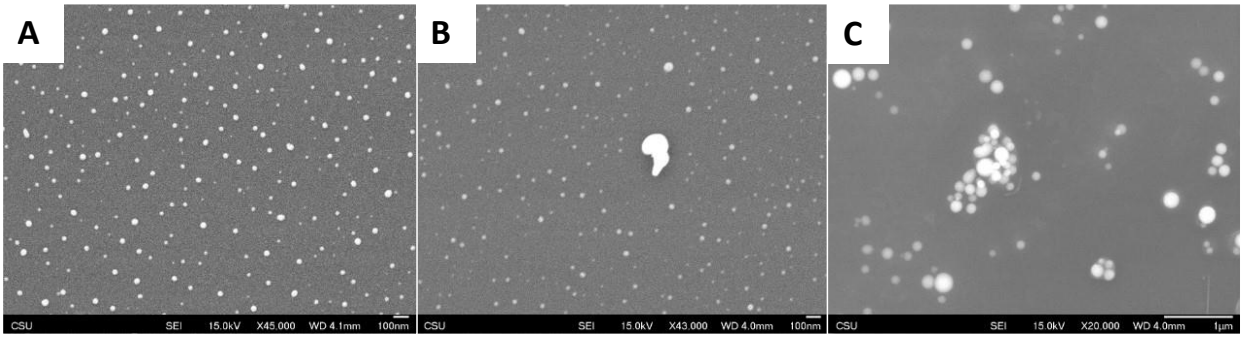

Figure 3.10: Acetone dissolution trials. (A) SeNPs before exposure to acetone, (B) SeNPs exposed to acetone for 5 minutes, and (C) SeNPs exposed to acetone for 20 minutes.

Subsequently, it was necessary to modify the preservation procedure to avoid SeNP dissolution. Ethanol is another common solvent used in embedment procedures; however, it is not miscible with the epoxy-based resin use in this study. Instead, a transition solvent that is miscible with the resin must be used following dehydration. Thus, we repeated the induction experiments above by adding 1 mM IPTG and 1 mM SeO_3^{2-} to cultures (1 µM SeO_3^{2-} to the control) for 3 hours. For preservation, we replaced acetone with ethanol for dehydration and propylene oxide was used as a transition fluid to resin followed by curing.

Results are shown in Figure 3.11, in which the top row depicts the control sample, and the bottom row shows the sample incubated with 1 mM SeO_3^{2-}. Upon inspection it is clear that there are not punctate particles. However, as is apparent in the bottom row, long filamentous structures seem to be highlighted compared to the control. We suspect this is a form of Se that has been transformed from a particle structure to something that resembles a localized metal stain. To confirm that the contrast was due to some form of Se, (S)TEM-EDS was done on one of the high contrast cells as is shown in Figure 3.12. From the data, Se is in fact present within the high contrast

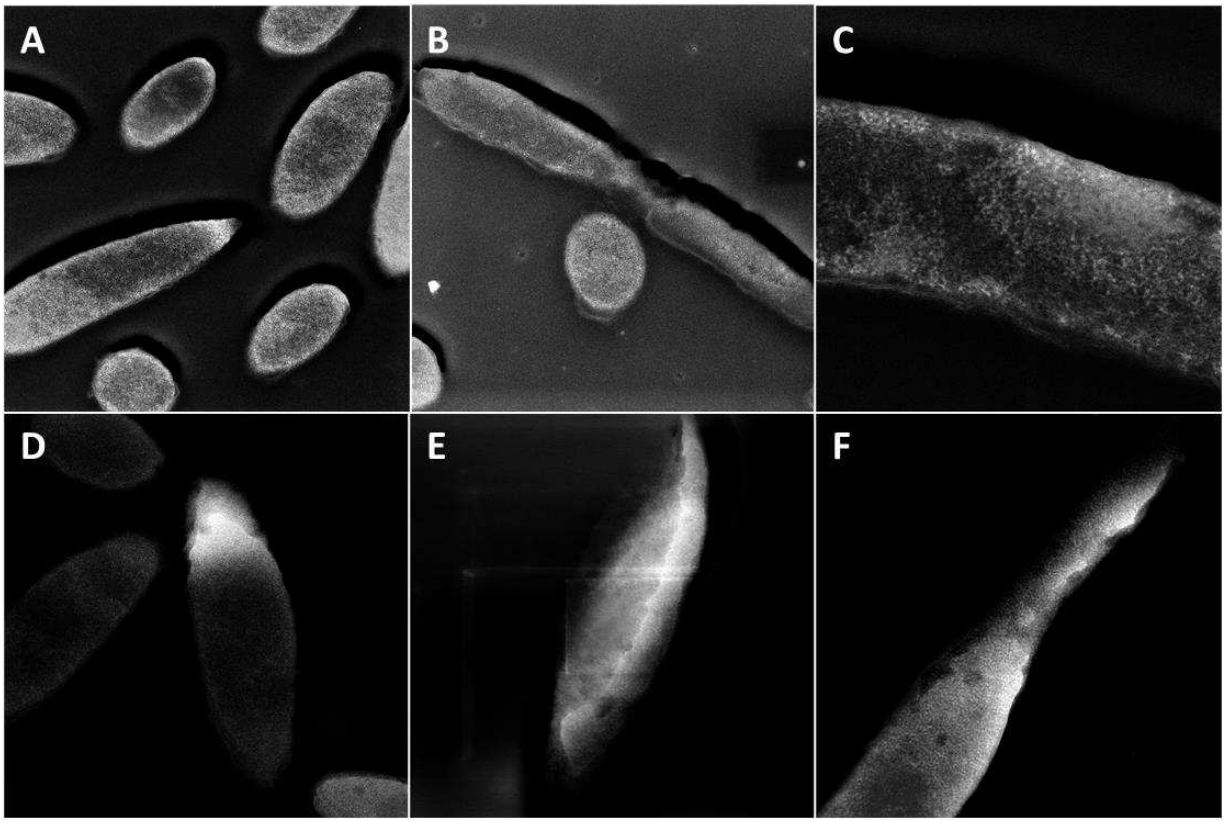

Figure 3.11: Results from the modified embedment procedure using propylene oxide as a transition solvent. (A-C) Images of the control and (D-F) images of the sample incubated with 1 mM selenite are shown.

region of the cell. From this we hypothesize that SeNPs are still degrading, albeit more slowly, despite switching from acetone to an ethanol/propylene oxide solvent system. We believe at this point the propylene oxide is causing the more significant dissolution of particles. Therefore, we

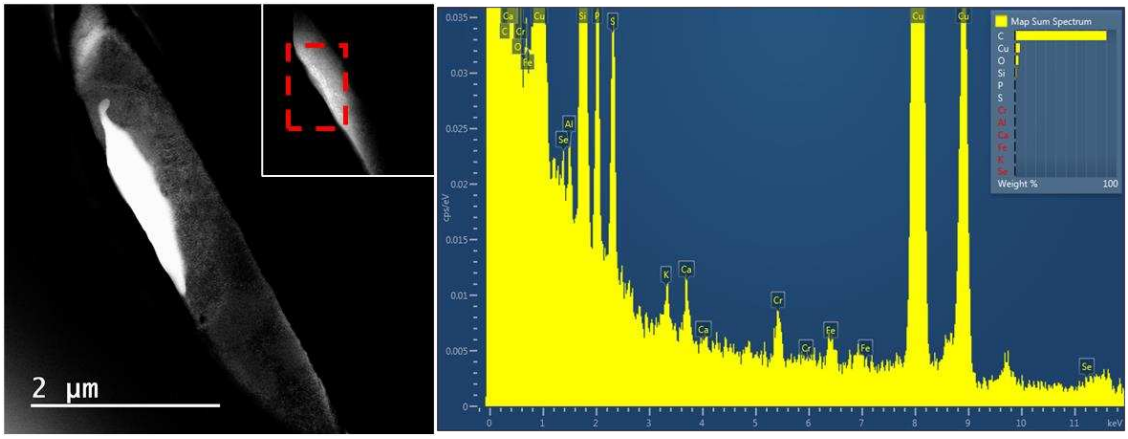

Figure 3.12: Image from the sample incubated with 1 mM selenite. The inset is a higher magnification view of the high contrast area, with the contrast a brightness greatly decreased to avoid saturation. To the right is an X-ray spectrum of the area boxed in red of the inset image.

modified the infiltration step by omitting the propylene oxide transition fluid, despite the immiscibility of the resin in ethanol.

The importance of the transition solvent is to ensure proper infiltration of the resin. This usually occurs with 3 changes of a gradual dilution of the transition fluid into complete resin over the course of 3 – 6 hours depending on the sample. By omitting this solvent, we must **greatly** increase the amount of time the sample spends in the exchange from ethanol to complete resin to ensure proper infiltration. Thus, the sample is taken from 100% ethanol to a 1:1 mixture of 100% ethanol to uncatalyzed resin, in which the ethanol is allowed to slowly evaporate off over the course of 16 – 18 hours followed by an additional 4 – 8 hours in uncatalyzed resin before moving the sample into complete (catalyzed) resin. **In sum, we turn a 3 hour step into a 20 hour step by omitting the transition solvent.**

The sample was made using the method described above. In this instance, propylene oxide was omitted from the embedment process and the results are shown in Figure 3.13. It does appear that by omitting the transition solvent we are able to preserve the larger SeNPs being formed as can be seen in the images. Notably, there do not appear to be many particles in the 5 nm regime. Looking at panel C, we again notice what looks to be a metal stain lining a filamentous structure

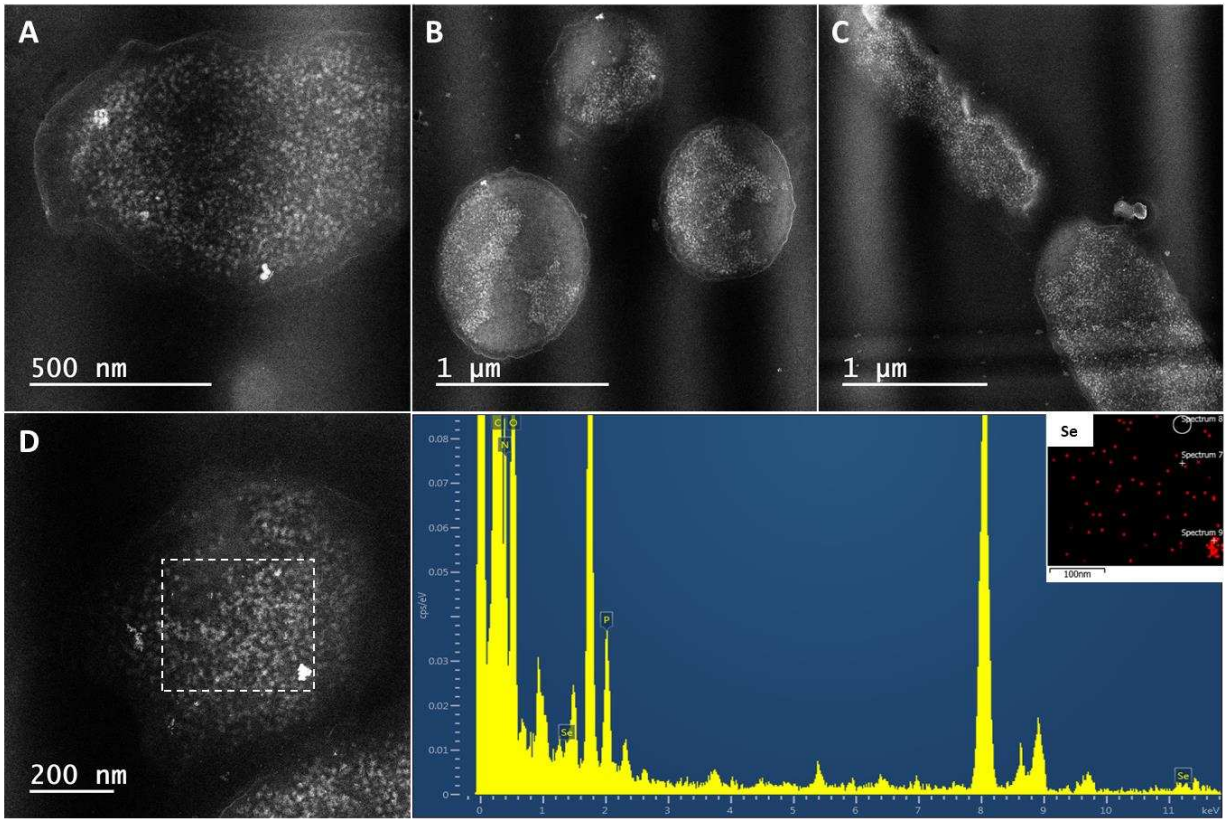

Figure 3.13: Images of the sample incubated with 1 mM seleniite preserved using an ethanol only embedment protocol (A-D). Also shown is an X-ray spectrum and the Se elemental map of the white boxed area shown in D.

versus discrete particles. It is possible that the now metal stain once was composed of many ultrasmall particles (5 nm or less in diameter) but has since somehow degraded into the contrast seen. Additionally, to confirm that the larger particles are composed of Se, EDS was employed on the cluster boxed in white as shown in the example in Figure 3.13D along with the spectrum shown. A trace amount of Se is observed, and the Se elemental map is shown in the inset of the spectrum. It is possible that these small particles are degrading in ethanol during the greatly extended time required by the modified procedure to ensure proper resin infiltration.

On the other hand, it has been shown previously that the surface of amorphous SeNPs can "soften" above 40 or 50 °C.[109] This is shown in Figure 3.14, reproduced from Jeong *et al.* (2005).[109] In Figure 3.14A are 300 nm SeNPs and in panel B are the same particles that have been annealed at 40 °C for several hours. Over time it appears that the particles have begun to fuse together as

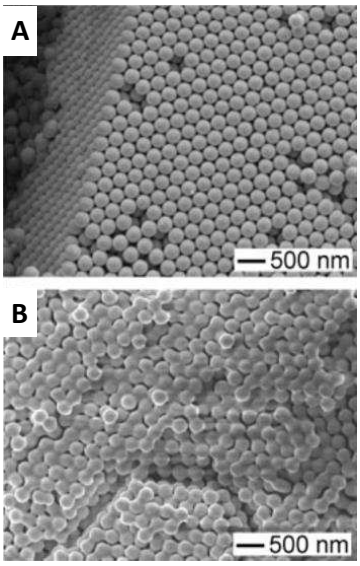

Figure 3.14: (A) SeNPs before thermal annealing and (B) SeNPs after annealing at 40 °C for several hours. Reproduced with permission from Jeong et al. (2005) and Advanced Materials of Wiley Publishing.

seen by the necks forming between the particles. Therefore, looking back at Figure 3.13C, it could also be possible that curing, which occurs at 60 °C for 16 hours, is causing the ultrasmall SeNPs that are packed closely together to slowly "soften" and fuse. However, it is unclear how the presence of the resin would affect the fusing of particles, and it is uncertain whether it is actually the elevated temperature that is causing the appearance of hazy structures or if ethanol is promoting a slow dissolution of particles.

Thus, we repeated the sample preparation from before and employed a lower temperature cure (42 – 45 °C over 3 days). The results of this experiment are shown in Figure 3.15. In both cases, we begin to make out ultrasmall, ~2 nm particles arranging into the wave-like patterns that we expect. However, the particles are not very distinct against the background of the cell. This could be due to the thickness of the section, which is 100 nm in A and 50 nm in B. The particles do appear a bit brighter in the 50 nm slice. However, in both cases still the particles are not as

obvious as is desired since when viewing the sample at low magnification, the particles are not apparent.

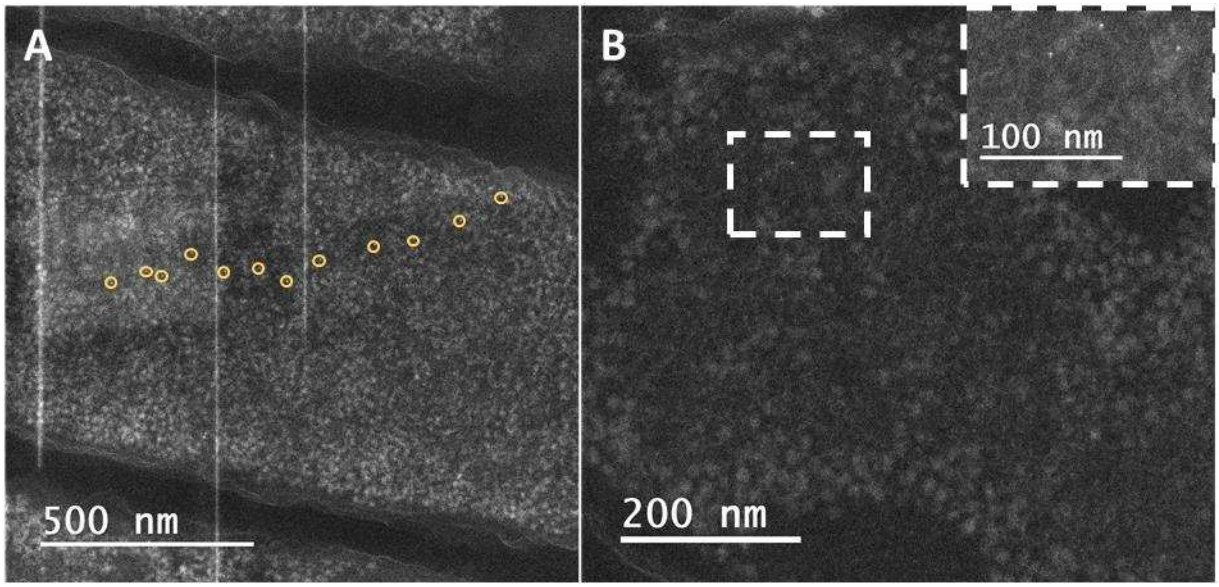

Figure 3.15: Sample preparation cured at a lower temperature (42 – 45 °C) for 3 days. (A) Circled in yellow are what appear to be ultrasmall particles from a 100 nm semi-thin section. (B) Boxed in white are other ultrasmall particles, blown up in the inset, from a 50 nm thin section.

In sum, through an exhaustive optimization of induction parameters, particle formation parameters, and preservation trials, we only seem to be able to distinguish either ultrasmall, 2 nm particles running throughout the cell or much larger, ca. 20 nm particles. It is likely that the 20 nm particles are too large and hinder the function of FtsZ, preventing it from polymerizing with other FtsZ monomers and possibly from tethering to the membrane. This could explain why when larger particles are observed, at times they are not surrounded by other particles. Nevertheless, it is apparent that traditional cellular preservation methods are not suitable for amorphous SeNP preservation. Therefore, we must find alternative ways of protecting SeNPs from the processing liquids used therein.

Outlook

The ultrasmall particles would indeed meet the size criteria to allow FtsZ to function normally, and it may well be that if a tilt series is collected, they would be much more

distinguishable. In this case, it would be worthwhile to collect tomograms of this sample. On the other hand, if the ethanol is dissolving some (but not all) of the particles, the tomograms might reveal incomplete evidence for FtsZ filamentation. Therefore, it is crucial to repeat the experiments done to date with nanoparticles that will not dissolve in the processing medium.

CHAPTER 4: Stabilization of Amorphous SeNPs via Disproportionation into MSeNPs

Introduction

From the studies detailed in Chapter 3 and from previous reports, it is clear that amorphous SeNPs are quasi-stable particles that will either degrade or convert to the stable trigonal phase over time.[107] In continuation of developing a clonable nanoparticle tag, it is important to ensure that the particles will remain intact throughout the duration of the experiment. We are left with two options: either 1) we post-synthetically crystallize the amorphous Se into trigonal Se or 2) we synthesize a metal selenide material *in situ*.

Pursuing option 1 is not ideal, since typical crystallization protocols require temperatures that would destroy biological materials.[110,111] Thus we are left with option 2: to synthesize a metal selenide nanoparticle rather than amorphous SeNPs. In previous work, we have shown that GRLMR is able to reduce Se^{4+} all the way down to the 2- state before being swiftly oxidized to zerovalent Se, which allowed us to nucleate Se^{2-} with Cd^{2+} to form CdSe quantum dots *in vitro*.[112] When transferring this reaction *in vivo*, Se^{2-} species are quickly oxidized by other small molecules such as O_2 and glutathione, which greatly impedes the rate of the reaction (30 minutes *in vitro* versus 16 hours *in vivo*), and the required redox state for spontaneous Cd^{2+}/Se^{2-} nucleation is lost. What also may affect QD formation is the effect of dual metal stress. In higher organisms, it has been observed that increased concentrations of certain trace elements affects the uptake of other metals.[113] Thus, the simultaneous addition of Cd^{2+} to the culture medium could hinder the uptake of SeO_3^{2-} *in vivo* and vice versa.

Another approach could be to post-synthetically transform GRLMR-produced SeNPs into metal selenide (MSe) NPs under mild conditions. In reviewing traditional MSeNP syntheses, and in particular CdSe, ZnSe, and Ag_2Se, most rely on either a co-reduction approach in organic

solvents at relatively high temperatures or laser ablation (>100 °C).[114–118] There have been few reports that use trigonal SeNWs as templates for transformation into a shelled SeNW@MSe, and in the case of Ag this reaction is possible at room temperature.[119–124] While this approach is mild, Ag can be difficult, yet not impossible, to work with in a biological setting. It can precipitate with either Cl or inorganic P, and it is easily reduced with GSH.[125] Consequently, it is appealing to synthesize MSe particles from metals that are more biologically relevant.

What has not been extensively explored is reactions that use amorphous SeNPs (a-SeNP) as precursors in an aqueous medium. It is known that a-Se is composed of Se_8 rings and Se_n chains in an intraparticle quasi-equilibrium of one and two electron propagation causing constant breakage and reformation of Se-Se bonds.[85,126] The instability of a-Se results in the eventual rearrangement of the amorphous allotrope to either a trigonal or monoclinic crystalline phase. To this extent, we hypothesized that it is possible to post-synthetically modify a-SeNPs by forming either a metal selenide (MSe) shell or nanoparticle using metals that tend to crystallize with Se through a disproportionation-type reaction. The proposed chemical equation is as follows:

$$m\mathrm{Se}_8^0 \rightleftharpoons \mathrm{Se}_n^0$$

$$\mathrm{Se}_n^0 + \mathrm{Se}_n^0 \rightleftharpoons \mathrm{Se}_n^{2+} + \mathrm{Se}_n^{2-}$$

$$\mathrm{Se}_n^{2+} + \mathrm{Se}_n^{2-} + \mathrm{M(OAc)_2} \rightleftharpoons (\mathrm{Se}_n)(\mathrm{OAc})_2 + (\mathrm{Se}_n)\mathrm{M}$$

$$(\mathrm{Se}_n)\mathrm{M} \longrightarrow \mathrm{Se}_{n-1}^0 + \mathrm{MSe}$$

Results and Discussion

As our end goal is biological imaging, we focused these experiments on synthesizing fluorescent ZnSe and CdSe particles that could potentially be used for Correlative Light and Electron Microscopic (CLEM) imaging. We took particular interest in Zn, as it is far less toxic than Cd. Precursor a-SeNPs were synthesized following the borohydride reduction method

described in Appendix A.[127] The growth of a-SeNPs was observed using UV/Vis spectroscopy. We see that about 30 seconds after we add borohydride to selenite, we start to form a-SeNPs (Appendix C Figure C.2).

After SeNP formation (2 – 5 minutes), various metal salts were added to the particle solution. The molar ratio of the metal precursors varied from 1:1, 1:2, 1:4, 1:10, and 1:100 of SeO_3^{2-}:M^{n+}. With most metals, a 1:10 ratio was used except in the cases of Zn and Cd where a 1:100 ratio was used and Ag where only a 1:2 ratio was needed. Experimental details can be found in Appendix C, and the empirical results are shown in Table 4.1.

Table 4.1: Metal disproportionation trials. The ratios of precursors used are specified above and in Appendix C.

Precursor	Observation
a-SeNP + $Pb(OAc)_2$	Black precipitate
a-SeNP + $CoCl_2$	Black precipitate
a-SeNP + $Ce(SO_4)_2$	Pink/red particles
a-SeNP + Na_2WO_4	no change
a-SeNP + $CuCl_2$	Black precipitate w/ metallic blue luster
a-SeNP + Sb-tartrate	Grey precipitate
a-SeNP + $AgNO_3$	Black precipitate
a-SeNP + $Cd(OAc)_2$	Orange fluorescent particles
a-SeNP + $Zn(OAc)_2$	Orange/yellow fluorescent particles
a-SeNP + $KMnO_4$	Brown particles

The transformation of a-SeNPs was also observed initially using UV/Vis spectroscopy. Because ZnSe and CdSe particles will crash out of solution upon conversion, we can continue to monitor absorbance at 375 nm over time (see Appendix C Figure C.2). We allow SeNPs to grow for 5 minutes before adding either $Zn(OAc)_2$ or $Cd(OAc)_2$ in a 100:1 molar ratio of Zn/Cd:Se. In

the case of ZnSe, we notice a change in the absorbance profile begin to occur after approximately 3 minutes, and in the case of CdSe this occurs after approximately 4 minutes (see Appendix C Figure C.2). During this time, we notice a gradual decay of the absorbance of SeNPs, indicating that the particles are crashing out of solution as the reaction proceeds until the majority of the particles have converted to either ZnSe or CdSe. We confirm the agglomeration of ZnSe/CdSe particles using dynamic light scattering (DLS) (see Appendix C Figure C.3). The size of a-SeNPs synthesized began around 40 nm, and upon disproportionation to ZnSe, these particles aggregate into supra-1 μm agglomerates.

We further confirmed that the particles synthesized were selenide nanocrystals rather than oxide particles deposited on top of amorphous selenium particles by doing extensive TEM and SAED analysis. For this study, particles were synthesized in situ by immobilizing a-SeNPs onto negatively glow-discharged C-coated 200 mesh Cu TEM grids. The grid was blotted dry and the particles were washed 2x with ultrapure H2O (18.2 mΩ resistivity). The sample was then transformed to ZnSe or CdSe by drop casting 5 μL of either ice cold 1 M $Zn(OAc)_2$ (aq) or $Cd(OAc)_2$ directly onto the grid, aged for 5 minutes, and then blotted and washed 2x as described above. These results are shown in Figure 4.1.

As-synthesized a-SeNPs are shown in Figure 4.1A along with the fast Fourier transform of the image (FFT), which can be calculated to indicate periodicity in the image collected. When the sample is amorphous, the FFT is featureless without any distinct diffraction spots or rings as is shown in the inset of Figure 4.1A. When the particles are converted to either ZnSe (Figure 4.1B) or CdSe (Figure 4.1C), we observe lattice spacings directly on the image as well as diffraction spots and rings shown by the FFTs in the insets. Figure 4.1 D – F also shows the optical appearance of the particles exposed to UV irradiation (302 nm). Upon inspection we see that the a-SeNP

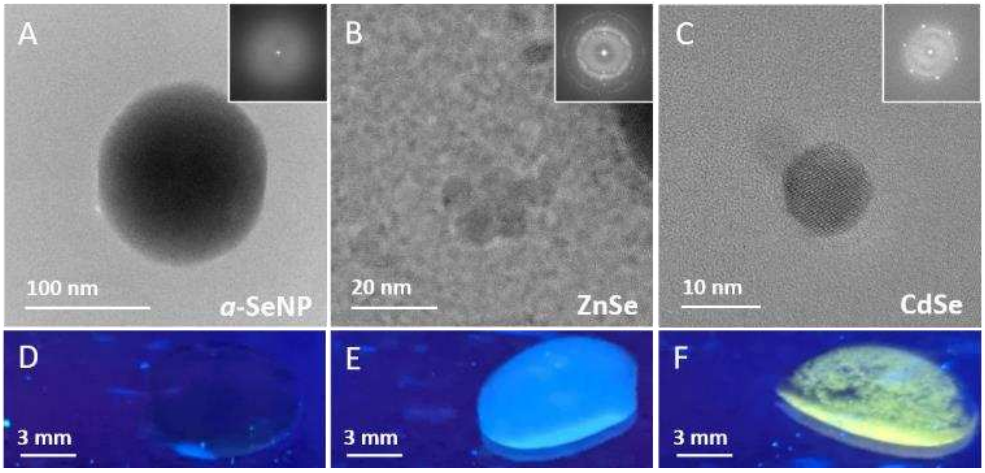

Figure 4.1: TEM data of (A) a-SeNP along with the Fourier transform of the image (inset) showing amorphous structure. (B) In situ transformation of a-SeNPs into ZnSe along with the Fourier transform (inset) showing crystallinity of the particles in the image. (C) In situ transformation of a-SeNPs into CdSe along with the Fourier transform (inset) showing crystallinity of the particles. (D-F) optical fluorescence of drops of a-SeNPs, ZnSe, and CdSe respectively on a UV table with an excitation wavelength of 302 nm.

precursors do not appear fluorescent. Once these particles are converted to either ZnSe (Figure 4.1E) or CdSe (Figure 4.1F), the particles become fluorescent.

The identity of ZnSe and CdSe particles was confirmed by indexing SAED patterns to JCPDS cards obtained from the International Centre for Diffraction Data (ICDD) database. SeNPs disproportionate into zinc blende type ZnSe nanocrystals as was found by indexing SAED images to JCPDS card number 00-005-0522 (Appendix C Figure C.4, Table C.1). The d-spacings of the (111), (220), (311), and (331) lattice planes were matched to different Friedel pairs in the SAED image. Likewise, diffraction data was collected from CdSe particles and indexed to JCPDS card 04-011-9599. Friedel pairs were measured and corresponded to the (100), (002), (101), (110), (103), and (112) lattice planes (Appendix C Figure C.5, Table C.2).

Next, a correlative study was performed by transforming a-SeNPs into ZnSe. The a-SeNPs were synthesized and imaged using SEM while taking note of the locations of particles (Figure 4.2A). High bin (2kx2k) images were collected at low magnification so that large areas of particles could be viewed at once with high-quality images. Next, the particles were transformed to ZnSe

via an *in situ* disproportionation. The grid was then put back into the SEM, where images of the same areas were collected (Figure 4.2B). The grid was then sandwiched between a glass slide and a coverslip and viewed on a light microscope with a laser excitation wavelength of 355 nm at 3 mW and a 405 nm long pass filter. Fluorescence images were collected, and emissions that appeared to correspond to the particles observed in Figure 4.2B are shown in Figure 4.2C. Finally, an overlay was created, allowing us to view where a-SeNPs were before the transformation in red, where ZnSe particles formed after the reaction in white, and the emissions coming from the particles shown in blue in Figure 4.2D.

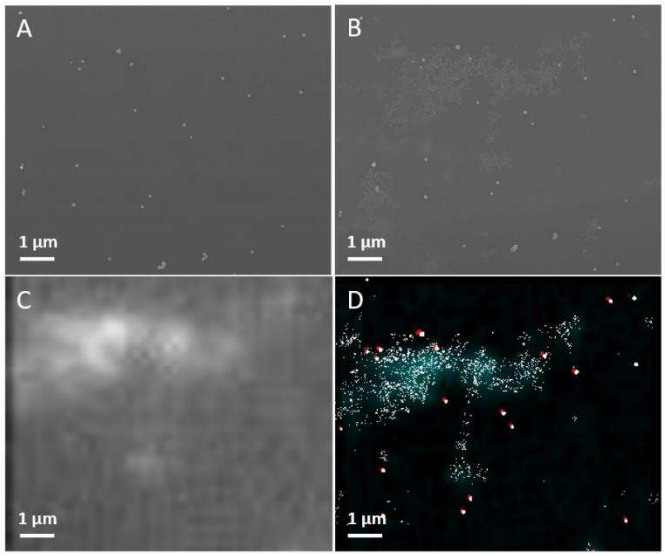

Figure 4.2: demonstrating ability for in situ modification. (A) SeNPs before rxn (B) ZnSe particles after modification (C) Fluorescence image of the particles in B (D) Overlay of images A - C. Red is SeNPs before rxn, white is ZnSe particles after, and blue glow is from fluorescence.

To further confirm that the emissions observed were from ZnSe particles, the sample was again analyzed by TEM and SAED, and the diffraction patterns were correlated to the fluorescence observed. As shown in Figure 4.3, the particles in the TEM image correlate with the fluorescence image shown, and the SAED pattern could be indexed to the characteristic (111) and (311) planes of ZnSe as well as the (222) and (511) planes.

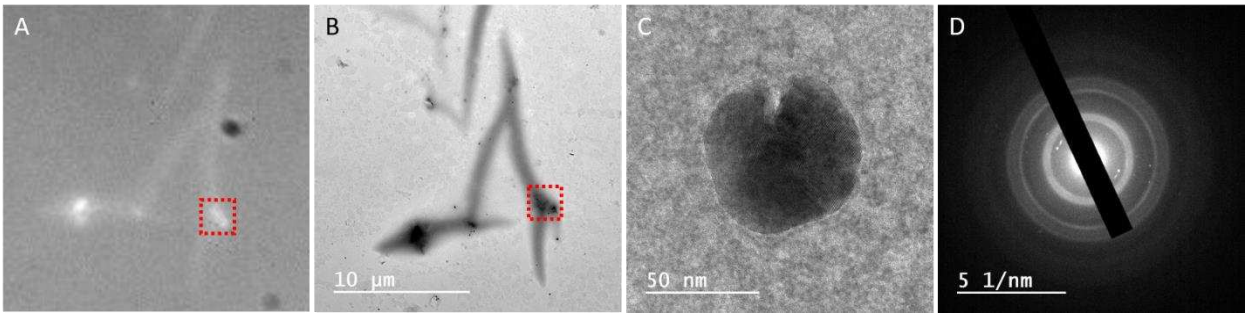

Figure 4.3: Correlative FLM, TEM, and SAED images of ZnSe. (A) Fluorescence image, (B) TEM low magnification view of the same area shown in A. (C) High magnification view of the area boxed in red in B and A. (D) SAED pattern of the image in C. The pattern can be indexed to the 111, 311, and 511 planes of ZnSe.

While extensive characterization has been done on ZnSe and CdSe particles so far, we have also performed the same reaction in solution with a variety of different metal cation precursors as shown in Table 4.1. In observing a color change and precipitation of these particles, we expect that this reaction could be performed with many different metals to synthesize metal selenide nanocrystals. However, based on initial studies it is clear that if a crystal has more than one favorable room temperature structure, the final product will be polycrystalline.

For example, Cu_xSe_y particles were made in situ via the same reaction. However, upon analysis of TEM images and SAED indexing results, it is clear that the product is polycrystalline, since many favorable forms of Cu_xSe_y exist (Figure 4.4B and Appendix C Figure C.6). In contrast, we can produce the single, low temperature phase of Ag_2Se using this type of reaction, since only one phase is favored under ambient conditions (Figure 4.4C and Appendix C Figure C.7). The formation of Ag_2Se under these conditions is not surprising, since nanowires of this composition have been synthesized previously using the disproportionality of Se. Yet still it is possible that other metals may merely form a shell over a-SeNPs like is seen in the example when these particles are reacted with $KMnO_4$ (Figure 4.4D).

It is unclear what promotes the formation of transformed particles versus shelled ones. It is possible that MnO_4 diffusion is much slower than the oxidation of the SeNP surface, causing

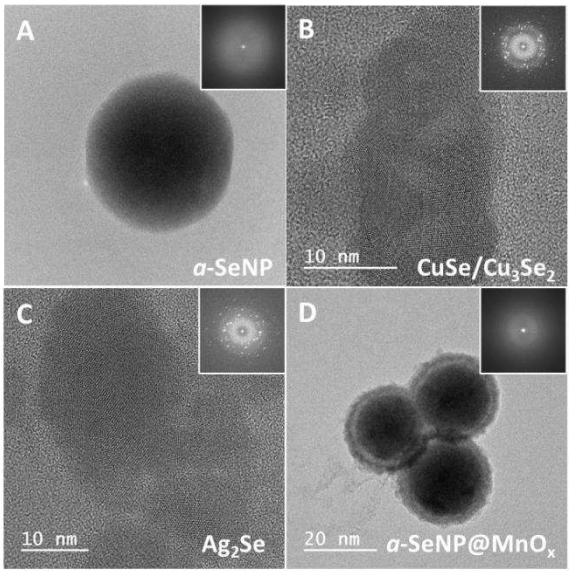

Figure 4.4: (A) Inorganically produced a-SeNPs, (B) Cu_xSe_y particles, (C) Ag_2Se particles, and (D) MnO_x shelled a-SeNPs. The insets of all figures contain the FFT of the respective images.

the a-SeNP core to remain intact while the shell is likely an oxidized MnO_2 layer. Conversely, for other MSe particles, it is possible that diffusion is a faster process than the oxidation of Se^{2-} into MSe. What is also observed in the case of MnO_4 reacted particles is that there is no apparent long-range order. In other words, it is possible that because so many forms of crystalline MnO_2 exist, and because the precursor itself is disordered, no preferred crystallization occurs, and instead the product appears to remain amorphous.[128]

After thorough investigation of inorganically transforming a-SeNPs into ZnSe and CdSe fluorescent particles as well as other MSe species, we hypothesized that we could apply the same method to biogenic a-SeNPs. Using a clonable SeNP (cSeNP), we can produce a-SeNPs that should react similarly to the inorganically synthesized particles shown above. To show this enzyme could be used to synthesize crystalline particles via the same method, we repeated the experiments to create ZnSe and CdSe particles *in situ* with biogenic a-SeNPs. As is shown in Figure 4.5, we can just as well transform these particles into ZnSe and CdSe (Figure 4.5A and 4.5B, respectively).

We directly measured the d-spacings of ZnSe as seen in Figure 4.5C and CdSe in Figure 4.5D to confirm the formation of metal selenide particles.

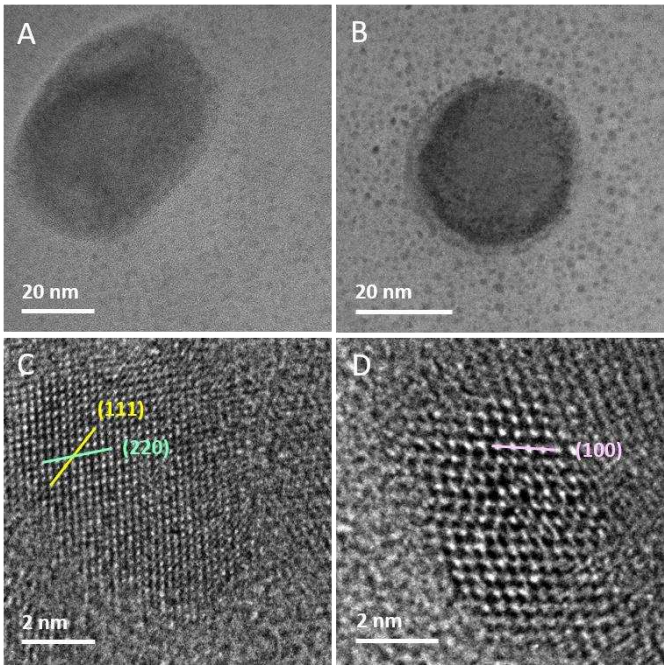

Figure 4.5: HR-TEM images of ZnSe and CdSe particles synthesized using enzymatically produced a-SeNPs. (A) ZnSe particles and (B) CdSe particles viewed at low magnification. High magnification images of (C) ZnSe and (D) CdSe particles showing high resolution images of the lattice planes. A line profile was drawn across the particles, and the planes corresponding to the appropriate d-spacings measured is indicated directly on the images in (C) and (D).

In conclusion, we have demonstrated that using a simple disproportionation type reaction of a-SeNPs with other metals that favorably crystallize with Se, we can produce crystalline MSe particles under biologically friendly conditions. Furthermore, we have demonstrated that the same reaction can be applied to biogenic SeNPs, which is key moving forward. Because we have demonstrated that it is possible to produce ZnSe and CdSe particles with enzymatically produced a-SeNPs, it is plausible that we can use this synthesis for CLEM studies on an *in vivo* system.

Outlook

As we have demonstrated the use of disproportionation with enzymatically produced particles, we envision the enzyme could also be used for patterning other selenide or

semiconducting particles like is shown in Table 4.1. Many biological approaches for patterning nanoparticles have been utilized as alternatives to traditional patterning, which usually involves laser ablation, as viruses, proteins, small peptides conjugated to viruses and/or proteins, and DNA have all been used as scaffolds to build nanodevices as bioinorganic materials.[45,49,51,52,55,56,129,130] While these biosystems have their advantages, their main shortcomings are that either the approach relies on biominerization or the nanoparticles must be synthesized *ex situ*. Therefore, using an enzymatic approach to synthesize and conjugate a nanoparticle would not only provide a biocompatible method to producing nanoparticles, but it would also provide genetic precision for controlled patterning of these biomaterials by allowing us to genetically engineer the enzyme to any structures of interest.

CHAPTER 5: A Breakthrough Study that Applies SeNP Disproportionation Reactions and Clonable Labeling Technology to Localize FtsZ Protofilaments *In Vivo*

Introduction

Biological microscopy is experiencing a "Resolution Revolution," where single molecule techniques that either break the diffraction barrier of light or generate atomic-level protein structures are providing much needed localization and structural data.[6,7,11,12,14,131,132] Regarding super resolution light microscopy, the most promising techniques developed utilize photoswitchable clonable fluorophores, whose fluorescence is activated and deactivated iteratively by two lasers to compute a high resolution image based on intensity decay.[7,131] This class of techniques is capable of up to 30 nm localization resolution, yet the inherent limitation is that only one fluorophore can be analyzed at a time. Furthermore, with only a few laser wavelengths amenable to this technology, not many structures can be labeled at once, hindering our ability to view the surrounding area. This is a major disadvantage for 3D imaging, where key information with respect to the surroundings would be lost.

A better approach would be to use electron tomography that can provide routine nanometer-level resolution on the low end to both the protein of interest and the surrounding areas, allowing for the generation of 3D models.[133] What has hindered the routine use of electron tomography for protein localization is the lack of commercially available EM contrast agents, as was described in Chapter 1. While we have shown in Chapter 3 our ability to form SeNPs *in vivo*, we have yet to determine whether we can protect these particles during sample preparation for standard EM analysis.

One of the most important aspects of biological electron microscopy is cellular preservation. When preparing samples for electron beam bombardment, it is vital to fix the

specimen using either chemical fixation or vitrification, exemplified in Figure 5.1 that was reproduced with permission from BioTechniques and Mechdonald and Auer (2006).[25] Clearly, the structures within the sample prepared using chemical fixation in panel A have undergone significant shifts, resulting in fixation artifacts. For example, we see that the golgi apparatus (g) in panel B, which was prepared via vitrification, extends much farther than what is noted in panel A. Additionally, in panel B there are clearly objects found in the extracellular space that are completely absent from the sample in panel A. Overall, for quality structural EM studies, vitrification is the ideal preservation approach.

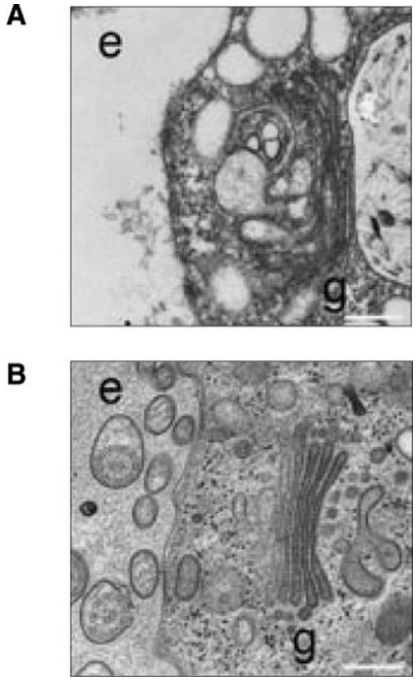

Figure 5.1: Example image from the marine sponge Oscarella carmela prepared using (A) chemical fixation and (B) vitrification. Labeled are the extracellular space (e) and the golgi apparatus (g). Reproduced with permission from BioTechniques and McDonald and Auer (2006).

Several techniques have been developed to prepare samples via vitrification, including plunge freezing, freeze fracturing, and high pressure freezing.[20,25,134,135] Plunge freezing can be done with relatively cheap equipment, but is limited to very thin samples (ca. 3 – 5 μm), as thicker

samples have a greater tendency to form ice crystals.[25] Freeze fracturing and high pressure freezing require specialized equipment. Likewise, with freeze fracturing, the sample must be very thin, but it differs in that a replica made of vacuum deposited Pt-C is imaged, not the biological material itself.[135] Its main advantage is the ability to preserve membrane associated proteins and structures, which preferentially break due to the weak interactions of the hydrophobic tail groups of the lipid bilayer.

High pressure freezing is arguably the most versatile method, as much thicker samples (ca. 200 μm) can be vitrified, such as tissues. Additionally, because the samples are slowly brought back to room temperature over time, handling is much simpler. Once high pressure frozen samples are brought back to room temperature through freeze substitution in anhydrous fixative, they can be processed for resin infiltration and curing using routine embedment protocols.

Current clonable EM labels (APEX and miniSOG) are not compatible with these preservation methods. As the contrast agents must be added post-fixatively, it is not possible to use these labels with advanced preservation methods.[3,33] To this end, our goal was to illustrate that clonable inorganic nanoparticles could be processed alongside biological samples using these preservation and embedment methods. As was shown in Chapter 3, clonable SeNPs are not amenable to the dehydration and embedment protocols. In Chapter 4, we demonstrated our ability to post-synthetically modify SeNPs *ex situ*. Finally, in Chapter 5, we explore the potential of performing these disproportionation-type reactions both *in vivo* and as a post-fixation step to ultimately produce particles that can withstand the processing involved in specimen preparation.

Results and Discussion

Using $KMnO_4$ to Shell Biogenic SeNPs and Enhance Cellular Contrast In Vivo

From our previous study probing the transformative properties of amorphous SeNPs synthesized with inorganic and enzymatic methods, we were encouraged by the potential to apply the technique to an *in vivo* system. Initially, we chose to use $KMnO_4$ to both shell the SeNPs to protect them from degradation and to stain the cell membrane to imbue higher contrast of any surrounding structures.[136] This study was conducted using the "Goldilocks" method described in Chapter 3 and Appendices B and D. After fixation, 0.6% buffered $KMnO_4$ was added to the sample for 25 minutes followed by 5 washes in ice cold buffer. Dehydration and embedment followed to produce sections that were imaged as shown in Figure 5.2. In the top row are images of the control, and in the bottom row are images of the sample. Both samples show a higher level of contrast than in previous images of unstained cells. In the Se-rich sample, there seems to be more contrast at constriction points than in the control. We further analyzed the sample using EDS. In Figure 5.3,

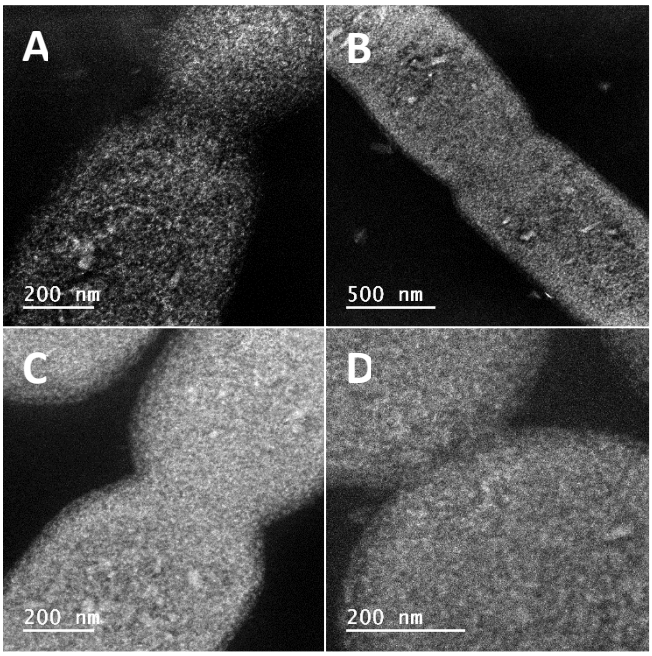

Figure 5.2: Control and SeNP samples reacted with $KMnO_4$. (A&B) Images of the control soaked with $KMnO_4$ and (B&) images of the SeNP containing samples soaked with $KMnO_4$.

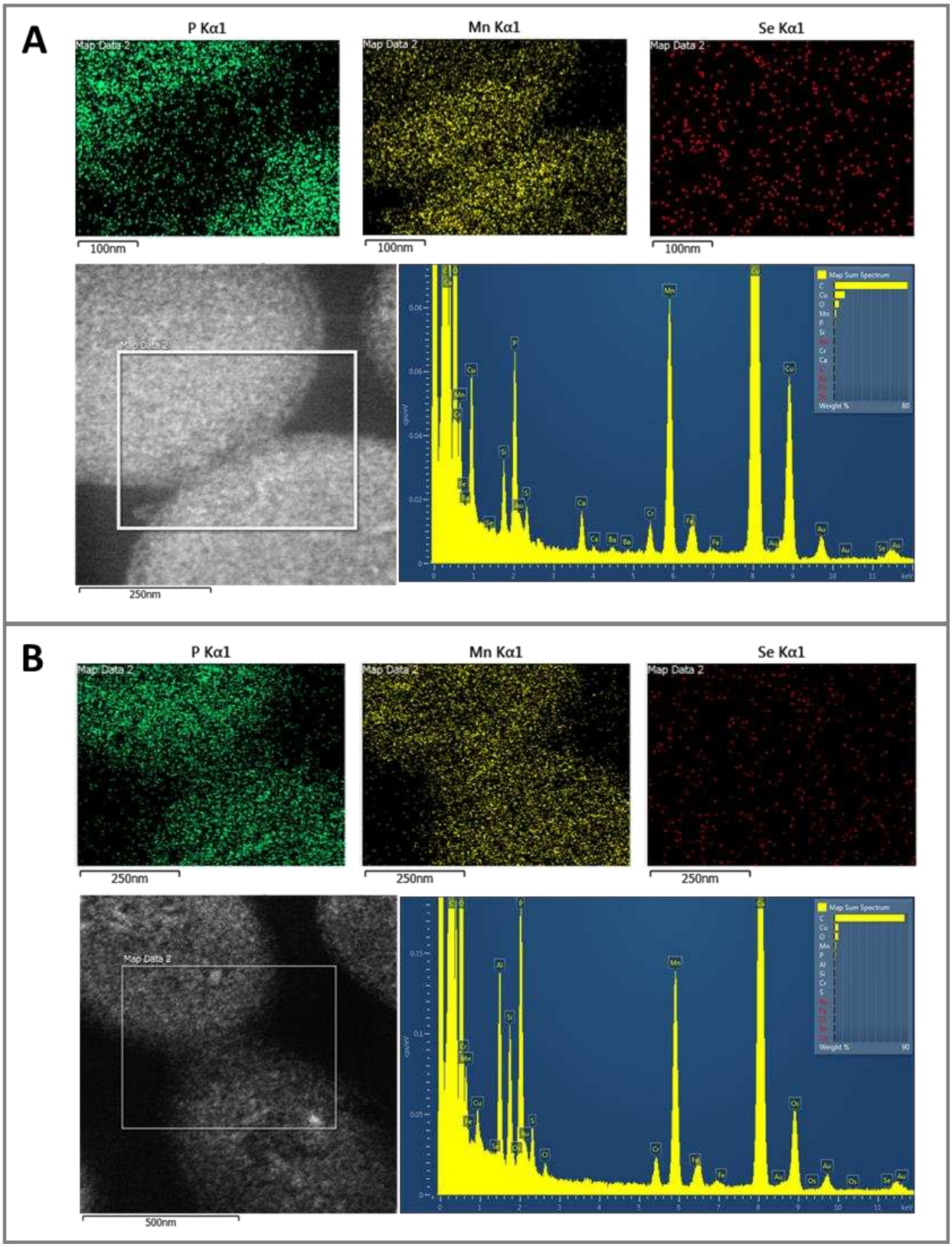

Figure 5.3: Elemental analysis of (A) the SeNP sample and (B) the control sample, both soaked with $KMnO_4$.

it is apparent that both the control and Se-rich sample contain Mn shown by the elemental map

and in the X-ray spectrum. What is quite interesting is that in the Se-rich sample, there is a clear localized concentration of Mn directly at a division point, indicated by the morphology of the cell and by the lack of P, where we would expect to see SeNPs. In stark contrast, this Mn localization is not observed in the control at a similar junction, where we do not expect there to be SeNPs. These results are suggestive of Mn localizing over small SeNPs, especially since there is a clear lack of P, the main group that Mn is used to stain.[136]

What is also apparent is the lack of Se signal in both the X-ray spectrum and the elemental map. In the Se-rich sample, there may be a trace amount of Se shown by the blip just above baseline from the K-line and by the lightly enhanced red color of the elemental map compared with the control. However, what is most desirable is the formation of punctate particles, which is unclear in these samples.

In an attempt to capture large, discrete particles, samples were prepared using a longer induction period as previously described, using 1 mM IPTG and 1 mM SeO_3^{2-} (1 μM for the control) over 3 hours (see Appendix D). The results of this experiment are shown in Appendix D Figure D.1. Although the samples containing SeNPs appear to be "spottier," the particles do not appear punctate as expected. Furthermore, because $KMnO_4$ tends to precipitate and create 2 – 15 nm schmears as seen in the control images in Appendix D Figure D.1, the stain itself can cause ambiguity in particle assignments.[27] Furthermore, $KMnO_4$ is very toxic to bacteria and cannot be used for *in vivo* nanoparticle transformation.[137] Even still, this study proved promising and inspired further exploration of SeNP disproportionation using other metals.

Disproportionating Biogenic SeNPs into ZnSeNPs as a Post-Fixation Step

Encouraged by the $KMnO_4$ studies, a ZnSe disproportionation experiment was attempted using the cSeNP construct alone. This was chosen to ensure large SeNP formation, which had

previously shown to produce ~80 nm particles as seen in the inset of Figure 5.4A. The sample was made by inducing with 1 mM IPTG and 1 mM SeO_3^{2-} for 3 hours followed by fixation. After fixation, the sample was soaked overnight at 4 °C in a 50 mM $Zn(OAc)_2$ solution supplemented with 100 mM acetate (detailed methods are available in Appendix D). From Figure 5.4, there is an apparent morphological difference between the unmodified SeNPs (shown in the inset of Figure 5.4A) and the transformed particles, which mimics the inorganic disproportionation syntheses described in Chapter 4. Furthermore, shown in the inset of Figure 5.4B and 5.4C, we observe crystalline planes that are not observed in the amorphous precursor particles.

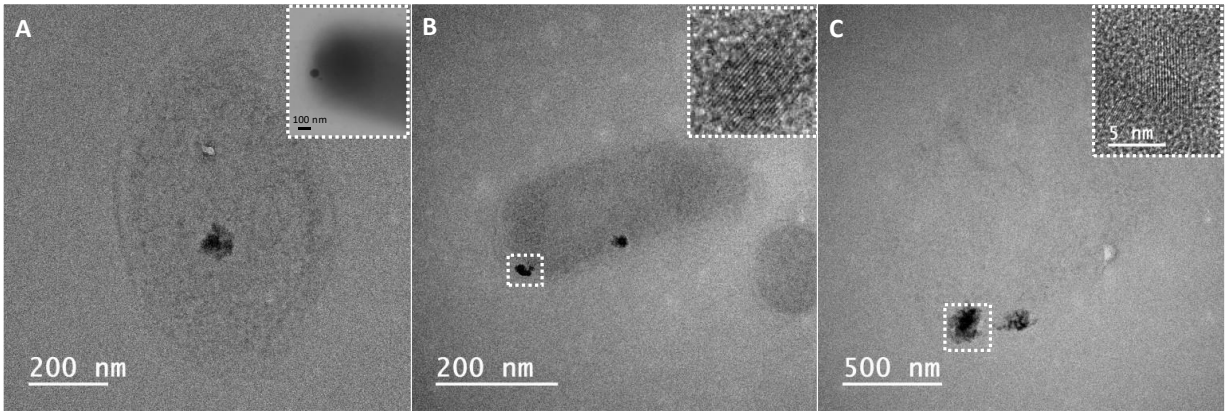

Figure 5.4: Example images of cells containing SeNPs that have undergone disproportionation with Zn. The inset of (A) is an example image of the SeNP-only sample. The insets of (B) and (C) show the lattice planes of two particles within the cells in the regions boxed in white.

These results are suggestive of a successful attempt to form ZnSe particles *in vivo* as a post-fixation step. However, there are very few particles that appear crystalline. This could indicate an incomplete disproportionation, which may be due to biomolecules preventing the diffusion of Zn^{2+} into SeNPs. It is also possible that the thickness of the section (100 nm) prevents observation of the crystallinity of the particles due to their dispersion in an amorphous material and significant scattering of electrons therein.

To improve the quality of the particles produced, we attempted a simultaneous disproportionation/fixation step by using Zn-Formalin to preserve cells. The sample containing the

chimeric cSeNP-FtsZ DNA was prepared by incubating cells in 2 mM SeO_3^{2-} and 1 mM IPTG for 2 hours followed by fixation for 1 hour on ice in 3% Zn-Formalin diluted into 0.1 M acetate. The results of this experiment are shown in Appendix D Figure D.2. The cells contained both large intracellular particles (~50 nm), smaller particles (~10 nm), and wavelike structures appearing to contain ultrasmall particles (~2 nm). The wave structures had not been seen previously in samples and were solely located along the membrane. If these structures are FtsZ filaments, it is possible that the rapid fixation of small molecule formaldehyde causes significant movement in the structures. As we had previously used a glutaraldehyde only fixation step, we had not noticed particles in this type of arrangement. Furthermore, because Zn^{2+} is providing a light metal stain to biomolecules, it may explain why these structures are highlighted. However, it is unclear why these structures are stained in this sample and not in other samples that had been soaked with Zn^{2+}.

While some particles are obvious in the sample, we do not see an abundance of particles like we expect. Again, it may be due to the incomplete reaction of Zn^{2+} with SeNPs *in vivo* since biomolecules can chelate Zn^{2+} and prevent these ions from reaching the particles. As such, the unreacted SeNPs could have been dissolved during sample processing, causing this apparent particle sparsity.

Disproportionating Biogenic SeNPs into CdSeNPs as a Post-Fixation Step

While Zn^{2+} is a more biologically friendly metal to use than Cd^{2+}, the particles do not appear as fluorescent as those made with Cd^{2+}. Thus, we attempted to transform particles into CdSe *in vivo* as a post-fixation step. We used a sample that had been induced with 100 µM IPTG for 1 hour followed by a 3 hour incubation in 1 mM SeO_3^{2-}. After fixation the sample was allowed to soak overnight in 50 mM $Cd(OAc)_2$ solution supplemented with 100 mM acetate at 4 °C followed by dehydration and embedment. A detailed procedure can be found in Appendix D. The results of

the experiment are shown in Figure 5.5. Similar to the ZnSe sample, the morphology of the CdSe particles matches those of the disproportionation type reaction, having the appearance of random growth out of a central point. Upon elemental analysis of the sample, it is shown that the sample is Cd-rich, which is likely due to extra Cd^{2+} salts depositing onto the newly formed CdSe particles. Additionally, the CdSe particles appear to be aligning into filamentous structures within the cells, which suggests that the CdSe has reacted with SeNPs that have labeled FtsZ.

Also similar to the Zn^{2+}-reacted sample was that the particles did not appear crystalline. From EDS data, it is possible that extra Cd^{2+} salts deposited onto the particles, preventing this observation. This could also be true for the Zn samples; however, we cannot confirm this since EDS was not performed due to the presence of Zn in the pole piece of the instrument, which would

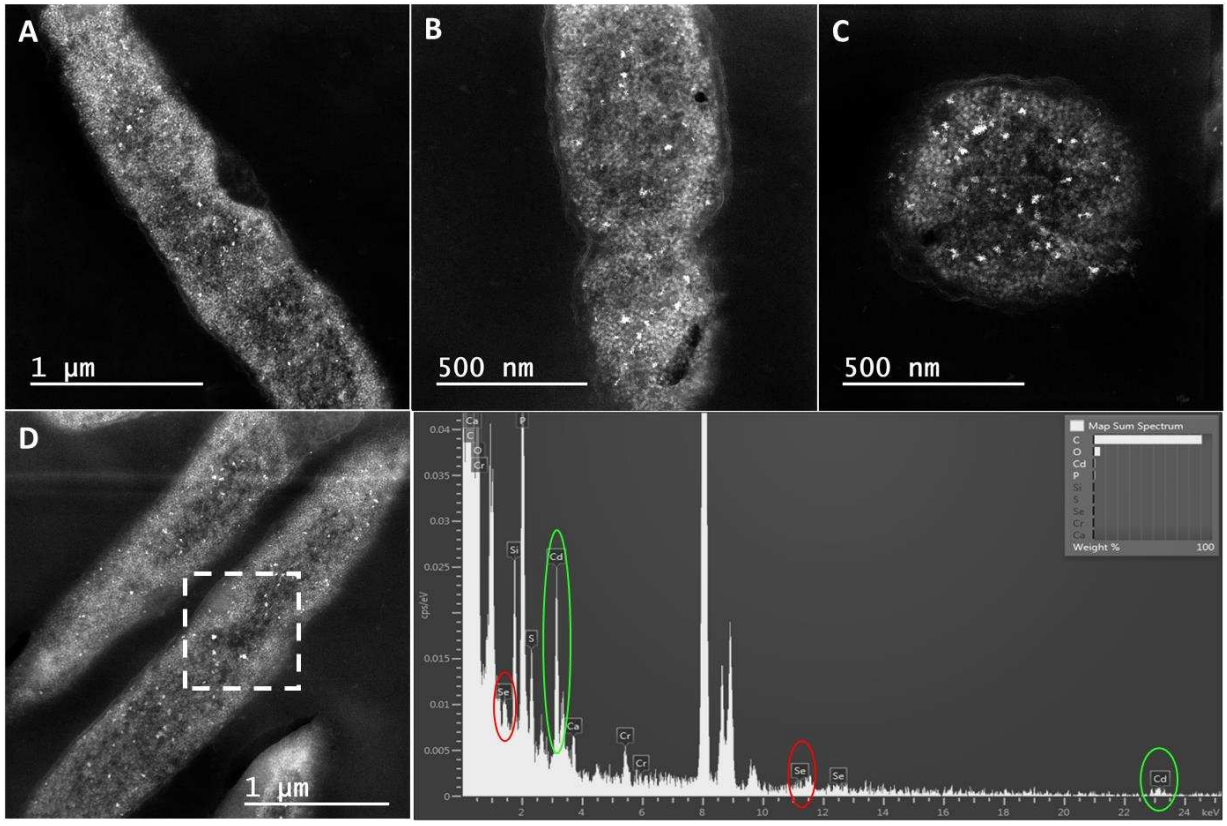

Figure 5.5: (A-D) Examples of SeNP containing samples that have been disporpotionated with Cd. Elemental analysis was taken from the region boxed in white in (D) and the spectrum is shown to the bottomr right. Circled in green are the Cd peaks and in red are the Se peaks.

result in an apparently high amount of Zn in the sample. It is also possible that lattice planes are not observed because the thickness of the section (100 nm) is preventing their observation. Finally, it could be that the reaction was not successful in completely transforming the particles, but it is apparent that Cd^{2+} protected the SeNPs from dissolution during processing. Unsure whether or not the disproportionation reaction was going to completion, we turned to metals that react more readily with the SeNP.

Disproportionating Biogenic SeNPs into Ag_2SeNPs as a Post-Fixation Step

Even though Ag^+ can be tricky to work with in a biological system, our studies from Chapter 4 as well as previous studies reveal that Ag^+ readily reacts with SeNPs at stoichiometric equivalents.[122] Thus, we hypothesized that reactions of SeNPs with Ag^+ would readily go to completion even in a biological matrix. Therefore, we should be able to observe both transformed and crystalline particles in these samples.

For this protocol, the goal was to enzymatically produce as many particles as possible. Therefore, the sample was prepared by performing a low level overnight induction using 10 μM IPTG and 1 μM SeO_3^{2-} to have a low level of chimera present for the ramp up, which was done following dilution by inducing with 100 μM IPTG and 2 mM SeO_3^{2-} for 3 hours while cells were in log phase (O.D. ca. 0.4). After fixation, the sample was soaked in 1 mM $AgNO_3$ supplemented with 100 mM acetate overnight at 4 °C. A detailed procedure can be found in Appendix D. The control was treated identically except the [SeO_3^{2-}] was kept at 1 μM. The results of this are shown in Figure 5.6.

It is apparent from the data that there are particles in both the control (panels A and B) and SeNP (panels C – E) samples. We believe, due to the extended expression of the chimera along with requiring a small supplementation of 1 μM SeO_3^{2-}, it is possible that there are ultrasmall

SeNPs or pools of zerovalent Se monomers present within the control. This in conjunction with the high reactivity of Ag^+ with Se could account for particles present within the control, especially since those in the range of 5 – 20 nm appear where we would expect to see FtsZ. Another source of AgNP formation could be due to photo reactions. Care was not taken to protect the sample from light, and it is possible for light-induced reduction of Ag^+ in the presence of biomolecules, such as cSeNP, to account for a portion of the particles seen in the control.[138]

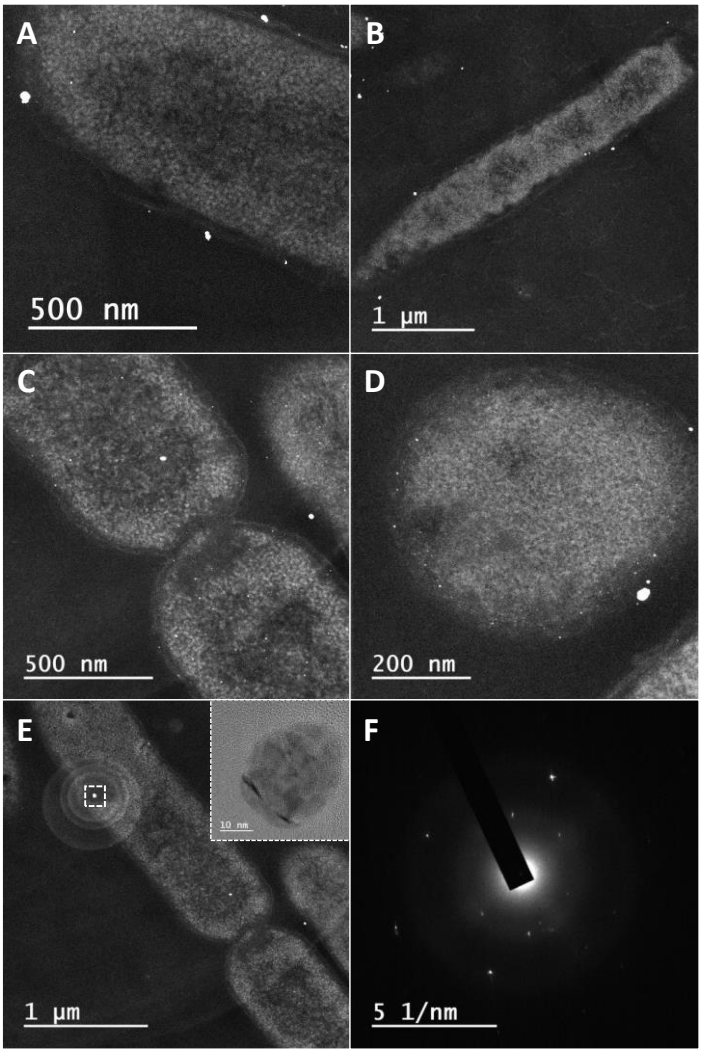

Figure 5.6: (A&B) Examples of the control that was soaked with Ag^+ and (C-E) of the SeNP containing sample that was soaked with Ag^+. The inset of (E) shows that the particles boxed in white are crystalline, and (F) is a SAED image captured from the particles in the sample.

Despite the possibility of background particle formation, the distribution and pellucidness of the particles in this sample was the most promising to date. Shown in Figure 5.6C – E are a division point and a cross-section perspective, respectively. In panel C, we observe particles aligning the membrane and across the cleavage furrow as expected. Similarly, in Panel D we see the particles concentrated about the inner membrane as they should be when labeling FtsZ. Highlighted in Figure 5.6E is a larger particle found within the sample, and the inset reveals that the particle is crystalline. Finally, in Figure 5.6F is a SAED image of the particles within the sample, where the characteristic [122] plane of Ag_2Se was compared with the data obtained in Chapter 4 and confirmed as such. Additionally, elemental data was collected to confirm traces of Se within particles, but they are certainly Ag rich (see Appendix D Figure 5.3).

To reduce the amount of background particle formation, another experiment was conducted omitting SeO_3^{2-} entirely from the control and keeping the samples in the dark when incubated with $AgNO_3$. Details of the procedure can be found in Appendix D. The results are shown in Figure 5.7. Panels A and B are of the control sample, where we see much less background particle formation, and panels C and D are of the SeNP containing sample, where we are indeed seeing small discrete particles forming along membranes as expected. In the control, it is clear that particles are still forming. It is possible that either 1) Ag(I) is highly reactive to the active site of cSeNP, 2) that even without SeO_3^{2-} supplementation, cSeNP can efficiently reduce Se species naturally present within cells, or 3) Ag(I) is reacting with endogenous glutathione.[139,140] Because the samples are fixed and washed several times before the introduction of Ag(I) into the sample, it is unlikely that enough glutathione remains within the cell to promote so much particle formation. The most plausible explanation is that Ag(I) is easily reduced by the active site of cSeNP, since these “background” particles appear in the cell where we expect FtsZ to localize.

This can be tested by repeating this experiment with cells that have not been induced and is currently ongoing.

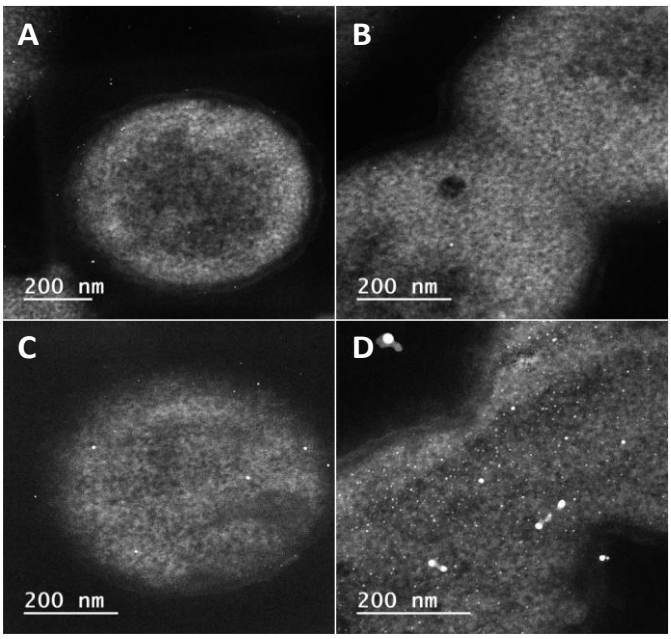

Figure 5.7: (A&B) The control sample soaked with Ag^{+} and (C&D) the SeNP containing sample soaked with Ag^{+}.

Disproportionating Biogenic SeNPs into CuSeNPs as a Post-Fixation Step[c]

We moved forward using Cu^{2+}, a metal that is much less toxic to prokaryotes and can also react readily with SeNPs. The first sample made was prepared identically to the Ag_2Se sample towards creating as many intracellular SeNPs as possible using the low level induction followed by a ramp up. The results of this experiment, using Cu instead of Ag, are shown in Figure 5.8. The control sample is given in panels A and B, where we see a bit of salt precipitate along the membrane. However, there are no indications of background particle formation as was seen in the Ag_2Se controls. Furthermore, small CuSe particles running along the inner membrane are easily seen in Figure 5.8C, 5.8D, and 5.8E. To confirm that these particles were CuSe, EDS was done,

[c] The stoichiometry of the Cu_xSe_y particles *in vivo* is unknown. For clarity, we simply denote them as CuSe throughout the remainder of the text.

as is shown in Figure 5.8F and in Appendix D Figure D.4 and D.5. Coupled together, these results indicate that Cu is selectively reacting with the SeNPs and not with intracellular biomass.

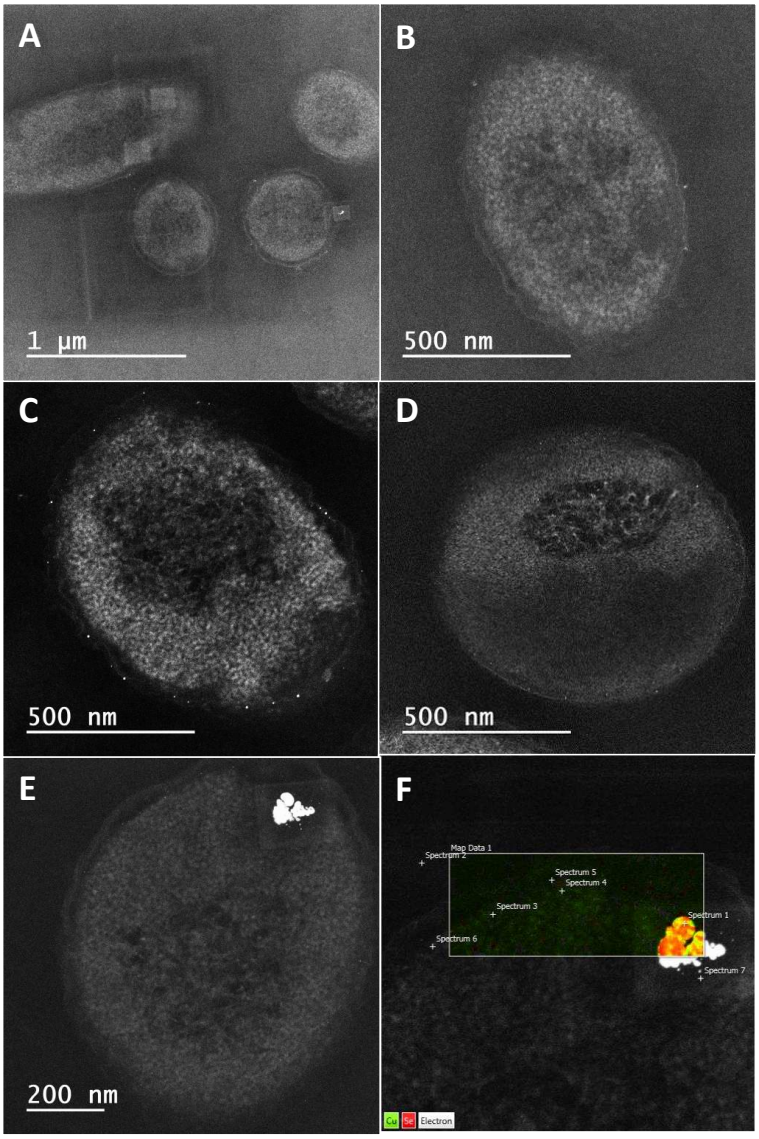

Figure 5.8: Post-fixation formation of CuSe particles. (A&B) Controls (C,D,&E) CuSe Sample (F) EDS map of image E, showing large CuSe particles as well as much smaller ones.

Disproportionating Biogenic SeNPs into CuSeNPs In Vivo

To further gauge the potential of using CuSe particles for clonable labeling, another trial of experiments was done to test whether the disproportionation could be done *in vivo*. Details of the experiment can be found in Appendix D. Briefly, following SeNP formation, usually 30 – 60 minutes after initial incubation with selenite, $Cu(OAc)_2$ was added to the culture for 1 hour at a

final concentration of 1 mM, 500 µM, 250 µM, and 100 µM followed by fixation. From previous toxicity studies, we know that *E. coli* are viable in up to 2 mM Cu^{2+} supplementation in LB medium. However, what has not been done is a dual metal stress experiment with both SeO_3^{2-} and Cu^{2+} added to the medium. It is known that formation of SeNPs will greatly reduce the toxicity of selenite, but it is not known if the same effect will occur upon disproportionation of SeNPs into CuSeNPs. Thus, the results from the Cu concentration screen are shown in Figure 5.9. In panel A, the control was made by only adding 0.5 mM $Cu(OAc)_2$ to the culture. As expected, *E. coli* appear normal and healthy. Panel B shows the results from adding 1 mM $Cu(OAc)_2$ to the culture that was first incubated with 2 mM SeO_3^{2-}, where it appears that many cells have died and are busted. There are some that appeared viable, and even contain indications of particles aligning the membrane. In panel C, the SeNP sample in which 0.5 mM $Cu(OAc)_2$ was added to the culture, the cells appear similar to Figure 5.9B, where many are busted and shriveled due to the toxicity of Cu^{2+} and Se^{4+}. Again, we are seeing a few viable cells that contain particles. Once we drop the concentration down to 0.25 mM, the cells begin to appear much more viable, and small particles that appear to align filamentous structures as well as pinch points become visible as seen in Figure 5.9D. This is even more apparent in the 0.1 mM sample, where cells now appear normal and particles are again aligning filamentous structures and midpoints as shown in Figure 5.9E. From these trials, it does seem that we are able to form CuSe particles *in vivo* using the disproportionation of clonable SeNPs. Our ability to form these particles *in vivo* opens the possibility of using this label for vitrification protocols as well as the standard ones against which these samples were screened.

It appears as though Ag- and Cu-containing samples provide particles that appear more spherical rather than the particles formed in the Zn and Cd trials, which had a splotchy morphology.

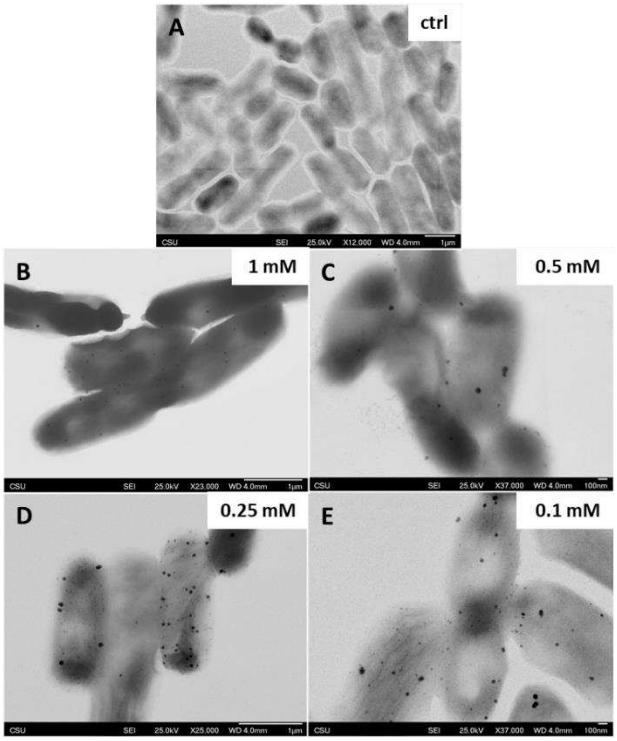

Figure 5.9: Cu concentration screen. (A) control sample incubated with 0.5 mM Cu(II), (B) SeNP sample incubated with 1 mM Cu(II), (C) SeNP containing sample incubated with 0.5 mM Cu(II), (D) SeNP sample incubated with 0.25 mM Cu(II), and (E) SeNP sample incubated with 0.1 mM Cu(II).

Additionally, there is very minimal metal precipitation, which is quite prominent in the samples containing $KMnO_4$. All in all, both the Cu and Ag samples made above were promising candidates for tomography. In doing this study, we would be able to confirm that particles are aligning the membrane in an ordered fashion that resembles FtsZ filamentation. Furthermore, we would be able to better resolve any ultrasmall particles that are being formed.

Tomograms and Models of the CuSe Sample Prepared Using a Post-Fixation Disproportionation

Tomogram acquisition would allow us to better resolve the intracellular particles and provide context of where the particles are with respect to the membrane. From previous studies, it appears that FtsZ localizes approximately 16 nm from the inner membrane, which in turn is about 30 – 40 nm from the outer membrane. Thus, we should be able to infer from distance measurements

that, if particles are within ca. 45 nm from the outer membrane, then they are likely associated with a protofilament. Because these samples were prepared via chemical fixation, we know that the preservation was not optimal. In this regard, even though the membrane is poorly preserved, so long as particles appear to be stable (no major aggregation events or dissolution noticed) and are within a reasonable distance from the membrane, we could infer that the particles are likely associated with filaments.

Tomograms were reconstructed from a tilt series of the CuSe sample shown in Figure 5.8 collected by collaborators from CU Boulder. We chose the CuSe sample because there were no background particles in our controls. For collection parameters, see Appendix D. After reconstruction, the tomogram was segmented using the IMOD software to construct a model of particles aligning protofilaments. The tomogram and the model are shown in Figure 5.10.[d] For clarity, only the outer membrane and the particles were modeled, which is represented in panel C. Particles were picked based on their morphology and contrast compared with the background.

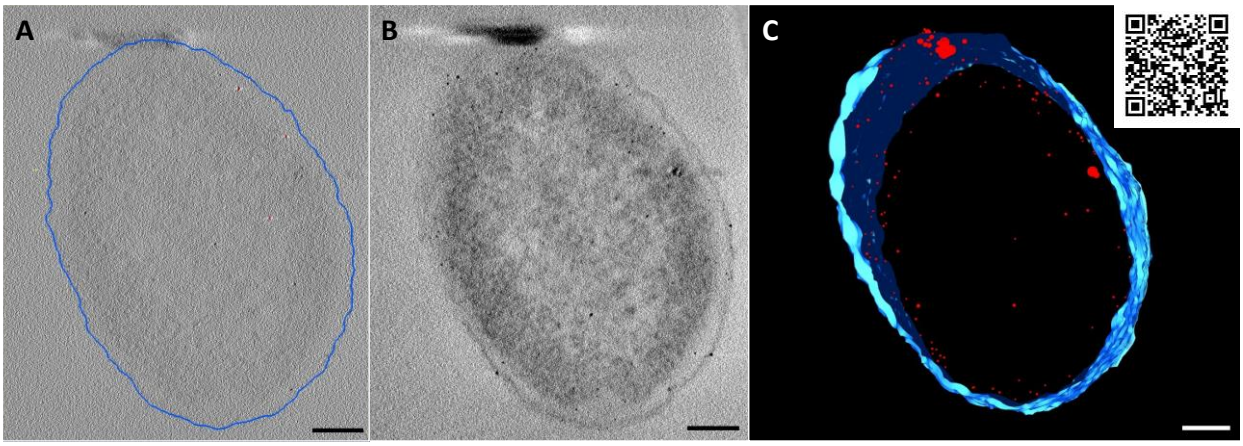

Figure 5.10: Tomogram reconstruction of the CuSe-FtsZ construct. (A) Single slice from the zero-degree tilt perspective. (B) A representation of 100 averaged slices. (C) Model view where the outer membrane is colored blue and the particles are colored red. The QR code in the inset is a link to the model movie file. Scale bars are 100 nm.

[d] To use the QR code, increase the document zoom to 200%, open your smart phone camera, and hold it over the code. Access to the shared drive has been granted to all with a colostate account. Please make sure your phone is linked to a CSU account beforehand. For readers outside of CSU, please contact Dr. Chris Ackerson for access to this content.

Examples of particles picked are shown in Appendix D Figure D.6, where high density areas were marked. From the image and model, it is clear that particles are closely bound to the membrane. We compared the CuSe sample to a control sample, and this is shown in Appendix D Figure D.7. Viewing the control, we do not see distinctive particles as is apparent in Figure 5.10B.

To further confirm that the particles were aligning FtsZ, the distance of each particle was measured perpendicular to the flow of the membrane, and a frequency plot was created as shown in Figure 5.11. Most of the intracellular particles (94%) are within 44 nm of the outer membrane. Of those, 37% are within 16 nm of the outer membrane, which can be attributed to poor preservation. During chemical fixation and dehydration, ca. 90% of unfixed biomolecules are extracted from the cell, causing structures to shift and create fixation artifacts. With this in mind, we are confident that the particles within 16 nm are associated with FtsZ protofilaments that have

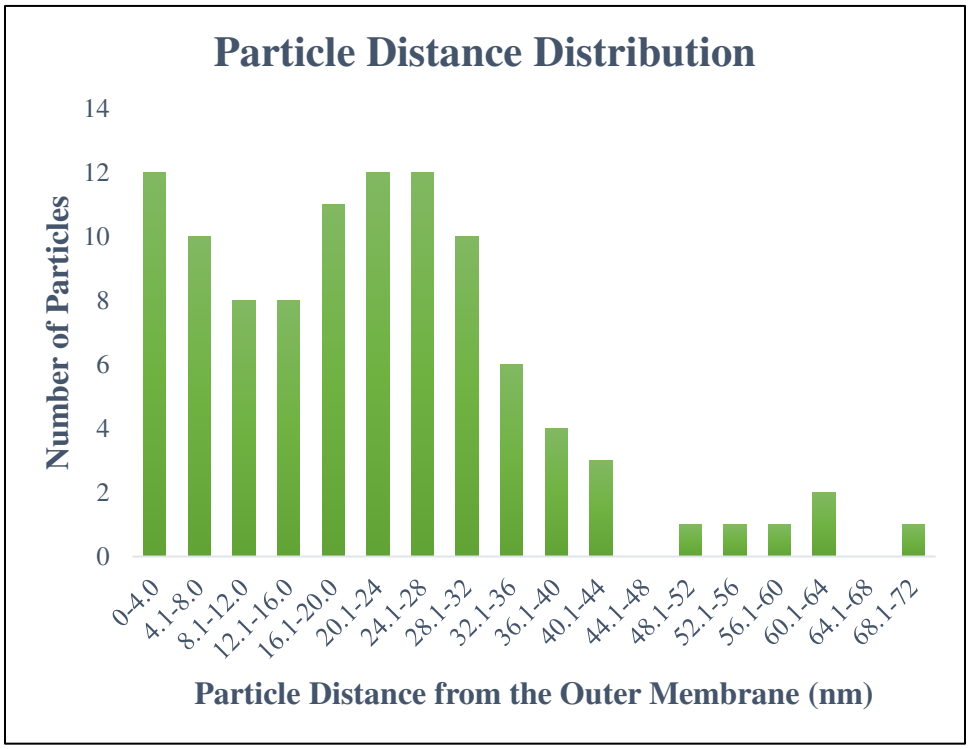

Figure 5.11: Particle distance frequency distribution of CuSeF Cell5. 57% of particles are 16 – 44 nm from the membrane, 37% are 0 – 16 nm from the outer membrane, and 6% are beyond 44 nm.

moved during processing. The majority of the particles, 57%, are found 16 – 44 nm from the outer membrane, which is likely where protofilaments would be found.

To confirm that the particles are aligning FtsZ, it was important to analyze a division point to search for filamentation around a constricting membrane, which would be suggestive of Z ring formation. These results are shown in Figure 5.12. Similar to the tomogram shown above, we notice particles closely associated with the membrane of the cell. Judging by the morphology of the cleavage furrow, this cell is in a very late stage of division. The septum is approximately 150 nm wide and 20 nm long. As such, it is possible that FtsZ has already migrated towards the interior of the cell, using treadmilling with other division proteins to pinch the two halves into separate daughter cells.[141] Thus, at this point in the division we do not see the notable structure of the Z-ring. However, it is clear that these particles are localized around the septum as is shown in Figure 5.12C-F.

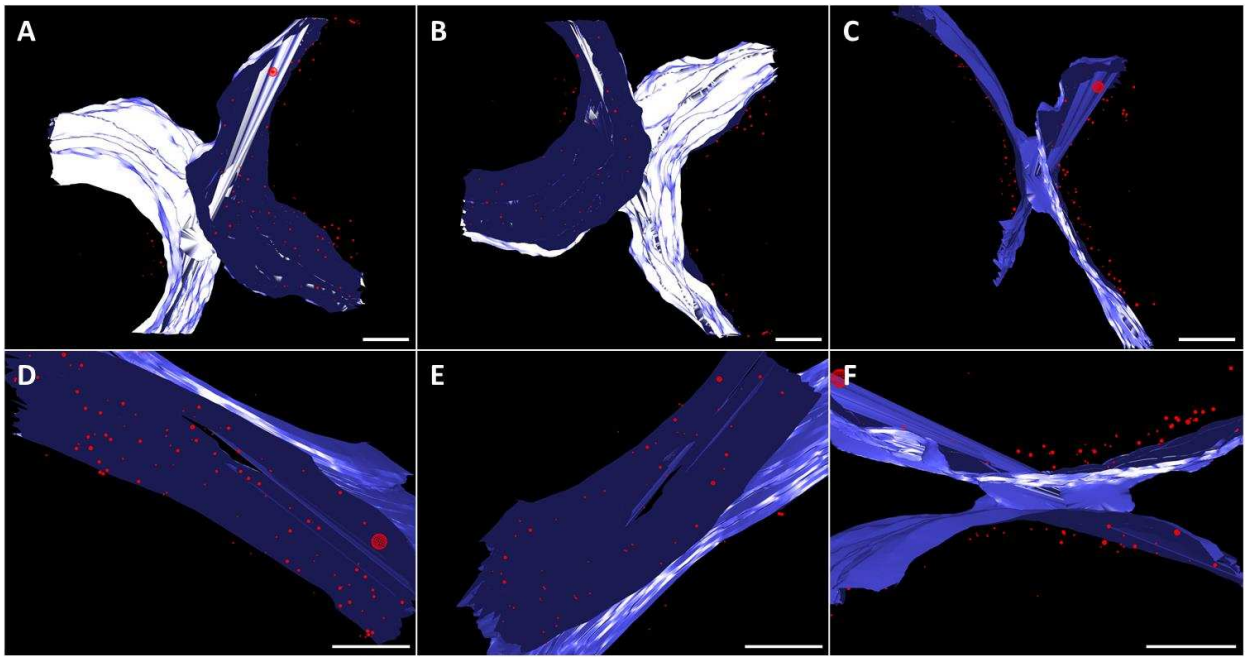

Figure 5.12: Model views of the dividing cell from the (A) top, (B) bottom, (C) side, (D) right (E) left, and (F) another perspective of the side. The particles are red, and the membrane is blue. Scale bars are 100 nm.

Impressively, we notice that at a constrictive point of the membrane where a clear force is being exerted on the membrane and causing it to distort inward (see Figure 5.12A and B at the lighter portion of the inner membrane), there are particles running along in a remarkably ordered fashion, which is most apparent in Figure 5.12D. In this view, we notice the particles running parallel to the distorted membrane. These particles are likely aligning the membrane in this way because of FtsZ migrating inwards to clinch the cell apart. To further confirm that our interpretation is accurate, we viewed the other side of the pinch point, shown in Figure 5.12E, where we observe the same ordered array of particle migrating along the membrane at the constriction point within the cell. To better view these particles, we compare the model with and without the membrane shown. As seen in Figure 5.13, the particles neatly align along the contour of the membrane. In Figure 5.13A and 5.13B, we notice at the division point that the particles slightly jut out towards the middle, indicating that these particles are likely aligning the remnants

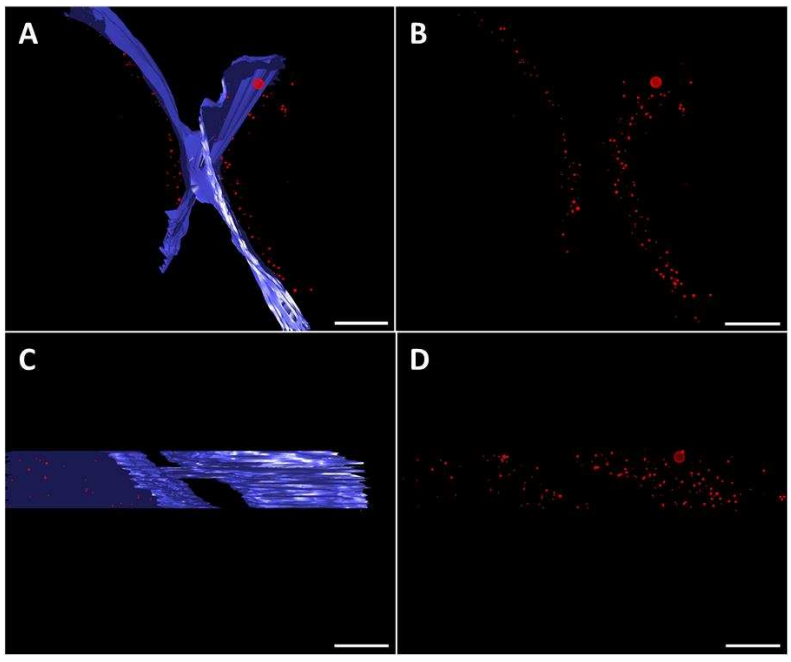

Figure 5.13: Other model views of the dividing cell shown in Figure 5.12. (A&B) Are views from above the pinch point with and without the membrane shown. (C&D) Are side views with and without the membrane shown. Particles are shown in red, and the membrane is shown in blue. Scale bars are 100 nm.

of a Z-ring. Furthermore, as is seen in Figure 5.13C and 5.13D, at the midpoint it is clear that the particles are curving with the flow of the membrane. Because these particles orient in such an ordered array, we are confident that the distribution within the cells is not due to background labeling and is marking protofilaments. If there were an abundance of background particles within the cell, these would likely aggregate or be found in the center of the cell as had been observed in our original study of GRLMR (Ni *et al.* 2015) and in previous experiments where SeNPs were clearly unstable (see Chapter 3).[57]

In summary, we have achieved well-preserved particles aligning FtsZ protofilaments using a disproportionation reaction to transform SeNPs into various MSeNPs. In shelling the SeNPs with $KMnO_4$, it was difficult to discern punctate particles from metal precipitation within cells. This is because of the reactivity of $KMnO_4$ with phosphate groups natively present *in vivo*, which causes severe precipitation even in the control samples as was observed. Despite assignment ambiguity, $KMnO_4$ did appear to preferentially stain areas of the cells that should have contained SeNPs as was judged by contrast and elemental mapping. Even though it is not an ideal option for protecting SeNPs against degradation, it led to further disproportionation studies because of its plausibility.

Regarding Zn^{2+} and Cd^{2+} disproportionated samples, both appeared to react with the SeNPs as was judged by particle morphology and by elemental data. In these samples, the particles were much more defined against the background of the cell compared to the $KMnO_4$ sample. However, unlike the disproportionation study conducted in Chapter 4, the lattice spacings and diffraction patterns of the particles were unattainable. This could be explained either by excessive electron scattering within the ~100 nm of resin, causing a blurring of our view of the crystalline particles, or by an incomplete disproportionation reaction to MSeNP. It is clear that more experimentation

will be required not only to improve the morphology of the particles within but also to ensure that the particles are forming crystalline MSeNPs.

On the other hand, Ag^+ and Cu^{2+} samples contained well-formed spherical particles aligning the membrane as is expected from FtsZ. It is possible that the sample reacted with Ag^+ has a degree of background AgNP formation either due to reactions with other biomolecules or to the active site of the enzyme itself. Other studies need to be conducted on *E. coli* that do not contain the chimera to confirm whether this particle formation is a result of side reactions with cSeNP or with native biomolecules such as glutathione. Regardless, it does appear that most particles within the Ag^+ reacted sample are aligning the membrane as we would expect of labeled FtsZ, suggesting that Ag disproportionation is possible.

Finally, it is clear that the most promising work involved reacting biogenic SeNPs with Cu^{2+} to form Cu_xSe_yNPs labeling FtsZ. Tomograms were reconstructed from tilt series collected at CU Boulder. Our initial method of label validation involved measuring particle distance from the outer membrane to determine if the distribution was random or well-ordered. Based on this plot, it is clear that particles with good morphology are aligning the interior of the membrane within 50 nm, which matches well with FtsZ localization from previous experiments. To further confirm a successful labeling attempt, we analyzed a tomogram of a cell at a late stage division point. In viewing this sample, it is clear that particles are aligning a constriction point within the membrane in an ordered array, as if the particles themselves are exerting a constrictive force on the membrane. This type of order is also routinely observed in experiments involving FtsZ filamentation. Overall, it is apparent that the particles were able to survive the processing methods used during dehydration and infiltration, and we were able to label a specific target of interest using a clonable nanoparticle tag.

Outlook

We have shown that cSeNP is a viable labeling strategy for high resolution localization of proteins within a cell using electron tomography. While we have shown that the label can be used with standard preservation protocols, we envision that SeNPs can be used as is (without post-synthetic transformation) in vitrification preparations for analysis using techniques like cryo-focused ion beam scanning electron microscopy (FIB-SEM).[142] We expect that the SeNP label alone would be sufficient to generate contrast, since the sample is immediately vitrified and maintained as such for lamella preparation and image collection. When using this technique to study proteins that are more sparsely distributed within a cell, it is highly desirable to use a correlative approach to first find the best places to mill the sample and create lamella. In this case, forming fluorescent ZnSe particles using the disproportionation style reaction to label the protein *in vivo* would be ideal, as Zn^{2+} is much less toxic than Cd^{2+}.

Overall, clonable nanoparticle technology is an extremely promising method for high resolution localization of proteins of interest with cryo-electron tomography. Furthermore, with recent and continual development of direct electron detectors, energy filters, and automated dataset acquisition, it will soon be possible to not only localize the protein with this label but also to resolve its structure to atomic precision. While the focus of this text has been on microscopic imaging, clonable nanoparticle labeling technology also has the potential to be used in medical imaging modalities involving X-ray tomography.[44,143] In this regard, specific cell types would be easily distinguishable with respect to the body. In another sense, the upregulation or downregulation of a specific biomarker could be tracked *in situ* under specific circumstances, allowing us to better understand cellular processes and target disease markers within an organism.

REFERENCES

1. Zanotti, G. Cryo-EM and X-Ray Crystallography: Complementary or Alternative Techniques? *NanoWorld J.* **2**, 22–23 (2016).
2. Yu, H. Extending the size limit of protein nuclear magnetic resonance. **96**, 332–334 (1999).
3. Gaietta, G. *et al.* Multicolor and electron microscopic imaging of connexin trafficking. *Science (80-.).* **296**, 503–507 (2002).
4. Huang, B., Bates, M. & Zhuang, X. Super-Resolution Fluorescence Microscopy. *Annu. Rev. Biochem.* **78**, 993–1016 (2009).
5. Tsien, R. Y. Imagining imaging ' s future. *Imaging Cell Biol.* **249**, 16–21 (2003).
6. Huang, B., Babcock, H. & Zhuang, X. Breaking the diffraction barrier: Super-resolution imaging of cells. *Cell* **143**, 1047–1058 (2010).
7. Tuijtel, M. W., Koster, A. J., Jakobs, S., Faas, F. G. A. & Sharp, T. H. Correlative cryo super-resolution light and electron microscopy on mammalian cells using fluorescent proteins. *Sci. Rep.* **9**, 1–11 (2019).
8. Thorley, J. a, Pike, J. & Rappoport, J. Z. Super-resolution Microscopy : A Comparison of Commercially Available Options. *Fluoresc. Microsc.* 199–212 (2014). doi:10.1016/B978-0-12-409513-7.00014-2
9. Fernández-Suárez, M. & Ting, A. Y. Fluorescent probes for super-resolution imaging in living cells. *Nat. Rev. Mol. Cell Biol.* **9**, 929–943 (2008).
10. Johnson, E. *et al.* Correlative in-resin super-resolution and electron microscopy using standard fluorescent proteins. *Sci. Rep.* **5**, 1–8 (2015).
11. Zivanov, J. *et al.* RELION-3: New tools for automated high-resolution cryo-EM structure determination. *bioRxiv* 1–22 (2018). doi:10.1101/421123
12. Nakane, T. *et al.* Single-particle cryo-EM at atomic resolution. *Nature* **587**, 152–156 (2020).
13. Nwanochie, E. & Uversky, V. N. Structure determination by single-particle cryo-electron microscopy: Only the sky (and intrinsic disorder) is the limit. *Int. J. Mol. Sci.* **20**, (2019).
14. Kuhlbrandt, W. The Resolution Revolution. *Science (80-.).* **343**, 1443–1444 (2014).
15. Tegunov, D., Xue, L., Dienemann, C., Cramer, P. & Mahamid, J. Multi-particle cryo-EM refinement with M visualizes ribosome-antibiotic complex at 3.5 Å in cells. *Nat. Methods* **18**, 186–193 (2021).
16. Yip, K. M., Fischer, N., Paknia, E., Chari, A. & Stark, H. Atomic-resolution protein structure determination by cryo-EM. *Nature* **587**, 157–161 (2020).
17. Blakeley, M. P., Hasnain, S. S. & Antonyuk, S. V. Sub-atomic resolution X-ray crystallography and neutron crystallography: Promise, challenges and potential. *IUCrJ* **2**, 464–474 (2015).
18. Zhou, H. *et al.* Programming Conventional Electron Microscopes for Solving Ultrahigh-Resolution Structures of Small and Macro-Molecules. *Anal. Chem.* **91**, 10996–11003 (2019).
19. Williams, D. B. & Carter, C. B. *Transmission Electron Microscopy*. *Transmission Electron Microscopy* (2009). doi:10.1007/978-0-387-76501-3_1
20. McIntosh, R., Nicastro, D. & Mastronarde, D. New views of cells in 3D: An introduction to electron tomography. *Trends Cell Biol.* **15**, 43–51 (2005).
21. Lloyd, G. E. Atomic Number and Crystallographic Contrast Images with the SEM: A

Review of Backscattered Electron Techniques. *Mineral. Mag.* **51**, 3–19 (1987).
22. Reimer, L. & Kohl, H. *Transmission Electron Microscopy Physics of Image Formation*. *Springer series in optical sciences* **51**, (2008).
23. Goldstein, J. I. *et al. Scanning Electron Microscopy and X-Ray Microanalysis*. (2018). doi:10.1007/978-1-4939-6676-9
24. Goldstein, J. *et al. Scanning Electron Microscopy and X-Ray Microanalysis*. (Kluwer Academic Plenum Publishers, 2003).
25. McDonald, K. L. & Auer, M. High-Pressure Freezing, Cellular Tomography, and Structural Cell Biology. *Biotechniques* **41**, 137–143 (2006).
26. Watson, M. L. Staining of Tissue Sections for Electron Microscopy with Heavy Metals. *J. Biophys. Biochem. Cytol.* **4**, 475–478 (1958).
27. Hayat, M. A. *Basic Techniques for Transmission Electron Microscopy*. (Elsevier, 1986). doi:10.1016/B978-0-12-333926-3.X5001-5
28. Adams, S. R. *et al.* Multicolor Electron Microscopy for Simultaneous Visualization of Multiple Molecular Species. *Cell Chem. Biol.* **23**, 1417–1427 (2016).
29. Bi, E. & Lutkenhaus, J. FtsZ ring structure associated with division in Escherichia coli. *Nature* **354**, 161–164 (1991).
30. Lancelle, S. A. & Hepler, P. K. Immunogold labelling of actin on sections of freeze-substituted plant cells. *Protoplasma* **150**, 72–74 (1989).
31. Giepmans, B. N. G., Adams, S. R., Ellisman, M. H. & Tsien, R. Y. The fluorescent toolbox for assessing protein location and function. *Science (80-.).* **312**, 217–224 (2006).
32. Ngo, J. T. *et al.* Click-EM for imaging metabolically tagged nonprotein biomolecules. *Nat. Chem. Biol.* **12**, 459–465 (2016).
33. Shu, X. *et al.* A genetically encoded tag for correlated light and electron microscopy of intact cells, tissues, and organisms. *PLoS Biol.* **9**, (2011).
34. Birrell, B., Hedberg, K. & Griffith, H. Pitfalls of Immunogold Labeling: Analysis by Light Microscopy, Transmission Electron Microscopy, and Photoelectron Microscopy. *J. Histochem. Cytochem.* **35**, 843–853 (1987).
35. Murtey, M. Das. Immunogold Techniques in Electron Microscopy. in *Modern Electron Microscopy in Physical and Life Sciences* **2**, 64 (InTech, 2016).
36. Melo, R. C. N., Morgan, E., Monahan-Earley, R., Dvorak, A. M. & Weller, P. F. Pre-embedding immunogold labeling to optimize protein localization at subcellular compartments and membrane microdomains of leukocytes. *Nat. Protoc.* **9**, 2382–2394 (2014).
37. Tsien, R. Y. Nobel lecture: Constructing and exploiting the fluorescent protein paintbox. *Integr. Biol.* **2**, 77–93 (2010).
38. Tsien, R. Y. The Green Fluorescent Protein. *Annu. Rev. Biochem.* **67**, 509–544 (1998).
39. Glazer, A. N. Phycobiliproteins — a family of valuable, widely used fluorophores. *J. Appl. Phycol.* **6**, 105–112 (1994).
40. Tsien, R. Y. Fluorescence readouts of biochemistry in live cells and organisms. *Mol. imaging Princ. Pract.* 808–828 (2009).
41. Martell, J. D., Deerinck, T. J., Lam, S. S., Ellisman, M. H. & Ting, A. Y. Electron microscopy using the genetically encoded APEX2 tag in cultured mammalian cells. *Nat. Protoc.* **12**, 1792–1816 (2017).
42. Martell, J. D. *et al.* Engineered ascorbate peroxidase as a genetically encoded reporter for electron microscopy. *Nat. Biotechnol.* **30**, 1143–1148 (2012).

43. Ingale, A. G. & Chaudhari, A. N. Biogenic synthesis of nanoparticles and potential applications: An eco-friendly approach. *J. Nanomedicine Nanotechnol.* **4**, 7 (2013).
44. Singh, P., Kim, Y.-J., Zhang, D. & Yang, D.-C. Biological Synthesis of Nanoparticles from Plants and Microorganisms. *Trends Biotechnol.* **34**, 588–599 (2016).
45. Salman, M. S. *et al.* Lysozyme-Templated Meso-Macroporous Hollow TiO2 for Lithium Ion Battery Anode. *ACS Appl. Nano Mater.* **1**, 698–710 (2018).
46. Wu, L. Q. & Payne, G. F. Biofabrication: Using biological materials and biocatalysts to construct nanostructured assemblies. *Trends Biotechnol.* **22**, 593–599 (2004).
47. Thakkar, K. N., Mhatre, S. S. & Parikh, R. Y. Biological synthesis of metallic nanoparticles. *Nanomedicine Nanotechnology, Biol. Med.* **6**, 257–262 (2010).
48. Ovais, M. *et al.* Biosynthesis of Metal Nanoparticles via Microbial Enzymes: A Mechanistic Approach. *Int. J. Mol. Sci.* **19**, 4100 (2018).
49. Yamashita, I., Hayashi, J. & Hara, M. Bio-template synthesis of uniform CdSe nanoparticles using cage-shaped protein, apoferritin. *Chem. Lett.* **33**, 1158–1159 (2004).
50. Eby, D. M., Farrington, K. E. & Johnson, G. R. Synthesis of Bioinorganic Antimicrobial Peptide Nanoparticles with Potential Therapeutic Properties. *Biomacromolecules* **9**, 2487–2494 (2008).
51. Iwahori, K., Yoshizawa, K., Muraoka, M. & Yamashita, I. Fabrication of ZnSe nanoparticles in the apoferritin cavity by designing a slow chemical reaction system. *Inorg. Chem.* **44**, 6393–6400 (2005).
52. Dickerson, M. B., Sandhage, K. H. & Naik, R. R. Protein- and peptide-directed syntheses of inorganic materials. *Chem. Rev.* **108**, 4935–4978 (2008).
53. Prasad, R., Pandey, R. & Barman, I. Engineering tailored nanoparticles with microbes: Quo vadis? *Wiley Interdiscip. Rev. Nanomedicine Nanobiotechnology* **8**, 316–330 (2016).
54. Akhtar, M. S., Panwar, J. & Yun, Y.-S. Biogenic Synthesis of Metallic Nanoparticles by Plant Extracts. *ACS Sustain. Chem. Eng.* **1**, 591–602 (2013).
55. Flynn, C. E. *et al.* Synthesis and organization of nanoscale II-VI semiconductor materials using evolved peptide specificity and viral capsid assembly. *J. Mater. Chem.* **13**, 2414–2421 (2003).
56. Portney, N. G., Martinez-Morales, A. A. & Ozkan, M. O. Nanoscale memory characterization of virus-templated semiconducting quantum dots. *ACS Nano* **2**, 191–196 (2008).
57. Ni, T. W. *et al.* Progress toward clonable inorganic nanoparticles. *Nanoscale* **7**, 17320–17327 (2015).
58. Sears, M. E. Chelation: Harnessing and enhancing heavy metal detoxification - A review. *Sci. World J.* **2013**, (2013).
59. Haas, K. L. & Franz, K. J. Application of Metal Coordination Chemistry To Explore and Manipulate Cell Biology. *Chem. Rev.* **109**, 4921–4960 (2009).
60. Staicu, L. C. *et al.* Pseudomonas moraviensis subsp. stanleyae, a bacterial endophyte of hyperaccumulator Stanleya pinnata , is capable of efficient selenite reduction to elemental selenium under aerobic conditions. *J. Appl. Microbiol.* **119**, 400–410 (2015).
61. Fu, F. & Wang, Q. Removal of heavy metal ions from wastewaters: A review. *J. Environ. Manage.* **92**, 407–418 (2011).
62. Thorgersen, M. P. *et al.* Mechanisms of chromium and uranium toxicity in pseudomonas stutzeri RCH2 grown under anaerobic nitrate-reducing conditions. *Front. Microbiol.* **8**, 1–12 (2017).

63. Hall, J. L. Cellular mechanisms for heavy metal detoxification and tolerance. *J. Exp. Bot.* **53**, 1–11 (2002).
64. Fox, B. & Walsh, C. T. Mercuric reductase. Purification and characterization of a transposon-encoded flavoprotein containing an oxidation-reduction-active disulfide. *J. Biol. Chem.* **257**, 2498–2503 (1982).
65. Mukhopadhyay, R. & Rosen, B. P. Arsenate reductases in prokaryotes and eukaryotes. *Environ. Health Perspect.* **110**, 745–748 (2002).
66. Gadd, G. M. Metals, minerals and microbes: Geomicrobiology and bioremediation. *Microbiology* **156**, 609–643 (2010).
67. Schiiler, D. and Frankel, R. B. . Bacterial magnetosomes,biomineralization and biotechnological applications. *Microbial. Biotechnol* 464–473 (1999).
68. Maruyama, T. *et al.* Proteins and protein-rich biomass as environmentally friendly adsorbents selective for precious metal ions. *Environ. Sci. Technol.* **41**, 1359–1364 (2007).
69. Tiwari, S. & Lata, C. Heavy metal stress, signaling, and tolerance due to plant-associated microbes: An overview. *Front. Plant Sci.* **9**, 1–12 (2018).
70. Rascio, N. & Navari-Izzo, F. Heavy metal hyperaccumulating plants: How and why do they do it? And what makes them so interesting? *Plant Sci.* **180**, 169–181 (2011).
71. Kiran, M. G., Pakshirajan, K. & Das, G. Heavy metal removal from multicomponent system by sulfate reducing bacteria: Mechanism and cell surface characterization. *J. Hazard. Mater.* **324**, 62–70 (2017).
72. Gorby, Y. A. *et al.* Electrically conductive bacterial nanowires produced by Shewanella oneidensis strain MR-1 and other microorganisms. *Proc. Natl. Acad. Sci.* **103**, 11358–11363 (2006).
73. Wall, J. D. & Krumholz, L. R. Uranium Reduction. *Annu. Rev. Microbiol.* **60**, 149–166 (2006).
74. Soo Choi, H. *et al.* Renal clearance of quantum dots. *Nat. Biotechnol.* **25**, 1165–1170 (2007).
75. Longmire, M., Choyke, P. L. & Kobayashi, H. Clearance properties of nano-sized particles and molecules as imaging agents: considerations and caveats. *Nanomedicine* **3**, 703–717 (2008).
76. Staicu, L. C. *et al.* Pseudomonas moraviensis subsp. stanleyae, a bacterial endophyte of hyperaccumulator Stanleya pinnata , is capable of efficient selenite reduction to elemental selenium under aerobic conditions. *J. Appl. Microbiol.* **119**, 400–410 (2015).
77. Zhang, J. *et al.* Two selenium tolerant Lysinibacillus sp. strains are capable of reducing selenite to elemental Se efficiently under aerobic conditions. *J. Environ. Sci.* **77**, 238–249 (2019).
78. Butz, Z. J., Borgognoni, K., Nemeth, R., Nilsson, Z. N. & Ackerson, C. J. Metalloid Reductase Activity Modified by a Fused Se 0 Binding Peptide. *ACS Chem. Biol.* **15**, 1987–1995 (2020).
79. Torreggiani, A., Tamba, M. & Fini, G. Binding of Copper (II) to Carnosine : Raman and IR Spectroscopic Study. *Biopolymner(Biospectroscopy)* **57**, 149–159 (2000).
80. Takeuchi, H. Raman structural markers of tryptophan and histidine side chains in proteins. *Biopolym. - Biospectroscopy Sect.* **72**, 305–317 (2003).
81. Zhu, G., Zhu, X., Fan, Q. & Wan, X. Raman spectra of amino acids and their aqueous solutions. *Spectrochim. Acta - Part A Mol. Biomol. Spectrosc.* **78**, 1187–1195 (2011).
82. Toyama, A., Ono, K., Hashimoto, S. & Takeuchi, H. Raman spectra and normal

coordinate analysis of the N1-H and N3-H tautomers of 4-methylimidazole: Vibrational modes of histidine tautomer markers. *J. Phys. Chem. A* **106**, 3403–3412 (2002).
83. Schirer, A., El Khoury, Y., Faller, P. & Hellwig, P. Similarities and differences of copper and zinc cations binding to biologically relevant peptides studied by vibrational spectroscopies. *J. Biol. Inorg. Chem.* **22**, 581–589 (2017).
84. Hasegawa, K., Ono, T. & Noguchi, T. Vibrational Spectra and Ab Initio DFT Calculations of 4-Methylimidazole and Its Different Protonation Forms: Infrared and Raman Markers of the Protonation State of a Histidine Side Chain. *J. Phys. Chem. B* **104**, 4253–4265 (2000).
85. Lucovsky, G., Mooradian, A., Taylor, W., Wright, G. B. & Keezer, R. C. Identification of the Fundamental Vibrational Modes of Trigonal, a-Monoclinic and Amorphous Selenium. *Solid State Commun.* **5**, 113–117 (1967).
86. Singh, B. R. *Infrared Analysis of Peptides and Proteins*. **750**, (American Chemical Society, 1999).
87. Lippert, J. L., Tyminski, D. & Desmeules, P. J. Determination of the Secondary Structure of Proteins by Laser Raman Spectroscopy. *J. Am. Chem. Soc.* **98**, 7075–7080 (1976).
88. Williams, R. W. Estimation of protein secondary structure from the laser Raman amide I spectrum. *J. Mol. Biol.* **166**, 581–603 (1983).
89. Ye, S., Li, H., Yang, W. & Luo, Y. Accurate Determination of Interfacial Protein Secondary Structure by Combining Interfacial-Sensitive Amide I and Amide III Spectral Signals. *J. Am. Chem. Soc.* 2–5 (2014). doi:10.1021/ja411081t
90. Bandekar, J. Amide modes and protein conformation. *Biochim. Biophys. Acta* **1120**, 123–143 (1992).
91. Talari, A. C. S., Movasaghi, Z., Rehman, S. & Rehman, I. U. Raman spectroscopy of biological tissues. *Appl. Spectrosc. Rev.* **50**, 46–111 (2015).
92. Barth, A. Infrared spectroscopy of proteins. *Biochim. Biophys. Acta - Bioenerg.* **1767**, 1073–1101 (2007).
93. Chu, D. B. K., Owen, J. S. & Peters, B. Nucleation and Growth Kinetics from LaMer Burst Data. *J. Phys. Chem. A* **121**, 7511–7517 (2017).
94. Lu, L., Sevonkaev, I., Kumar, A. & Goia, D. V. Strategies for tailoring the properties of chemically precipitated metal powders. *Powder Technol.* **261**, 87–97 (2014).
95. Lutkenhaus, J. Assembly dynamics of the bacterial minCDE system and spatial regulation of the z ring. *Annu. Rev. Biochem.* **76**, 539–562 (2007).
96. Li, Z., Trimble, M. J., Brun, Y. V & Jensen, G. J. The structure of FtsZ filaments in vivo suggests a force-generating role in cell division. *EMBO J.* **26**, 4694–4708 (2007).
97. Shen, B. & Lutkenhaus, J. The conserved C-terminal tail of FtsZ is required for the septal localization and division inhibitory activity of MinCC/MinD. *Mol. Microbiol.* **72**, 410–424 (2009).
98. Kumar, P., Yadav, A., Fishov, I. & Feingold, M. Z-ring structure and constriction dynamics in E. coli. *Front. Microbiol.* **8**, 1–9 (2017).
99. Huecas, S. *et al.* Self-Organization of FtsZ Polymers in Solution Reveals Spacer Role of the Disordered C-Terminal Tail. *Biophys. J.* **113**, 1831–1844 (2017).
100. Liu, R. *et al.* Three-Dimensional Superresolution Imaging of the FtsZ Ring during Cell Division of the Cyanobacterium Prochlorococcus. *MBio* **8**, (2017).
101. Daley, D. O., Skoglund, U. & Söderström, B. FtsZ does not initiate membrane constriction at the onset of division. *Sci. Rep.* **6**, 1–6 (2016).

102. Holden, S. J. *et al.* High throughput 3D super-resolution microscopy reveals Caulobacter crescentus in vivo Z-ring organization. *Proc. Natl. Acad. Sci. U. S. A.* **111**, 4566–4571 (2014).
103. Liu. crossm Imaging of the FtsZ Ring during Cell Division of the Cyanobacterium. **8**, 1–11 (2017).
104. Szwedziak, P., Wang, Q., Bharat, T. A. M., Tsim, M. & Löwe, J. Architecture of the ring formed by the tubulin homologue FtsZ in bacterial cell division. *Elife* **3**, e04601 (2014).
105. Ma, X., Ehrhardt, D. W. & Margolin, W. Colocalization of cell division proteins FtsZ and FtsA to cytoskeletal structures in living *Escherichia coli* cells by using green fluorescent protein. *Proc. Natl. Acad. Sci. U. S. A.* **93**, 12998–3003 (1996).
106. Mückl, A., Schwarz-Schilling, M., Fischer, K. & Simmel, F. C. Filamentation and restoration of normal growth in E.coli using a combined CRISPRi sgRNA/antisense RNA approach. *bioRxiv* 1–19 (2018). doi:10.1101/323212
107. Lucovsky, G. *THE S T R U C T U R E OF A M O R P H O U S SELENIUM F R O M I N F R A R E D. THE PHYSICS OF SELENIUM AND TELLURIUM: Proceedings of the International Symposium held at Montreal, Canada October 12–13, 1967 and sponsored by the Selenium-Tellurium Development Association, Inc. 345 East 47th Street, New York, N.Y. 10017* (Pergamon Press Inc., 1967). doi:10.1016/B978-0-08-013895-4.50025-8
108. Corb, B. W., Wei, W. D. & Averbach, B. L. Atomic models of amorphous selenium. *J. Non. Cryst. Solids* **53**, 29–42 (1982).
109. Jeong, U. & Xia, Y. Synthesis and crystallization of monodisperse spherical colloids of amorphous selenium. *Adv. Mater.* **17**, 102–106 (2005).
110. van Embden, J., Chesman, A. S. R. & Jasieniak, J. J. The Heat-Up Synthesis of Colloidal Nanocrystals. *Chem. Mater.* **27**, 2246–2285 (2015).
111. Zhang, H. Y., Hu, Z. Q. & Lu, K. Transformation from the amorphous to the nanocrystalline state in pure selenium. *Nanostructured Mater.* **5**, 41–52 (1995).
112. Riskowski, R. A., Nemeth, R. S., Borgognoni, K. & Ackerson, C. J. Enzyme-Catalyzed in Situ Synthesis of Temporally and Spatially Distinct CdSe Quantum Dots in Biological Backgrounds. *J. Phys. Chem. C* **123**, 27187–27195 (2019).
113. Muszyńska, E. & Labudda, M. Dual role of metallic trace elements in stress biology—from negative to beneficial impact on plants. *Int. J. Mol. Sci.* **20**, (2019).
114. Manna, L., Scher, E. C. & Alivisatos, A. P. Synthesis of soluble and processable rod-, arrow-, teardrop-, and tetrapod-shaped CdSe nanocrystals. *J. Am. Chem. Soc.* **122**, 12700–12706 (2000).
115. Wei, Y., Yang, J., Lin, A. W. H. & Ying, J. Y. Highly reactive se precursor for the phosphine-free synthesis of metal selenide nanocrystals. *Chem. Mater.* **22**, 5672–5677 (2010).
116. Gu, Y.-P., Cui, R., Zhang, Z.-L., Xie, Z.-X. & Pang, D.-W. Ultrasmall Near-Infrared Ag 2 Se Quantum Dots with Tunable Fluorescence for in Vivo Imaging. *J. Am. Chem. Soc.* **134**, 79–82 (2012).
117. Application, F. & Data, P. United States Patent (19). (1973).
118. Ouchi, A. *et al.* Room-temperature reaction between laser chemical vapor deposited selenium and some metals. *Chem. Mater.* **16**, 3439–3445 (2004).
119. Jeong, U., Wang, Y., Ibisate, M. & Xia, Y. Some new developments in the synthesis, functionalization, and utilization of monodisperse colloidal spheres. *Adv. Funct. Mater.* **15**, 1907–1921 (2005).

120. Wang, W., Geng, Y., Qian, Y., Ji, M. & Xie, Y. Novel room temperature method to nanocrystalline Ag2Se. *Mater. Res. Bull.* **34**, 877–882 (1999).
121. Camargo, P. H. C., Lee, Y. H., Jeong, U., Zou, Z. & Xia, Y. Cation exchange: A simple and versatile route to inorganic colloidal spheres with the same size but different compositions and properties. *Langmuir* **23**, 2985–2992 (2007).
122. Gates, B. *et al.* Synthesis and Characterization of Crystalline Ag2Se Nanowires Through a Template-Engaged Reaction at Room Temperature. *Adv. Funct. Mater.* **12**, 679–682 (2002).
123. Mayers, B., Jiang, X., Sunderland, D., Cattle, B. & Xia, Y. Hollow Nanostructures of Platinum with Controllable Dimensions Can Be Synthesized by Templating Against Selenium Nanowires and Colloids. *J. Am. Chem. Soc.* **125**, 13364–13365 (2003).
124. Jiang, X., Mayers, B., Herricks, T. & Xia, Y. Direct Synthesis of Se@CdSe Nanocables and CdSe Nanotubes by Reacting Cadmium Salts with Se Nanowires. *Adv. Mater.* **15**, 1740–1743 (2003).
125. Balavandy, S. K., Shameli, K., Biak, D. R. B. A. & Abidin, Z. Z. Stirring time effect of silver nanoparticles prepared in glutathione mediated by green method. *Chem. Cent. J.* **8**, 11 (2014).
126. Olin, Å., Noläng, B., Öhman, L., Osadchii, E. & Rosén, E. Chemical Thermodynamics Volume 7: Chemical thermodynamics of selenium. *Chem. Thermodyn.* **7**, 851 (2005).
127. Nath, S., Ghosh, S. K., Panigahi, S., Thundat, T. & Pal, T. Synthesis of selenium nanoparticle and its photocatalytic application for decolorization of methylene blue under UV irradiation. *Langmuir* **20**, 7880–7883 (2004).
128. Julien, C. M. & Mauger, A. Nanostructured MnO2 as electrode materials for energy storage. *Nanomaterials* **7**, (2017).
129. Lee, S. W., Mao, C., Flynn, C. E. & Belcher, A. M. Ordering of quantum dots, using genetically engineered viruses. *Science (80-.).* **296**, 892–895 (2002).
130. Abendroth, J. M., Bushuyev, O. S., Weiss, P. S. & Barrett, C. J. Controlling Motion at the Nanoscale: Rise of the Molecular Machines. *ACS Nano* **9**, 7746–7768 (2015).
131. Sauer, M. & Heilemann, M. Single-Molecule Localization Microscopy in Eukaryotes. *Chem. Rev.* **117**, 7478–7509 (2017).
132. Schorb, M., Haberbosch, I., Hagen, W. J. H., Schwab, Y. & Mastronarde, D. N. Software tools for automated transmission electron microscopy. *Nat. Methods* **16**, 471–477 (2019).
133. Beck, M. & Baumeister, W. Cryo-Electron Tomography: Can it Reveal the Molecular Sociology of Cells in Atomic Detail? *Trends Cell Biol.* **26**, 825–837 (2016).
134. McIntosh, J. R. Electron microscopy of cells: A new beginning for a new century. *J. Cell Biol.* **153**, F25–F32 (2001).
135. Severs, N. J. Freeze-fracture electron microscopy. *Nat. Protoc.* **2**, 547–576 (2007).
136. Maclean, N. ELECTRON MICROSCOPY OF A FISSION YEAST, SCHIZOSACCHAROMYCES POMBE. *J. Bacteriol.* **88**, 1459–1466 (1964).
137. Cleasby, J. L., Baumann, E. R. & Black, C. D. Effectiveness of Potassium Permanganate for Disinfection. *J. Am. Water Works Assoc.* **56**, 466–474 (1964).
138. Rahman, A. *et al.* A Mechanistic View of the Light-Induced Synthesis of Silver Nanoparticles Using Extracellular Polymeric Substances of Chlamydomonas reinhardtii. *Molecules* **24**, 3506 (2019).
139. Lesnichaya, M. V., Sukhov, B. G., Shendrik, R. Y., Sapozhnikov, A. N. & Trofimov, B. A. Synthesis of water-soluble silver selenide quantum dots luminescing within the

transparency window of biological tissues. *Russ. J. Gen. Chem.* **88**, 284–287 (2018).
140. Khan, H., Khan, M. F., Asim-ur-Rehman, Jan, S. U. & Ullah, N. The protective role of glutathione in silver induced toxicity in blood components. *Pak. J. Pharm. Sci.* **24**, 123–8 (2011).
141. Wagstaff, J. M. *et al.* A polymerization-associated structural switch in ftsz that enables treadmilling of model filaments. *MBio* **8**, 1–16 (2017).
142. Kizilyaprak, C., Bittermann, A. G., Daraspe, J. & Humbel, B. *Electron Microscopy. Electron Microscopy: Methods and Protocols* **1117**, (Humana Press, 2014).
143. Mahan, M. M. & Doiron, A. L. Gold Nanoparticles as X-Ray, CT, and Multimodal Imaging Contrast Agents: Formulation, Targeting, and Methodology. *J. Nanomater.* **2018**, 1–15 (2018).
144. Rakgalakane, B. P. & Moloto, M. J. Aqueous synthesis and characterization of CdSe/ZnO core-shell nanoparticles. *J. Nanomater.* **2011**, (2011).
145. Osman, D. & Mustafa, M. Synthesis and Characterization of Zinc Oxide Nanoparticles using Zinc Acetate Dihydrate and Sodium Hydroxide. *J. Nanosci. Nanoeng.* **1**, 248–251 (2015).
146. Yue, Q. *et al.* Fluorescence property of ZnO nanoparticles and the interaction with bromothymol blue. *J. Fluoresc.* **21**, 1131–1135 (2011).

APPENDIX A: Supplemental to Chapter 2

Materials

BL21(DE3) *E. coli* were purchased from New England Biolabs. Antibiotics were purchased from GoldBio. Na_2SeO_3 and $HNaSeO_3$ were purchased from Alfa Aesar. NADPH was purchased from BioVision and Coomassie Plus Bradford Reagent from Thermo Scientific. GeneJet Plasmid Miniprep Kit (Cat# K0503) and PCR Cleanup Kit (Cat# K0702) were purchased from ThermoFisher Scientific. Additionally, $NaBH_4$ was purchased from Merck and SeBP (sequence LTPHKHHKHLHA) was made by GenScript.

Methods

Enzyme isolation and characterization

10mL cultures of BL21(DE3) cells containing the GRLMR-SeBP or GRLMR were started and grown O/N in a shaker at 37°C and 225 RPM. The dense cultures were diluted into 1 L of LB Kan/Cam and allowed to grow until an OD_{600} ~0.5-0.6. Induction was started using a 1 mM final concentration of IPTG and was supplemented with 1 µM of $HNaSeO_3$. Growth was O/N at 37°C. Cells were then spun down at 14000 RPM for 20 minutes and resuspended into B-PER and sonicated to lyse the cells. The insoluble cell debris was removed by centrifugation and the soluble cell lysate was collected for Ni-NTA purification. Nickel columns were prepared using Ni-NTA agarose beads. Beads were washed as follows: 3 x 3 column volumes of H2O, 3 x 3 column volumes of binding buffer (50 mM Tris-HCl (pH 8), 5 mM imidazole, 100 mM NaCl). The lysate was then run through the column 3 x before 4 cycles of washing the column using washing buffer (50 mM Tris-HCl (pH 8), 20 mM imidazole, 300 mM NaCl). Finally, the column was incubated with column volume of elution buffer (50 mM Tris-HCl (pH 8), 300 mM imidazole, 50 mM NaCl) for at least 5 minutes before the elution buffer was collected. The isolated protein solution was

dialyzed into PBS before the concentration was collected using UV-Vis and stored at -80°C in aliquots for further study. A native PAGE gel was then run to ensure the positively charged SeBP was present on the isolated GRLMR.

Enzymatic SeNP formation

Particles were made by adding 100 µg of enzyme and aliquots of a 100 mM $HNaSeO_3$ solution to PBS, pH 7.4. The reaction was then started by the introduction of NADPH and allowed to react for several hours. After, the SeNPs were spun down and separated from the supernatant for further study.

Bradford assay for SeNP retention of GRLMR vs cSeNP

Stocks of enzyme in PBS, pH 7.4 at various concentrations were prepared of which 100 µL were diluted by 900 µL of Bradford reagent. Standard curves were collected for both the GRLMR and cSeNP (GRLMR-$SeBP_2$ construct) by monitoring the absorbance at 595 nm, each point being performed in triplicate. Samples were then prepared for measurement in the same fashion by taking 100 µL of the target solution and diluting it up with 900 µL Bradford reagent. The concentration was then calculated by monitoring the absorbance at 595 nm and performed in triplicate.

DLS Assay of SeNP size growth in presence of GRLMR vs cSeNP

Reactions for DLS monitoring were prepared in disposable plastic cuvettes as described above. SeNP formation was monitored using a refractive index of 2.6 and an absorbance of 0.5 for α-Se and a refractive index and viscosity of PBS of 1.332 and 0.8898 cP, respectively. Reactions ran for at least 4 hours at RT. Each point in DLS was an aggregate of 1 – 14 reads depending on the quality of data collected, determined by the Zetasizer Nano ZS software.

Synthesis of SeBP capped Selenium Nanoparticles (SeBP-SeNP)

Peptide-capped SeNPs were synthesized based on the method from Nath *et. al.* For the SeNPs, 50 – 100 µL of acidic 10 mM SeO_3^{2-} and 0.5 – 1.0 mL of 10 mM $NaBH_4$ (aq) were added to a 15 mL conical tube and diluted to a final volume of 1.5 – 3.0 mL with 18.2 mΩ ultrapure (Up) H_2O. The solution was mixed and placed on a rocker for 90 – 300 seconds, after which 50 – 100 µL of 10 mM of the SeBP was added and thoroughly mixed into the solution and placed back on the rocker. Within 10 minutes the tube was placed in an ice bag and allowed to conjugate for 4 hours on the rocker. After this, the solution was added to a 3,500 MW cutoff dialysis bag and dialyzed on ice in 2.0 L UpH_2O for at least 2 hours. The resulting mixture was extracted from the dialysis bag and lyophilized and stored in a refrigerator until ready for analysis. The sample was diluted into 50 µL of pH 7.4 1x PBS.

Raman Spectroscopy

Raman spectra were collected using an inverted Raman microscope with an Olympus IX73 frame and objectives with a Horiba iHR 550 Spectrometer with a neural synapse thermoelectrically cooled charge-coupled device (CCD) detector attached to a Horiba ONDAX T-Hz Raman 532 nm laser provided by Justin Sambur. This setup was accompanied with a LabSpec software package. The specimen was prepared by drop-casting 3-7 µL of sample onto a glass cover slip and allowed to dry in air at room temperature. We used double-sided tape to seal the sample and to adhere the coverslip to a glass slide. Spectra were collected using an incident laser power of 83 mW. We used a 60x water objective with a 1200 blazes/mm grating, which has a resolution of approximately 2 cm^{-1} per pixel. We manually focused the laser on the sample using the optical setup. If signal was insufficient, we refocused the laser until signal was obtained. We used the software's denoiser program, which is essentially a smoothing algorithm, to obtain a smoother curve. Backscatter collection ranged from 30 – 300 seconds per acquisition, and a total of 1-15 spectra were

accumulated and averaged, depending on the level of noise. Any spikes caused by cosmic rays were removed using the software's spike removal function. No further data processing was performed after collection. Spectra were plotted using the program Origin.

Supplemental Figures

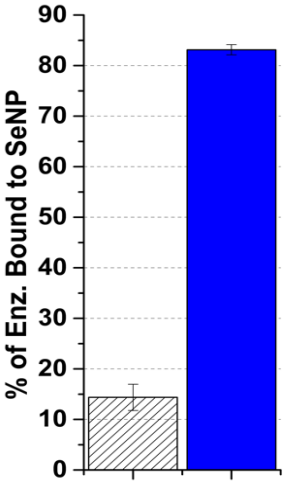

Figure A.1: Enzymatic retention of biogenic SeNPs. The grey bar represents the % of WT that remained bound to the enzyme, and the blue bar represents the % of cSeNP that remained bound to NPs.

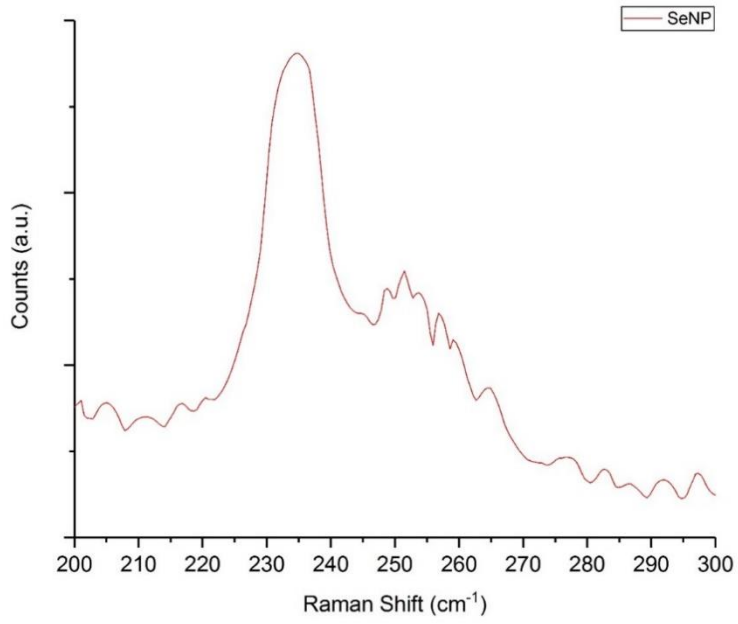

Figure A.2: Raman spectrum of inorganically synthesized SeNPs.

			Size (d.nm):	% Intensity:	St Dev (d.nm):
Z-Average (d.nm):	47.90	Peak 1:	48.86	100.0	7.100
PdI:	0.016	Peak 2:	0.000	0.0	0.000
Intercept:	0.954	Peak 3:	0.000	0.0	0.000
Result quality :	Good				

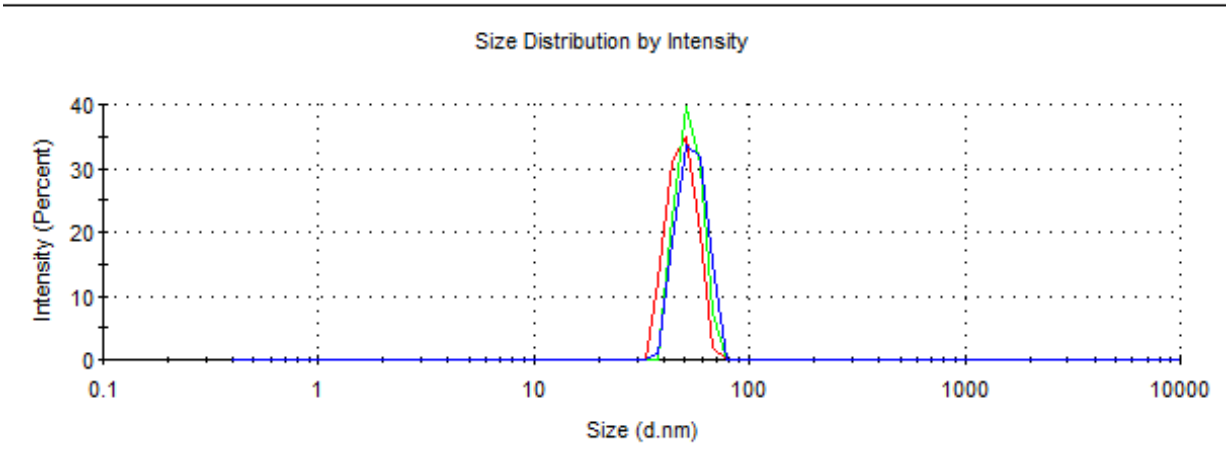

Figure A.3: DLS spectra of inorganically synthesized SeNPs before conjugation to SeBP.

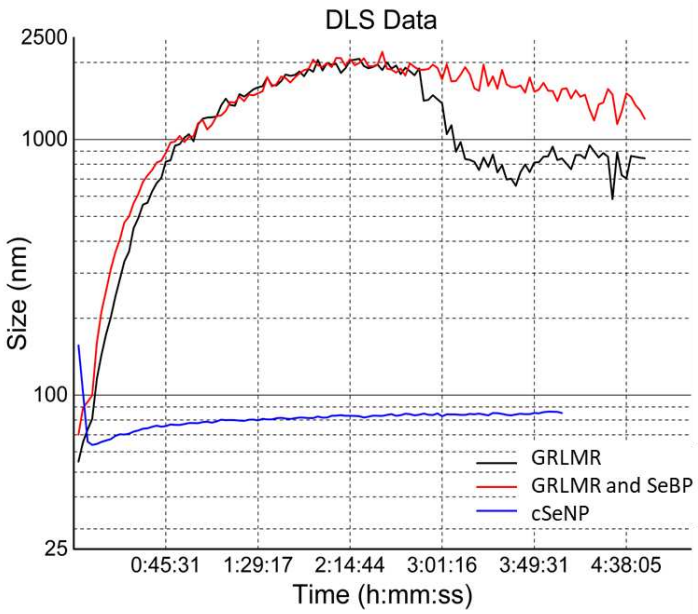

Figure A.4: DLS results of biogenic SeNP formation using GRLMR (black line), GRLMR with exogenous SeBP added to the mixture (red line), and cSeNP (blue line).

APPENDIX B: Supplemental to Chapter 3

Materials

T7 Expression *lysY/I^q* Competent *E. coli* cells (Cat no. C3013I) were purchased from New England Biolabs, Inc. Original plasmids containing GRLMR and F-cSeNPHis were designed and purchased from ATUM (DNA Twopointo, Inc.) in their pD441-CH expression vector. Luria Broth was purchased from Fisher Scientific. Kanamycin, Chloramphenicol, and IPTG were purchased from GoldBio. Sodium hydrogen selenite was purchased from Alfa Aesar. Molecular Biology grade ethanol and HPLC grade acetone were purchased from Fisher Scientific. Araldite 502 Kit; Araldite, EMbed 812 Kit; 25% aqueous EM grade glutaraldehyde, and 0.25% aqueous Toluidine Blue O Solution were purchased from Electron Microscopy Sciences.

Sterile snap cap culture tubes (max volume 12 mL) were used for initial growth and induction experiments. 15 mL falcon tubes were used during centrifugation and fixation. 1.5 mL microfuge tubes were used for fixation and encapsulation in agarose. 20 mL glass scintillation vials with screw tops were used during dehydration and embedment. BEEM® size 3 Embedding Capsules were used during high pressure freeze substitution protocols, and either BEEM® Flat Embedding Molds or Easy-Molds™ were used for standard fixation and embedment procedures.

The PELCO easiGlow™ Glow Discharge system was used to prepare EM grids. Either 200 mesh C-coated (5-6 nm thick) Cu grids or Cu slot grids coated in house-prepared Formvar were used for sample mounting.

Methods

Bacterial glycerol stocks containing the cSeNP-FtsZ chimera

BL21 (DE3) competent *E. coli* were transformed via heat shock with a high-copy pD441-CH expression vector containing the cSeNP-FtsZ gene. Transformed cells were grown overnight

at 37 °C on solid Miller's Luria Broth (LB) medium containing kanamycin and chloramphenicol antibiotics. The next day single colonies were picked and grown overnight in liquid LB with antibiotics at 225 rpm at 37 °C. The next day, stocks were made by adding sterile glycerol at a final concentration of 25% to 500 µL confluent culture and frozen in liquid nitrogen. Stocks were stored in the -80 °C freezer until needed.

Whole cell in vivo SeNP formation expressing the cSeNP-FtsZ chimera

The cells containing the chimeric DNA were grown in a shaker at 225 – 250 rpm for 16 – 24 hours at 37 °C in 2 mL Miller's Luria Broth (LB) containing kanamycin and chloramphenicol antibiotics. After cells reach confluency, the culture was diluted 1/100th by volume into 5 mL fresh antibiotic containing LB and allowed to grow at room temperature for an additional 3 – 6 hours to reach log phase. After an apparent optical density of 0.2 – 0.4 was reached, cells were treated with a final concentration of 1 – 2 mM SeO_3^{2-} (or 1 µM for SeO_3^{2-} the controls) and 0.1 – 1 mM isopropyl-β-D-thiogalactopyranoside (IPTG) to promote nanoparticle formation and expression of the cSeNP-FtsZ construct. *NOTE: In the text, we denote our Goldilocks conditions as 1 – 2 mM SeO_3^{2-} and 100 µM IPTG induced for 30 – 180 minutes. Our Red Sonja experiments refers to samples induced with 1 mM IPTG and 1 – 2 mM SeO_3^{2-} for 3 – 6 hours.*

After an induction period, which varied from 30 – 500 minutes, cells were centrifuged at 3000 xg at 4 °C for 3 minutes and washed with ice cold filter sterilized 0.1 M phosphate buffer (PB) pH 6.9 – 7.0 three to five times, or until cells were no longer "sticky." Cells were then fixed in buffered 1.5 – 2.5% glutaraldehyde (25% Electron Microscopy Sciences) for 1 hour at 4 °C. A final wash 3 – 5x in ice cold buffer at 3000 xg at 4 °C for 3 minutes was done before reconstituting the sample into 100 – 200 µL buffer to either plate cells or prepare them for dehydration. To plate,

5 µL of cells were drop-cast onto negatively glow-discharged C-coated 200 mesh Cu grids for 1 – 2 minutes followed by 2 washes with 5 µL filtered UpH_2O for 1 minute each.

Dehydration Protocol

To prepare samples for dehydration, cells were first encapsulated in molten 2.5% low melting temperature Agarose that had been diluted into either buffer or ultrapure water. To encapsulate the samples, molten agarose was added to the fixed sample prewarmed to 42 °C in a 1:1 ratio and quickly spun down at 4000 rpm for 3 minutes in a microfuge. After the spin down samples were immediately placed on ice to harden. Once firm enough to handle, <1 mm^3 cubes were diced and placed in the dehydration solvent. Serial dehydration occurred initially in acetone, but later was moved to ethanol according to the following series with at least two solvent changes during each step: 5 minutes in 30%, 5 minutes in 50%, 10 minutes in 70%, 10 minutes in 80%, 10 minutes in 90%, 10 minutes in 100%, 10 minutes in 100%.

Embedment procedure

Immediately following dehydration, the infiltration process can begin. Using acetone as the dehydration solvent, the sample is immediately placed in a 1:1 solution of acetone to complete resin for 30 – 60 minutes, then in complete resin for 2 hours with one change. Following this the sample was centered with a wooden applicator stick to an Easy-Mold™ capsule filled with 2 drops complete resin. Once centered, the capsule was filled entirely with resin and set into a prewarmed oven to cure for 16 hours at 60 °C.

Using ethanol as the dehydration solvent, the following approach was first used. The sample was placed in 100% propylene oxide transition fluid for 30 minutes with one change. Sample was transferred to a 1:1 solution of propylene oxide to complete resin for 30 – 60 minutes followed by transfer to 100% complete resin for 2 hours with one change. Following this the

sample was centered with a wooden applicator stick to an Easy-Mold™ capsule filled with 2 drops complete resin. Once centered, the capsule was filled entirely with resin and set into a prewarmed oven to cure for 16 hours at 60 °C.

Omitting propylene oxide, this modified procedure was used. Following dehydration, the sample was transferred to a 1:1 mixture of ethanol to uncatalyzed resin for 16 – 18 hours. Next the sample was transferred to 100% uncatalyzed resin for an additional 4 – 8 hours with one change. Following, the sample was transferred to complete (catalyzed) resin for 2 hours with one change. Finally, the sample was centered with a wooden applicator stick to an Easy-Mold™ capsule filled with 2 drops complete resin. Once centered, the capsule was filled entirely with resin and set into a prewarmed oven to either cure for 16 hours at 60 °C or for 3 – 5 days at 42 – 45 °C as a low temperature alternative.

High Pressure Freeze Substitution Method

After completing the induction time, live cells can be immediately spun down and plated into brass PELCO® freezer hats. Subsequently, cells were vitrified in a Wohlwend Compact 02 High Pressure Freezer and immediately transferred to a liquid nitrogen (LN_2) cooled freeze substitution cocktail composed of anhydrous 0.25% glutaraldehyde in ethanol with no cryoprotectant added placed in metal blocks. Samples were slowly brought up to -20 °C over the course of 4 – 5 days by surrounding the samples with dry ice in a Styrofoam box in a -20 °C freezer. The sample was removed from the freezer and placed in a refrigerator for 4 hours at 4 °C followed by 1 hour at room temperature. The samples were carefully washed 3x with molecular biology grade ethanol and removed from their freezer hats. Embedment was done using the protocols described above to collect plastic blocks.

EM Grid Preparation

200 mesh C-coated Cu grids were prepared for sample mounting by glow discharging in air for 45 seconds using the PELCO easiGlow™ apparatus.

Ultramicrotomy

The blocks were removed from the oven and roughly trimmed under a dissection scope using injector blades followed by fine trimming using a glass knife made with a LKB Type 7801B KnifeMaker. A Reichert-Jung Ultracut E Microtome was used with either a DiATOME Ultra 35° Diamond Knife or a glass knife to make thin (50 – 100 nm) sections for EM analysis. In some instances, semi-thin (100 – 200 nm) sections were made for better elemental mapping.

Scanning Electron Microscopy (SEM) Imaging

A JEOL JSM-6500 Field Emission Scanning Electron Microscope with an In-Lens thermal field emission electro gun (TFEG) was used for SEM imaging. It is also equipped with an Oxford Instruments energy dispersive X-ray spectrometer (EDS) and uses Oxford Aztec software for qualitative and quantitative elemental analysis.

Transmission Electron Microscopy (TEM) Imaging and Energy Dispersive X-ray Spectroscopy Characterization

A JEOL JEM-2100F Transmission Electron Microscope equipped with a Gatan Ultrascan 2K x 2K CCD camera to capture images in TEM mode and diffraction patterns was used. For STEM mode, a JEOL annular dark field (ADF) detector was used. For elemental analysis, an Oxford Instruments SSD EDS detector with Aztec software was used.

Figures

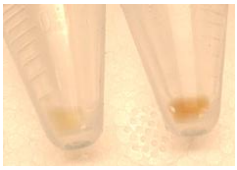

Figure B.1: (Left) control without adding SeO_3^{2-} (right) adding 2 mM SeO_3^{2-} for 2h and 250 uM IPTG.

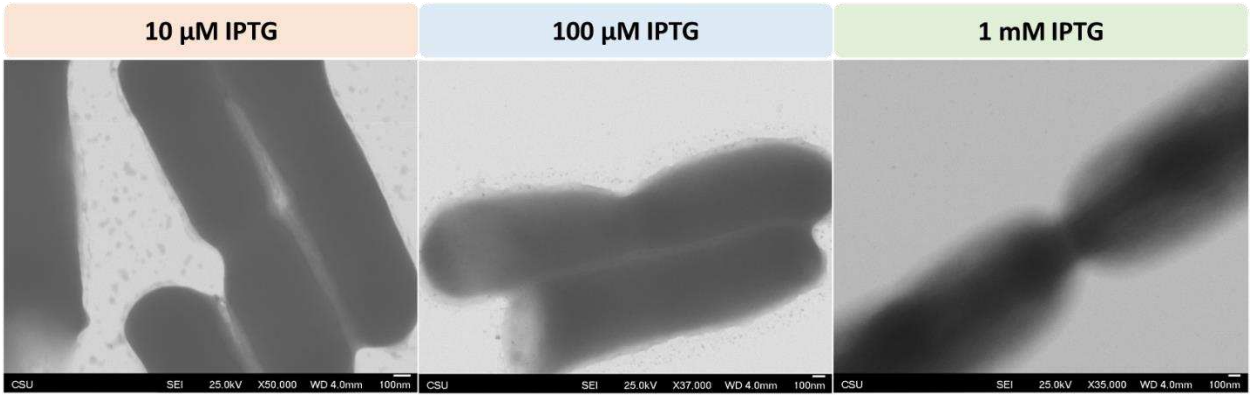

Figure B.2: IPTG induction screen results, incubating samples with 1 mM SeO_3^{2-} for the 10 µM sample to ensure cell viability and 2 mM SeO_3^{2-} for the 100 µM and 1 mM samples.

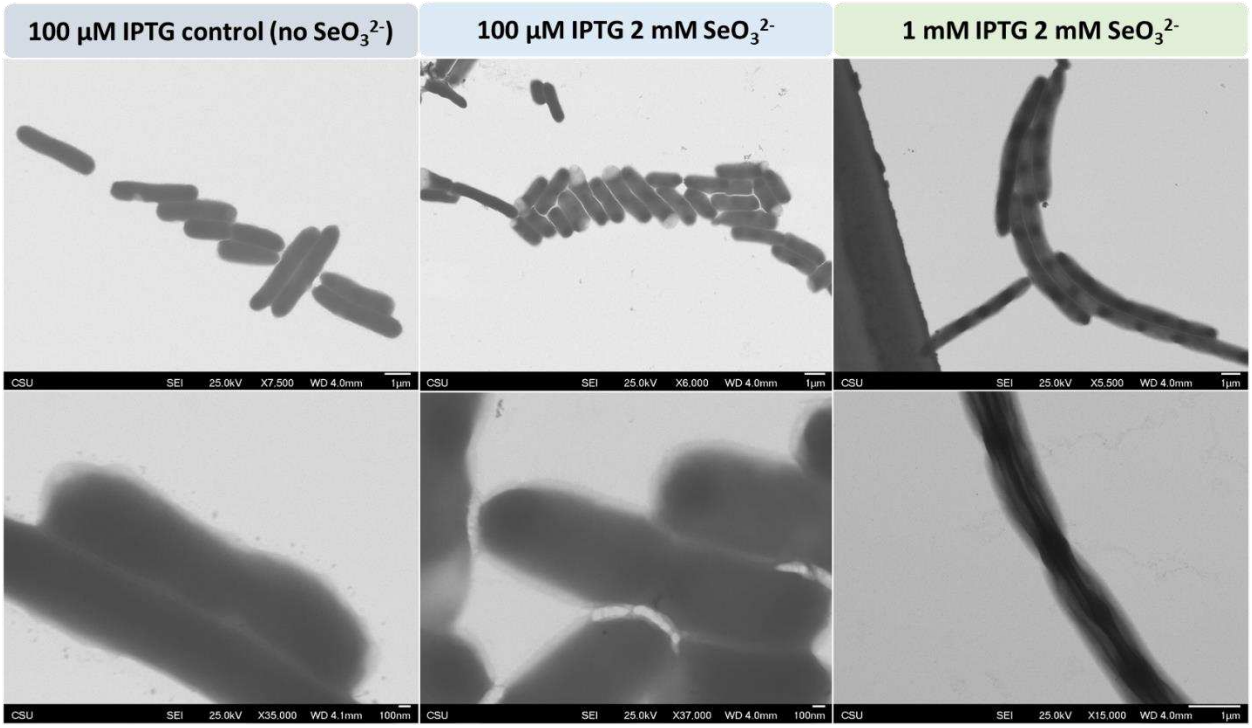

Figure B.3: IPTG induction experiment comparison between 100 µM and 1 mM screens. A control was included to confirm the lack of contrast in cells when no Se is added to the medium.

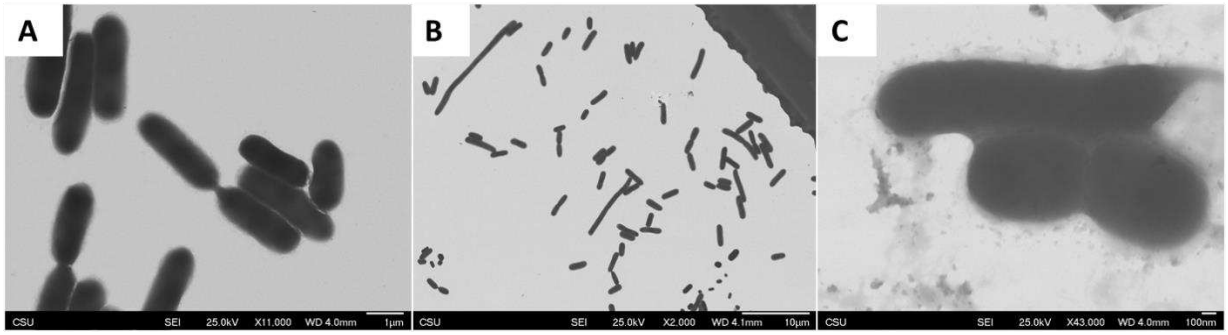

Figure B.4: SeO_3^{2-} concentration screen (A) 2.5 mM (B) 3 mM (C) 5 mM incubated for only 30 minutes. Cells begin to shrivel, indicating that conditions are too toxic and cells will not survive.

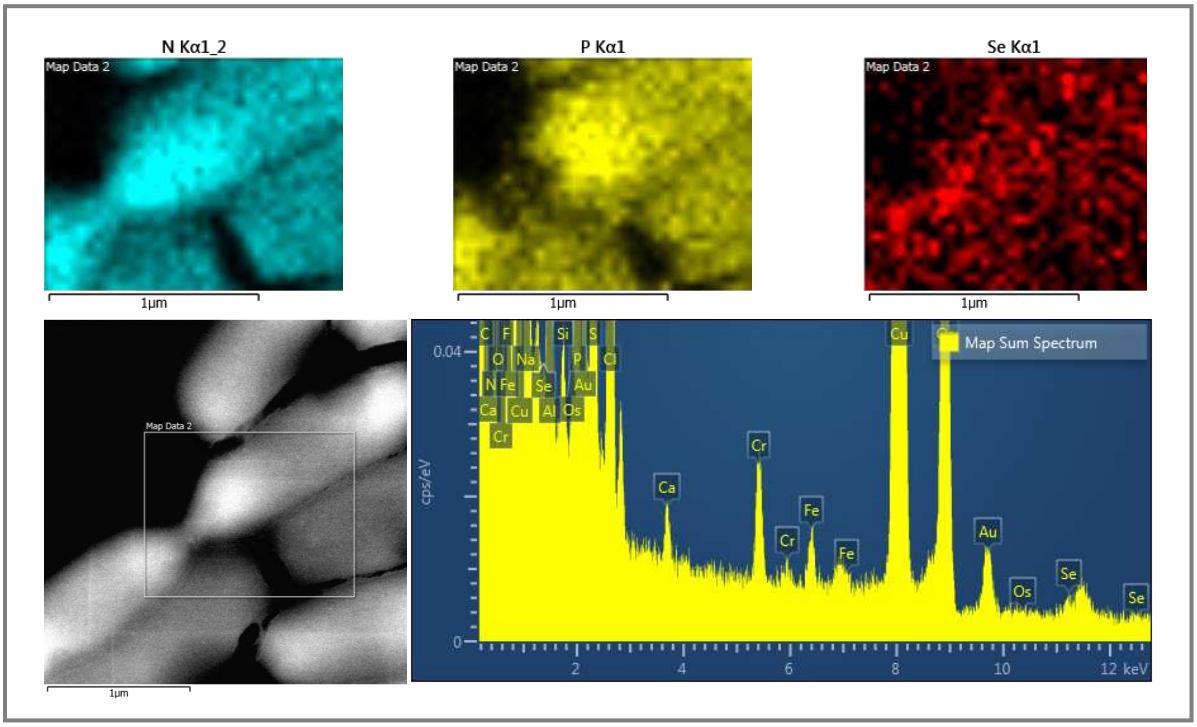

Figure B.5: EDS results of Figure 3.4.

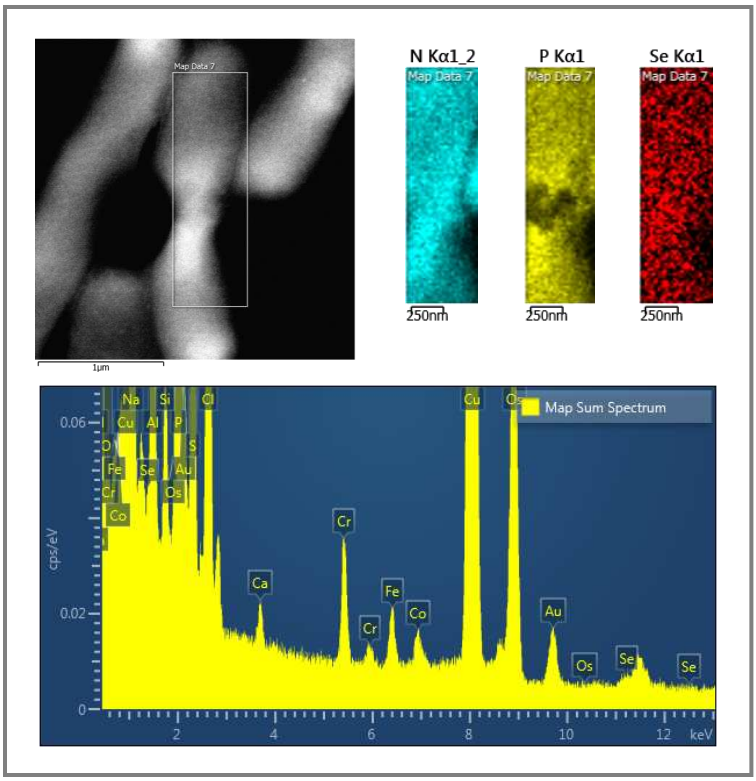

Figure B.6: EDS data of another cell from the same sample as in B.5.

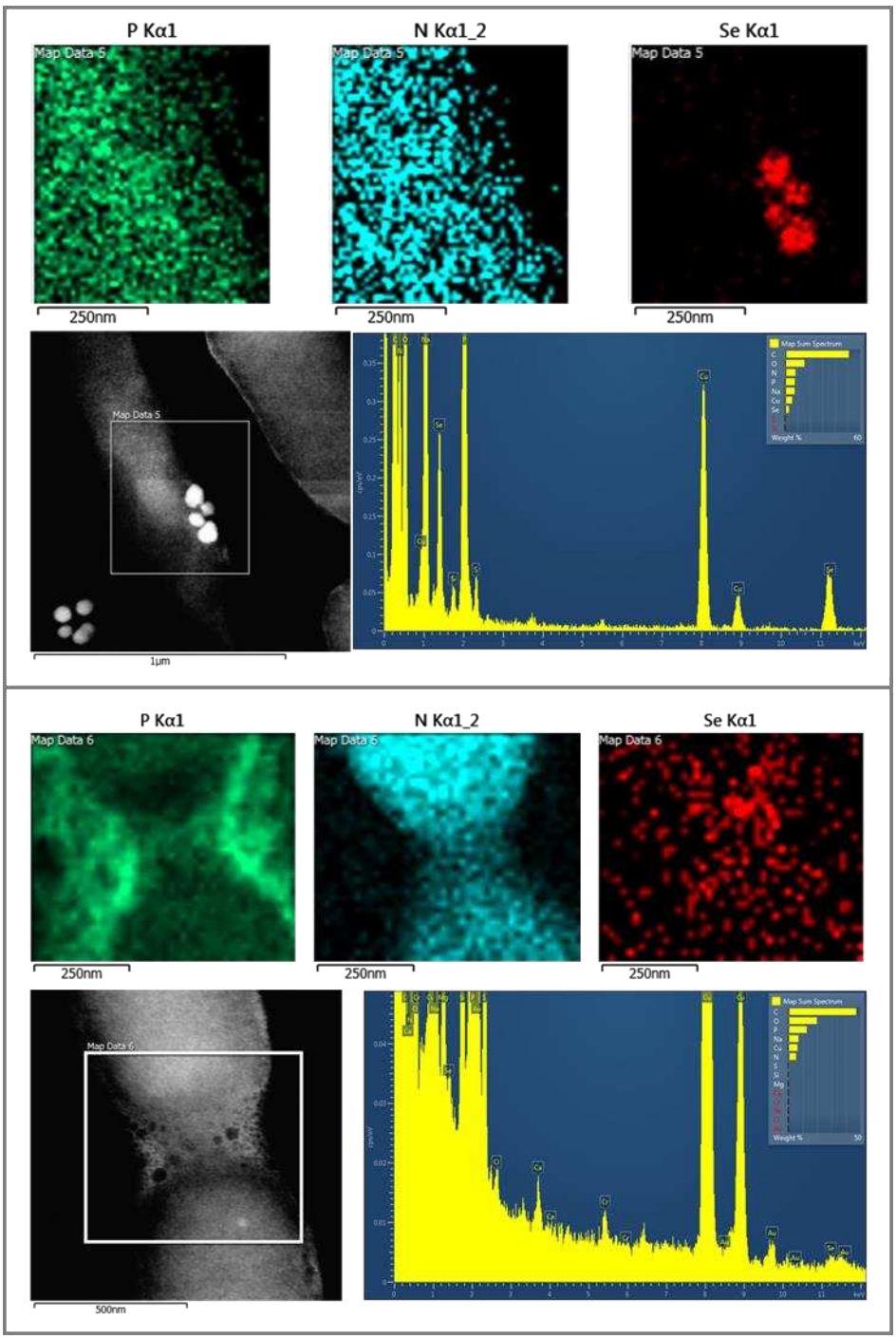

Figure B.7: EDS data of the N-term tag. Above are results from large particles found within the sample and below are results from a division point.

APPENDIX C: Supplemental to Chapter 4

Methods

We made a-SeNPs using a borohydride reduction method modeled from the Nath *et al.* (2004).[127] Briefly, we added 100 µL of a 10 mM $HNaSeO_3$ (aq) stock to 900 µL of 10 mM $NaBH_4$ (aq) on ice in 1.5 mL polystyrene microfuge tubes. After a color change from colorless to a red/orange was observed (within 5 minutes), 100 uL of an ice cold 1 M $Zn(OAc)_2$ (aq) stock was added to the mixture. The particles change color from red/orange to yellow/orange within 5 minutes. Since borohydride reduction reactions produce OH^- as a byproduct, it was important to maintain a pH below 12 since ZnO quantum dots can be produced by simply adding NaOH to Zn^{2+} precursors at a pH at or above 12.[144–146]

Various ratios of precursors were tried, including 1:1, 2:1, 3:1, 4:1, and 10:1 of $Zn(OAc)_2$ to $HNaSeO_3$; however, the 100:1 appeared to create the most fluorescent particles. Likewise, this same procedure was used to synthesize CdSe particles in a comparable time frame, replacing $Zn(OAc)_2$ with $Cd(OAc)_2$. Again, a 1:1, 4:1, and a 10:1 ratio of Cd:Se precursor were tried, yet the 100:1 produced the most fluorescent particles.

Other MSe particles were produced using a 100:1 ratio of M:Se precursors for Cu, Pb, and Co. With Sb and W, a 10:1 ratio was used. With Ce, a 1:1 ratio was used. With $KMnO_4$, a 4:1 ratio was used. In the case of Ag_2Se, these particles could be made using a 2:1 ratio of $AgNO_3$ to $HNaSeO_3$, but a 4:1 and a 10:1 ratio were also used. The 2:1 produced more of a red-brown solution, likely indicating smaller particle formation, whereas the 4:1 and 10:1 reactions both produced black particles. The reactions with the metals above occurred immediately after addition of the metal salt to the a-SeNP solution.

For syntheses performed *in situ*, 5 uL a-SeNPs were dropcast onto negatively glow discharged 200 mesh C-coated Cu EM grids and washed 2x with filtered UpH_2O. Following, 5 uL of the metal precursor was dropcast and aged on the grid for 5 minutes. The grid was blotted dry, washed 2x with filtered UpH_2O, and stored for LM/EM analysis.

Dynamic Light Scattering

A Malvern Zetasizer Nano ZS was used to collect DLS data. a-SeNP sizes were measured within 1 hour following synthesis. The dispersant medium was water with a Refractive Index (RI) of 1.33 and viscosity (cP) of 1.5678. Data was acquired at 4 °C, and the collection parameters were set to allow for automated detection based on the count rate with the appropriate attenuator aperture. The material RI for a-SeNPs was set to 2.60. ZnSe size data was collected identically to that of a-SeNPs, except the material RI for ZnSe was set to 2.40.

UV/Vis

A NanoDrop 2000 Spectrophotometer was used to collect absorbance data. A spectrum was collected every 5 seconds, and curves were created by taking the absorbance measured at 375 nm over time. For a-SeNPs, BH_4 was added to SeO_3 and a measurement was immediately taken as time = 0 seconds. For ZnSe and CdSe formation measurements, a-SeNPs were immediately transformed by adding $M(OAc)_2$ to the particles for time = 0 seconds. Occasionally, the cuvette was mixed, which accounts for outliers seen in the spectrum as the bubbles created affected the absorbance.

Transmission Electron Microscopy and Selected Area Electron Diffraction

A JEOL JEM-2100F Transmission Electron Microscope equipped with a Gatan Ultrascan 2K x 2K CCD camera to capture images in TEM mode and diffraction patterns was used. For

STEM mode, a JEOL annular dark field (ADF) detector was used. For SAED, 30 cm camera length was used in SA DIFF mode.

Fluorescence Microscopy

Fluorescence images were collected on an Olympus IX73 inverted microscope using 355 nm laser excitation and 3 mW power. The excitation was done in the epi direction, a 405 nm long pass filter was used to remove the excitation light from the collected signal. Images were collected on an Andor iXon 897 EMCCD camera.

Supplemental Figures and Tables

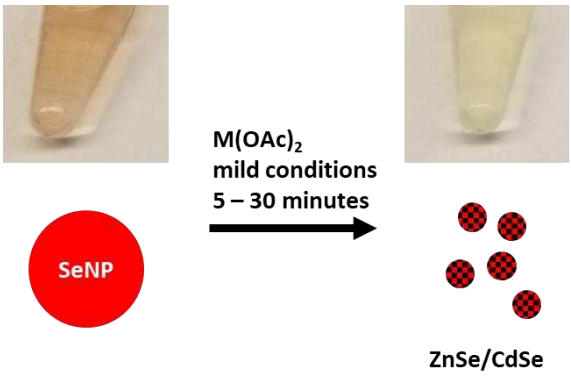

Figure C.1: Above are pictures of a solution of SeNPs before (left) and after reacting with $Zn(OAc)_2$ to form ZnSe particles. The color of CdSe particles is quite similar to ZnSe, but they are just a bit more orange.

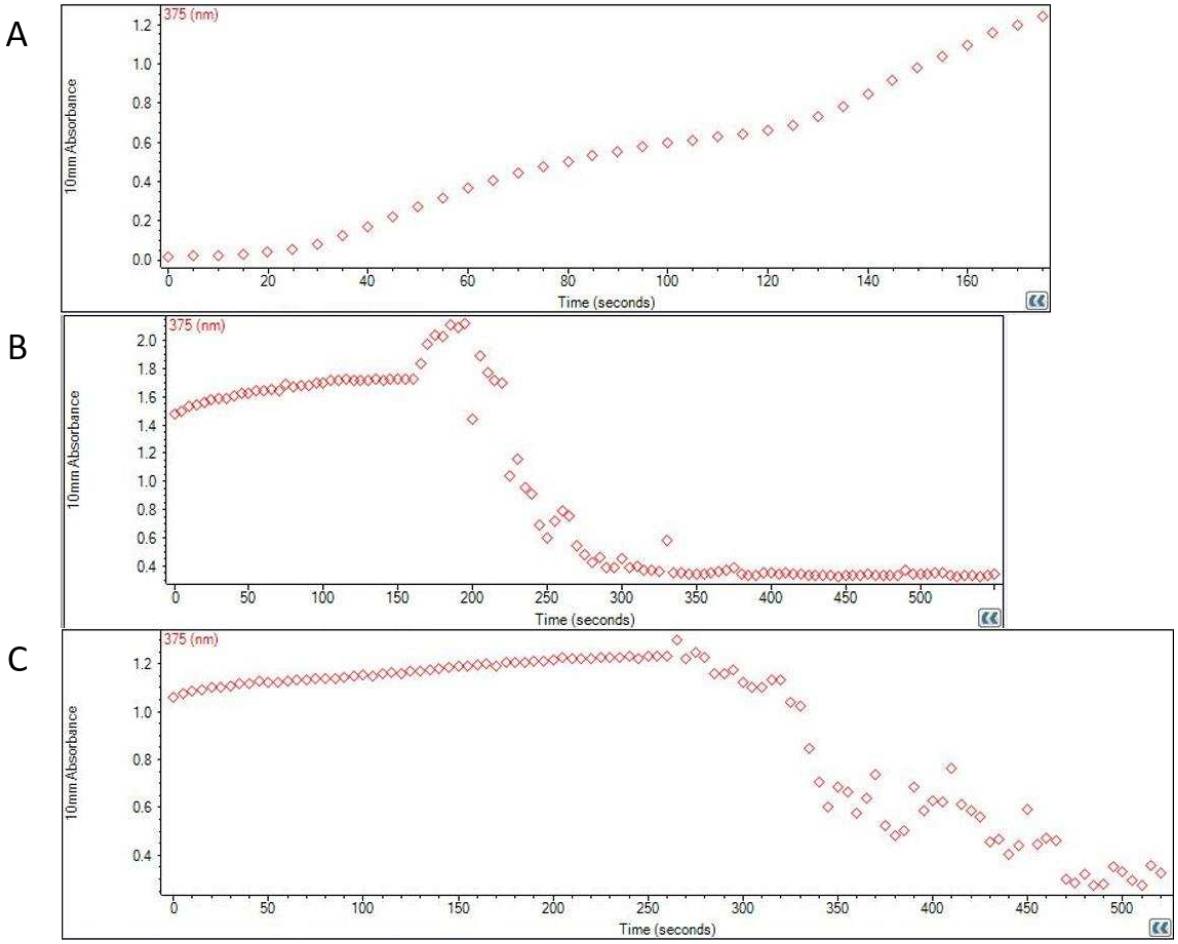

Figure C.2: UV/Vis spectroscopy monitoring the growth and decay of SeNP absorbance at 375 nm. (A) SeNP growth is monitored, and particles begin to form after approximately 30 seconds (s). After about 170 seconds, particle growth slows. (B) SeNP decay is monitored as a function of ZnSe formation. At time = 0 s, 100 µL of 1 M $Zn(OAc)_2$ is added to the cuvette. We see that the reaction completes within 300 seconds. (C) SeNP decay is monitored as a function of CdSe formation. At time = 0 s, 100 µL of 1 M $Cd(OAc)_2$ is added to the cuvette. We see that the reaction completes within 500 seconds.

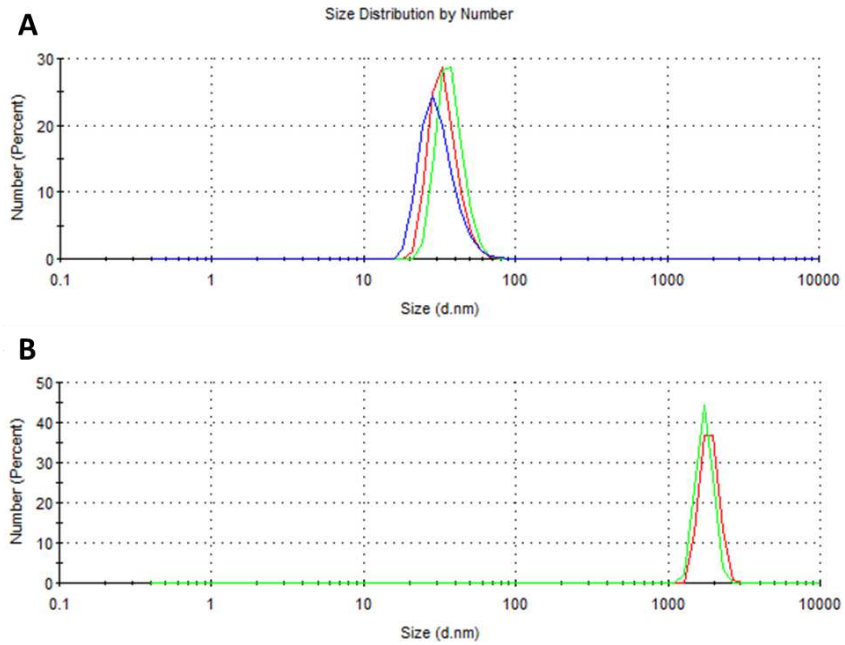

Figure C.3: (A) SeNPs as synthesized (B) ZnSe particles formed by adding $Zn(OAc)_2$ directly to a-SeNPs shown in A.

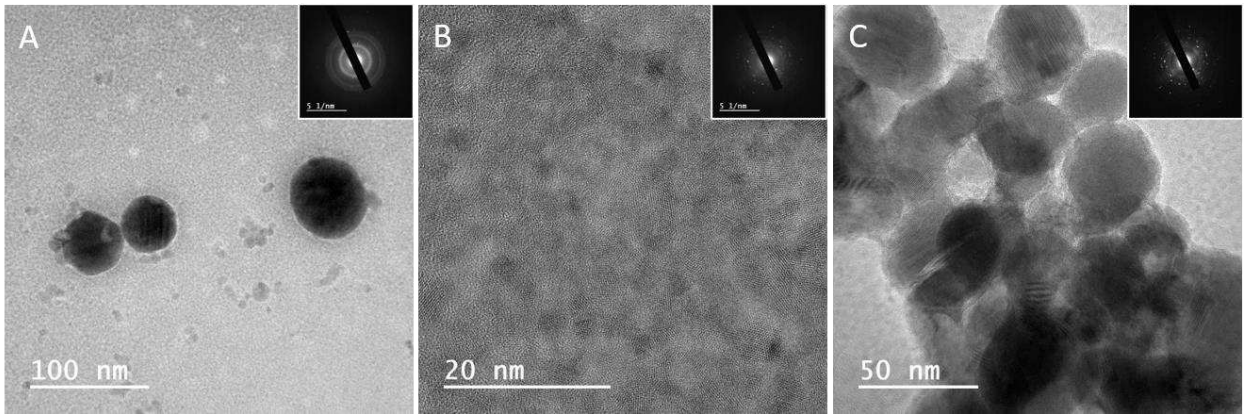

Figure C.4: ZnSe particles with the DP in the inset.

Table C.1: Indexing data from Figure C4 above.

Figure C.4A			Figure C.4B			Figure C.4C		
nm^{-1}	**d(Å)**	**hlk**	**nm^{-1}**	**d(Å)**	**hkl**	**nm^{-1}**	**d(Å)**	**hlk**
3	3.33	111	2.87	3.48	111	3	3.33	111
-	-	-	4.36	2.29	-	-	-	-
4.83	2.07	220	4.92	2.03	220	4.94	2.02	220
5.81	1.72	311	5.72	1.75	311	5.75	1.74	311
-	-	-	6.44	1.55	400	7.92	1.26	331
7.5	1.33	331	7.34	1.36	331	8.42	1.19	422
-	-	-	9.33	1.07	511	9	1.11	511
-	-	-	9.91	1.01	440	-	-	-
-	-	-	-	-	-	10.24	0.977	531

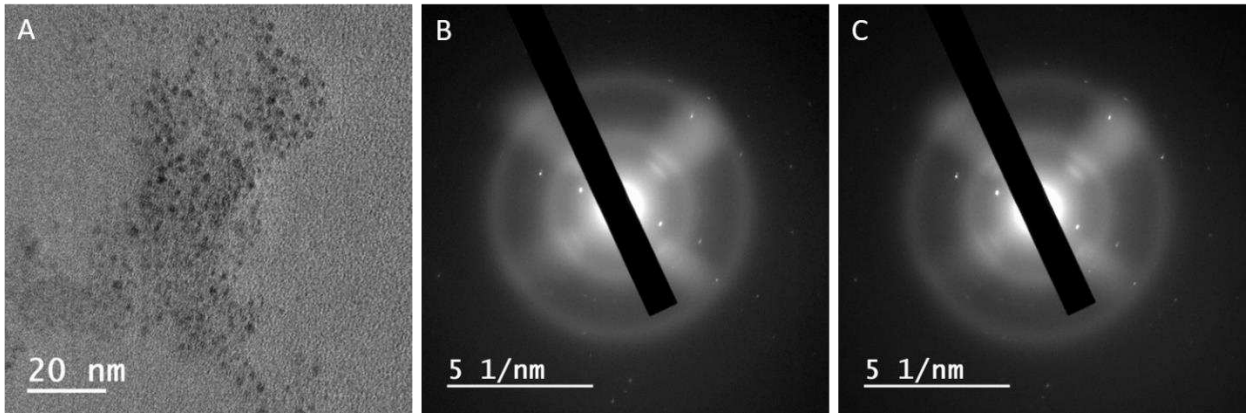

Figure C.5: CdSe SAED workup. (A) shows an example TEM image of CdSe particles formed. (B) and (C) are two diffraction images taken from different areas of the sample.

Table C.2: Indexing results from CdSe SAED images shown in Figure C5.

Figure C.5B			Figure C.5C		
nm^{-1}	**d(Å)**	**hlk**	**nm^{-1}**	**d(Å)**	**hkl**
2.93	0.341297	002	2.95	0.338983	002
2.98	0.33557	101	-	-	-
5.9	0.169492	202	5.95	0.168067	202
-	-	-	7.78	0.128535	300
8.24	0.121359	213	-	-	-
8.9	0.11236	205	8.87	0.11274	205
9.11	0.109769	-	-	-	-

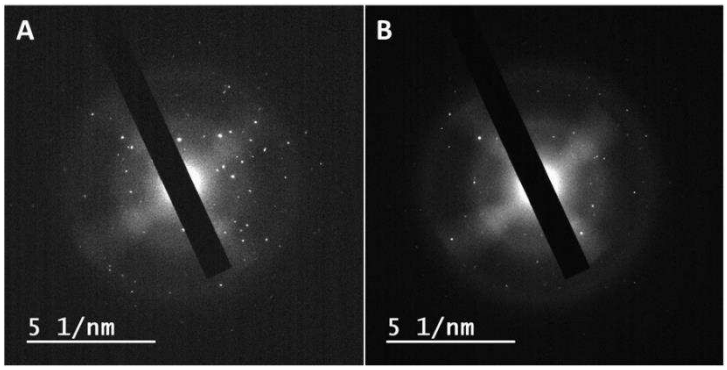

Figure C.6: SAED patterns from Cu_xSe_y sample.

Table C.3: Indexing results of Cu_xSe_y SAED images above in Figure C6.

DP from Figure C.6A				DP from Figure C.6B			
nm^{-1}	**d(Å)**	**hkl Cu_3Se_2**	**hkl CuSe**	**nm^{-1}**	**d(Å)**	**hkl Cu_3Se_2**	**hkl CuSe**
3.92	2.551	[201]		2.92	3.425	[101]	[021]
3.93	2.5445	[201]		3.48	2.874	[210]	[006]
4.02	2.4876	[201]		4	2.5	[201]	[025]
4.05	2.4691	[201]		4.01	2.494	[201?]	[025]
4.47	2.2371	[220]		4.09	2.445	[211]	[025]
4.49	2.2272	[220]		4.47	2.237	[220]	
4.52	2.2124	[220]		4.73	2.114	[002]	
4.82	2.0747	[310]	[117][130]	4.74	2.11	[002]	[117]/[130]
4.84	2.0661	[310]	[117][130]	5.04	1.984	[221]	[200]
4.88	2.0492	[310]	[117][130]	5.52	1.812	[311]	[118]
4.96	2.0161	[221]	[117][130]	5.85	1.709	[212?]	[222]
5.08	1.9685	[221]	[200]				
5.82	1.7182		[041]/[135]				
5.83	1.7153		[222]				
5.84	1.7123		[222]				
7.51	1.3316		[228]				
7.75	1.2903		[152]/[20(10)] /[242][311]				
7.76	1.2887		[152]/[20(10)] /[242][311]				
8.23	1.2151	[511]					
8.75	1.1429		[317]/[330]				

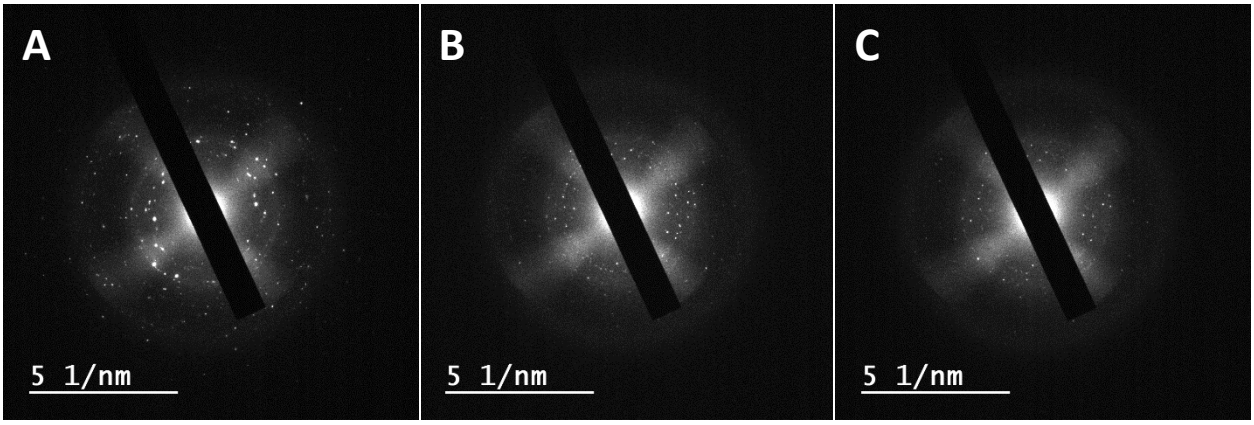

Figure C.7: Ag_2Se SAED patterns

Table C.4: Indexing results from Ag_2Se DPs above in Figure C7.

DP Figure C.7A			DP Figure C.7B			DP Figure C.7C		
nm^{-1}	**d(Å)**	**hkl**	**nm^{-1}**	**d(Å)**	**hkl**	**nm^{-1}**	**d(Å)**	**hkl**
3	3.33333	[111]	3.14	3.18471	[111]	3.46	2.89017	[102]
3.45	2.89855	[102]	3.77	2.65252	[112]	4.1	2.43902	[013]
3.8	2.63158	[112]	4.09	2.44499	[013]	4.47	2.23714	[122]
4.01	2.49377	[013]	4.48	2.23214	[122]	4.97	2.01207	[032]
4.71	2.12314	[113]	4.98	2.00803	[032]			
4.8	2.08333	[032]	5.03	1.98807				
4.9	2.04082	[211]	5.69	1.75747				
5.29	1.89036							
5.75	1.73913							
6.89	1.45138							
8.36	1.19617							

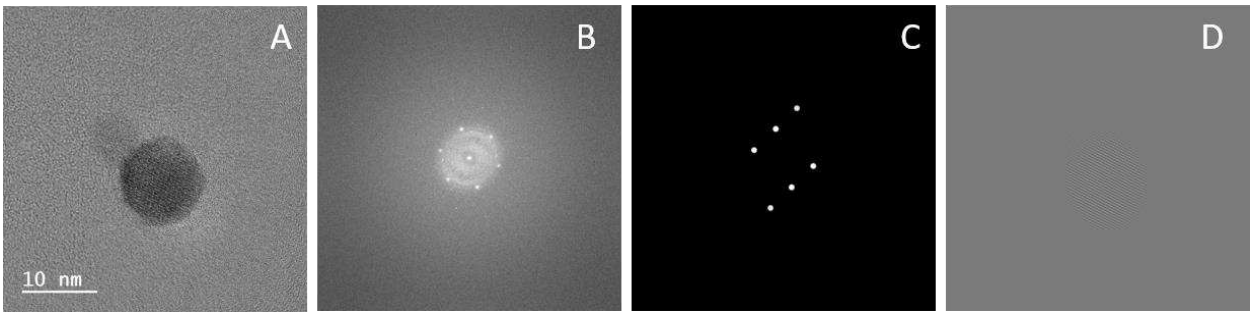

Figure C.8: Image workup from Figure 1C in the manuscript. Simple math was done on the raw image (A) to emphasize the lattice planes. (B) An FFT of the image was extracted, and (C) a mask was applied to the FFT and smoothed by 3 pixels. (D) An inverse FFT was taken of the masked area. The inverse FFT was added to the raw image to get the image shown in Figure 1C.

APPENDIX D: Supplemental to Chapter 5

Methods

In vivo *formation of SeNPs*

Samples were first prepared as described in Appendix B. Briefly, after cells containing the cSeNP-FtsZ construct reached log phase, an IPTG induction was performed using a final concentration of 0.1 – 1.0 mM IPTG and 1 – 2 mM SeO_3^{2-}. Samples were incubated for 30 minutes – 3 hours to allow SeNPs to form. Controls were made using either 1 μM SeO_3^{2-} or no SeO_3^{2-}, and it is made explicit in the text which controls were made.

Another batch of samples were made following the same procedure described, but instead of using the cSeNP-FtsZ construct, only the *E. coli* containing the cSeNP concatemer DNA was used. This was used for an initial check with the ZnSe particle samples to ensure that SeNPs would be large enough to be noticeable within the sample and to view if a similar ZnSe morphology would be observed *in vivo*.

Formation of ZnSe and CdSe particles post-fixation

Following SeNP formation, the sample was washed 4x with ice cold filtered 0.1 M acetate pH 5.6 at 3000 xg at 4 °C for 3 minutes each. Next, the sample was fixed at 4 °C with 2.5% glutaraldehyde buffered in acetate for 1 hour. The sample was washed 4x with buffer and split evenly into two aliquots. To each aliquot, either $Zn(OAc)_2$ or $Cd(OAc)_2$ was added at a total concentration of 50 mM to the cells at 4 °C overnight. The next day, the samples were washed 4x and prepared for embedment as described in Appendix B.

Formation of Ag_2Se and CuSe particles post-fixation

Following SeNP formation, the sample was washed 4x in ice cold filtered 0.1 M phosphate buffer at pH 7 at 3000 xg at 4 °C for 3 minutes each. Samples were fixed using 1.5 – 2.5% buffered

glutaraldehyde for 1 hour. Samples were then washed 3x with ice cold filtered 0.1 M acetate pH 5.6 at 3000 xg at 4 °C for 3 minutes each. Samples were then incubated with either $AgNO_3$ or $Cu(OAc)_2$ at a final concentration of 1 mM for 1 hour at 4 °C. Samples were washed 3x in acetate buffer and prepared for embedment as described in Appendix B. These controls did not contain Se supplement.

In another preparation, we wanted to enzymatically produce as many particles as possible. A low level induction was done overnight using 10 µM IPTG and 1 µM SeO_3^{2-} to have a minimal amount of chimera present for the ramp up, which was done following a 5 hour dilution at 30 °C by inducing with 100 µM IPTG and 2 mM SeO_3^{2-} for 3 hours while cells were in log phase (O.D. ca. 0.4). For disproportionation reactions performed post-fixation, the sample was first fixed following protocols described in Appendix B. The sample was washed 3x with filtered 0.1 M acetate pH 5.6 and immediately soaked with either 1 mM $AgNO_3$ or $Cu(OAc)_2$ overnight at 4 °C. The control was treated identically except the [SeO_3^{2-}] was kept at 1 µM.

Formation of CuSe particles in vivo

Following SeNP formation, CuSe particles were made by adding $Cu(OAc)_2$ to the live culture at 1 mM, 500 µM, 250 µM, and 100 µM final concentrations for 1 hour. Following CuSe formation, indicated by the transformation of the culture from red to brown, samples were washed 3x with ice cold filtered 0.1 M acetate pH 5.6 at 3000 xg at 4 °C for 3 minutes each. Next, the sample was fixed at 4 °C with 2.5% glutaraldehyde buffered in acetate for 1 hour. Following, samples were washed 3x with buffer as described and prepared for embedment as described in Appendix B. Controls were supplemented with 1 µM SeO_3^{2-}.

Transmission Electron Microscopy Sample Preparation and Analysis

Sections were prepared for 2D TEM as described in Appendix B to generate 100 nm sections for analysis.

A JEOL JEM-2100F Transmission Electron Microscope equipped with a Gatan Ultrascan 2K x 2K CCD camera to capture images in TEM mode and diffraction patterns was used. For STEM mode, a JEOL annular dark field (ADF) detector was used. For elemental analysis, an Oxford Instruments SSD EDS detector with Aztec software was used.

Electron Tomography

All data collection and tomogram reconstruction was done by Eileen O'Toole and Garry Morgan at the University of Colorado in Boulder. Tomograms were reconstructed from a tilt series collected from a 200 – 300 nm thick section using SerialEM and ETomo software. No post-fixation stain was applied and no gold fiducials were added. This means that there is no question that the contrast we are observing is from the intracellular particles and not from salts or fiducials added *ex situ*.

The tilt series was collected using 2° steps over 120° at 31 kX, 39 kX, and 59 kX magnification on a FEI Tecnai F30 FEG-TEM equipped with a Gatan OneView IS (4k) CCD at 300 kV. Following acquisition, tilts were reconstructed by inputting the Setup parameters into Etomo. Of particular note is that Etomo was able to align tilts using intracellular particles as the fiducial markers for the seed model. Following tomogram generation, a nonlinear anisotropic diffusion filter was applied to improve contrast, which is not usual but was necessary for our samples since they were not stained with heavy metals.

Segmentation of reconstructions

IMOD was used to semi-automatically segment the tomographic reconstructions to reproduce models of the nanoparticles and cell membrane.

Figures

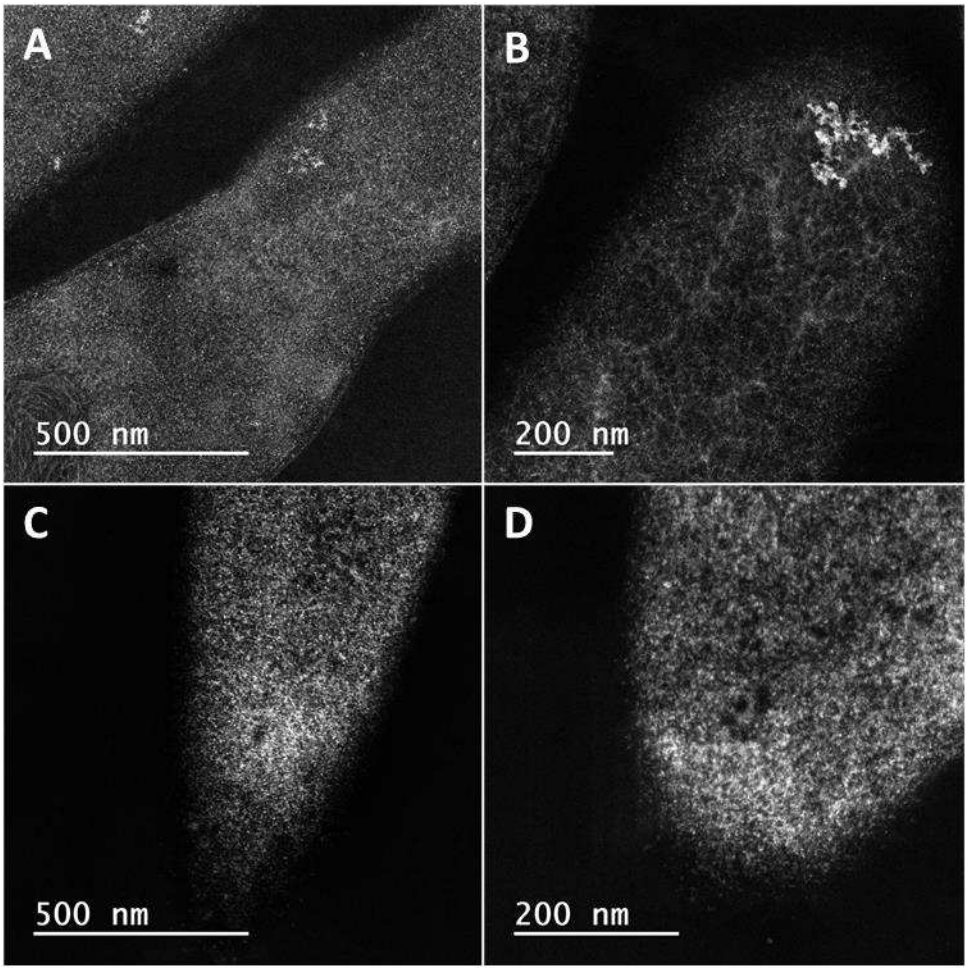

Figure D.1: 3h 1mM Se (1 µM control) 1mM IPTG for comparison during $KMnO_4$ trials. (A&B) control, (C&D) SeNP sample

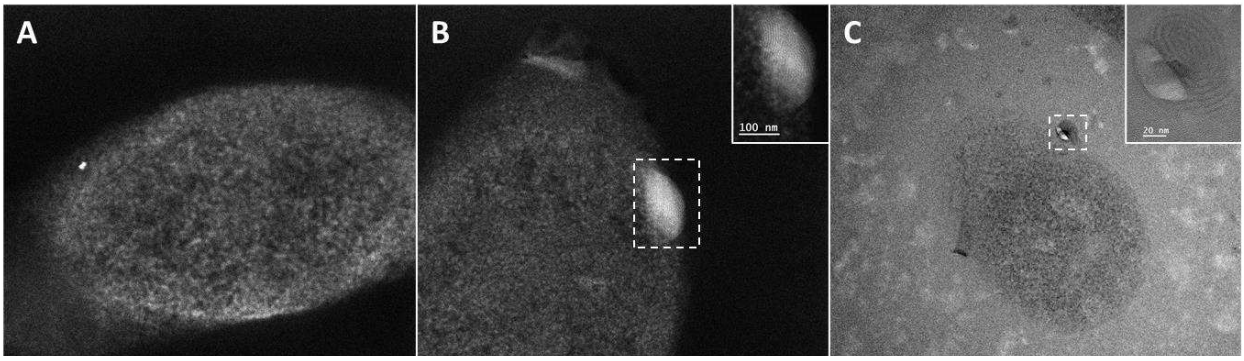

Figure D.2: Sample processed with Zn-Formalin fixation. (A) A representation of the cells within the sample. (B) Example of the wave-pattern boxed in white and blow up in the inset. (C) HR-TEM image of a cell with another wave-like pattern boxed in white and blown up in the inset.

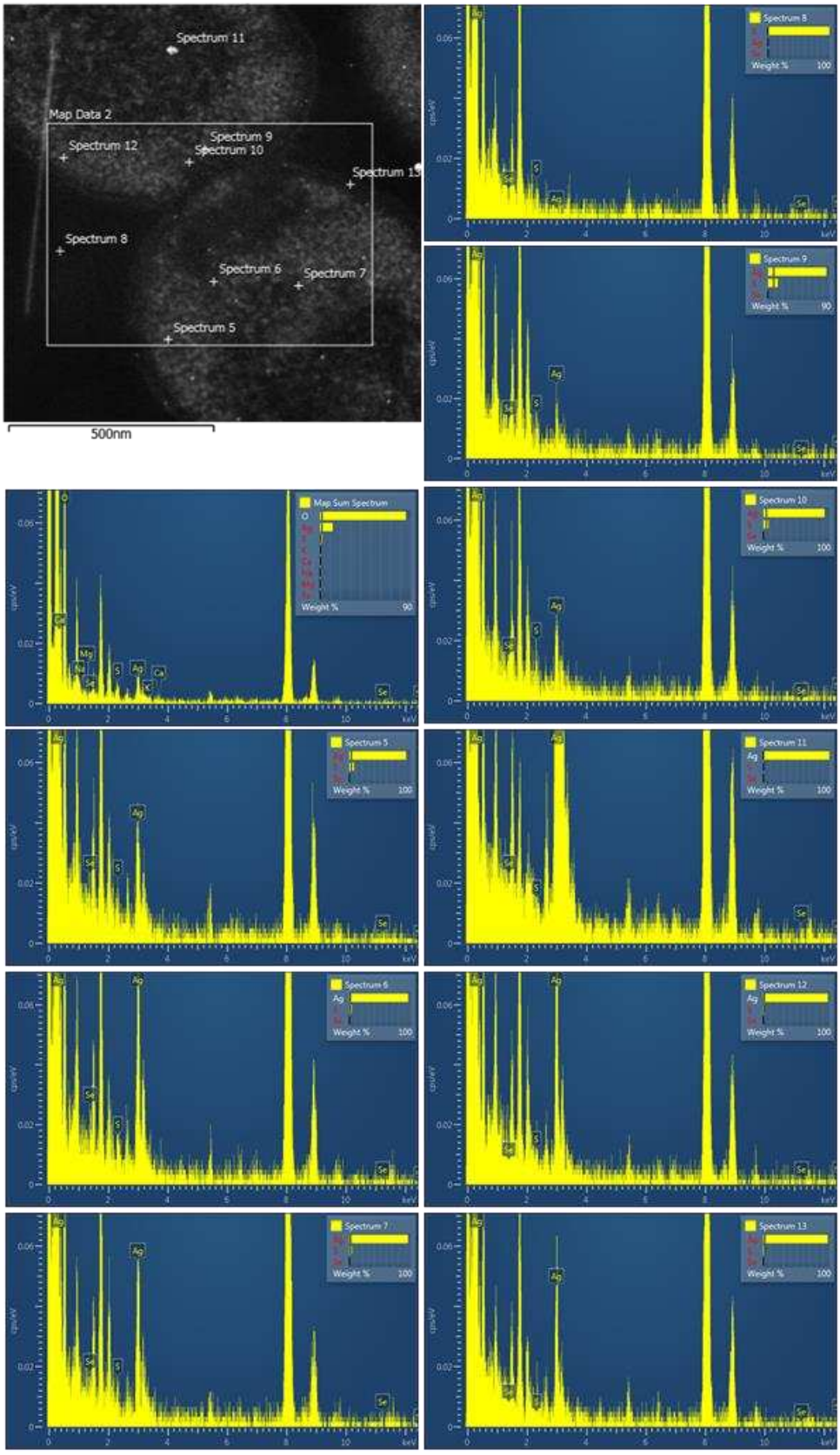

Figure D.3: EDS data of Ag_2Se sample from Figure 5.6C showing the map sum spectrum and point spectra of many particles in the cell.

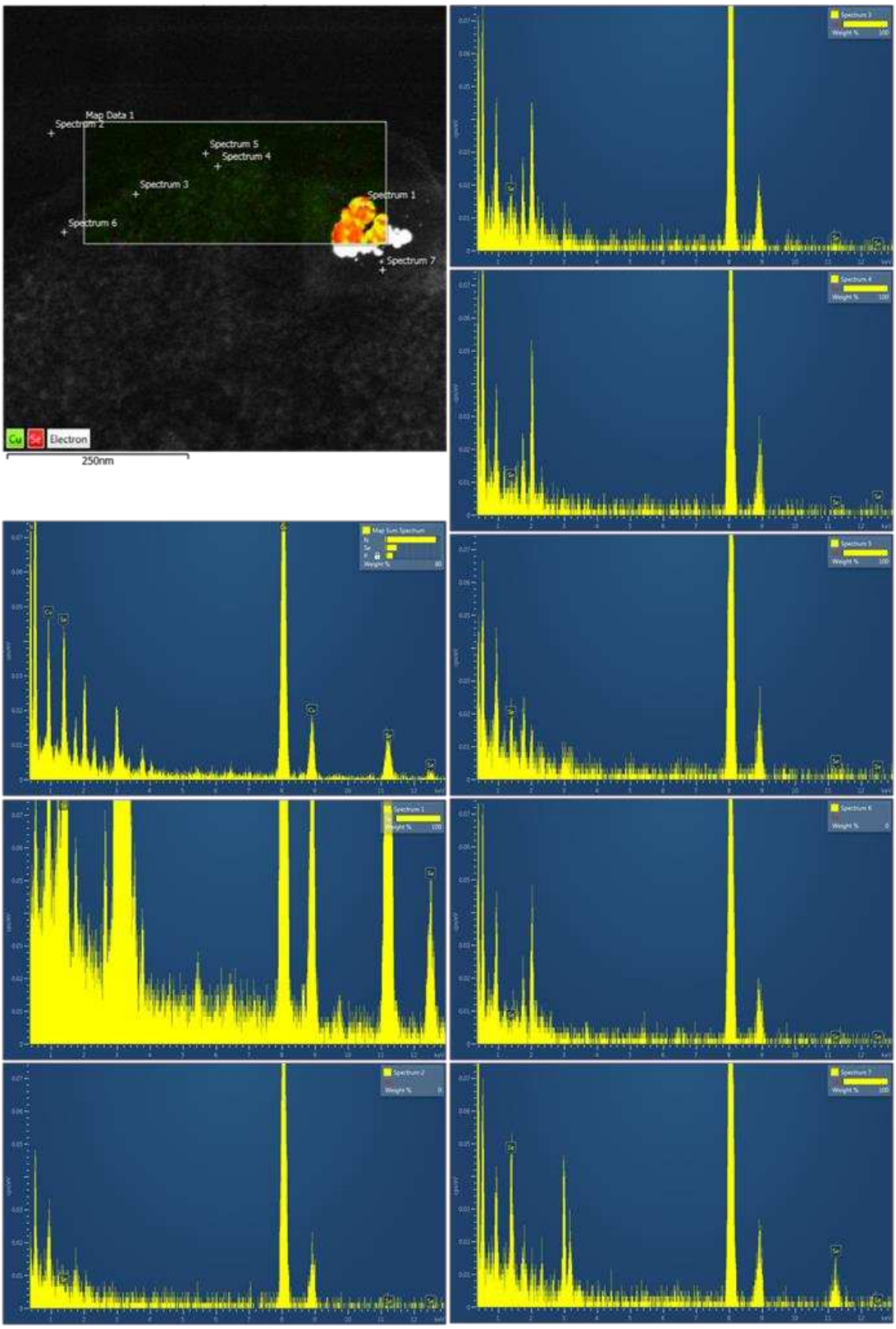

Figure D.4: EDS maps of the CuSe sample in Figure 5.8E & F, showing the map sum spectrum and the point spectra of multiple particles in the cell.

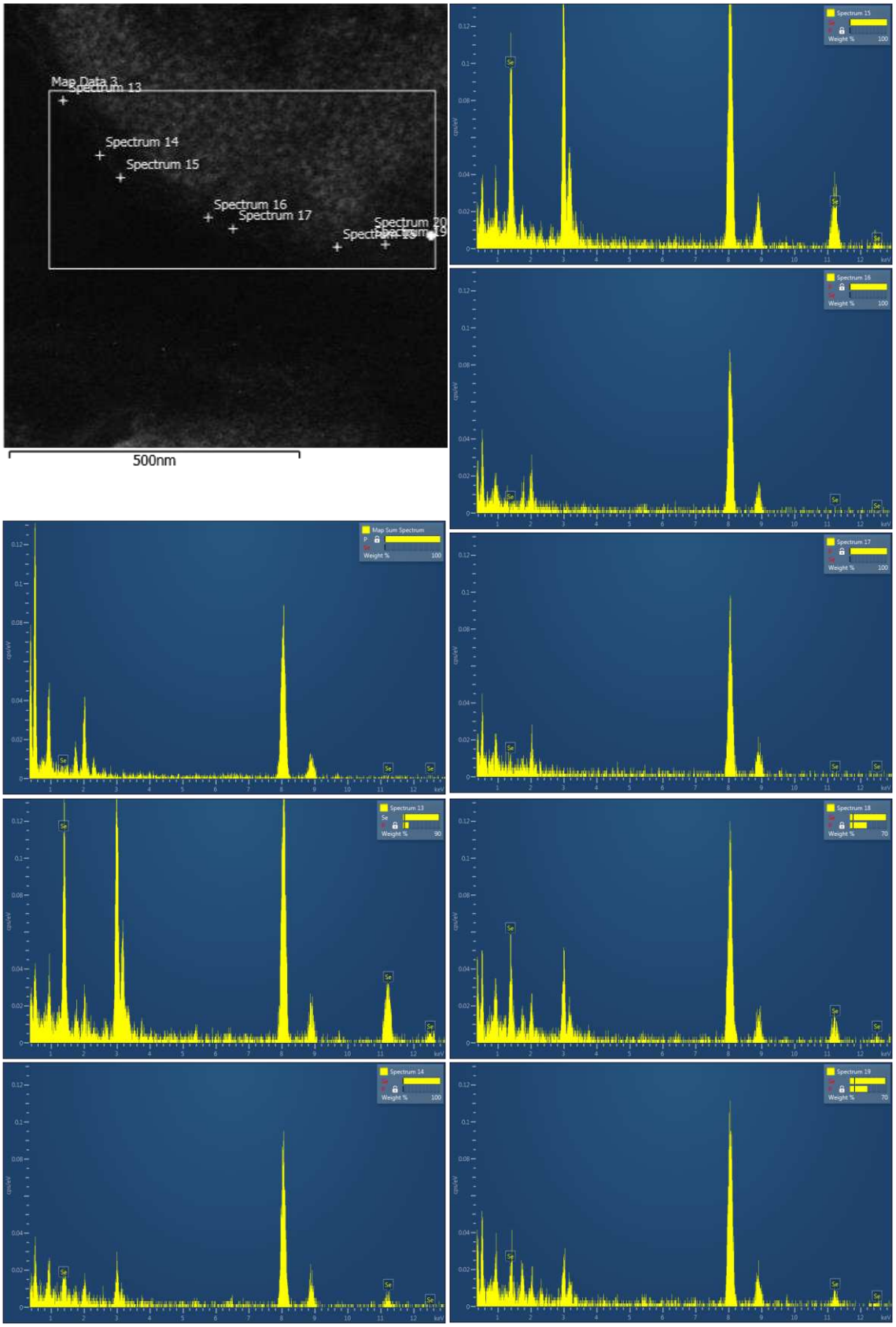

Figure D.5: CuSe EDS of Figure 5.8C showing the map sum spectrum and the point spectra of multiple particles in the cell.

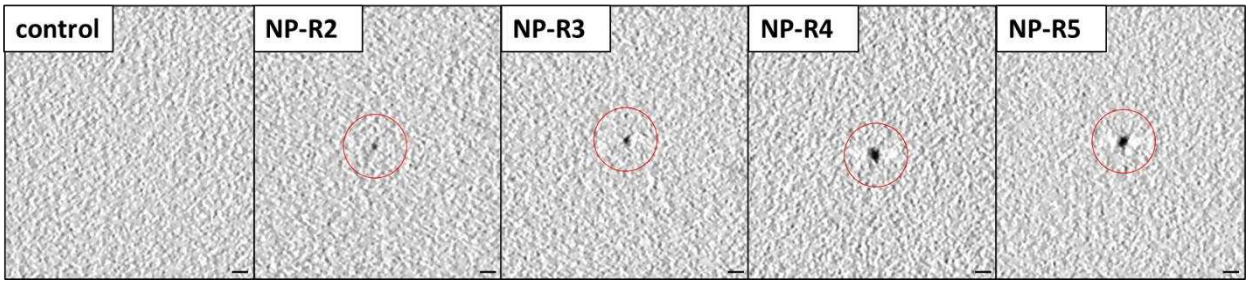

Figure D.6: Example of how particles were picked with respect to the background. The control panel contains no particles, NP-R2 represents the smallest particles selected, NP-R3 are slightly larger, and so on as shown. The particles are circled in red. Scale bars are all 5 nm.

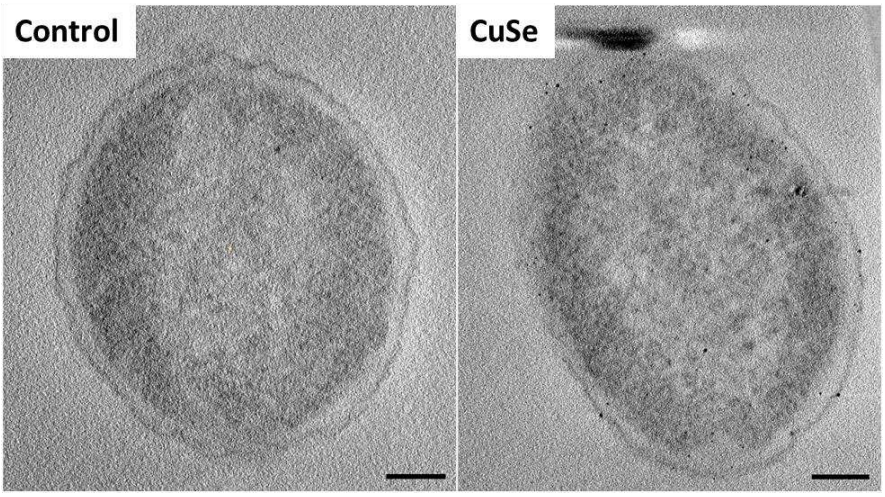

Figure D.7: 100 averaged slices of the control and the CuSe sample shown for comparison. Scale bars are 100 nm.